DEVELOPMENT OF A PULSE MODULATOR FOR ACTIVE FLOW CONTROL IN TURBOMACHINERY

A Thesis

by

SHALOM JOHNSON

Submitted to the Office of Graduate Studies of
Texas A&M University
in partial fulfillment of the requirements for the degree of

MASTER OF SCIENCE

May 2010

Major Subject: Aerospace Engineering

DEVELOPMENT OF A PULSE MODULATOR FOR ACTIVE FLOW CONTROL IN TURBOMACHINERY

A Thesis

by

SHALOM JOHNSON

Submitted to the Office of Graduate Studies of
Texas A&M University
in partial fulfillment of the requirements for the degree of

MASTER OF SCIENCE

Approved by:

Chair of Committee,	Othon Rediniotis
Committee Members,	Paul Cizmas
	Mark Holtzapple
Head of Department,	Dimitris Lagoudas

May 2010

Major Subject: Aerospace Engineering

ABSTRACT

Development of a Pulse Modulator for Active Flow Control in Turbomachinery.

(May 2010)

Shalom Johnson, B.S., Aerospace Engineering, Texas A&M University

Chair of Advisory Committee: Dr. Othon Rediniotis

In today's highly maneuverable jet aircraft designs, aircraft are required to have a propulsion system that can operate during sudden accelerations and rapid changes in angle-of-attack. Consequently, the compressor of the jet engine occasionally must operate at low-flow rates and rapid changes in inlet conditions. The high angle-of-attack and low-flow regime of compressor operation is often plagued by rotating stall and surge. Rotating stall and surge can result in loss of engine performance, rapid heating of the blades, and severe mechanical stresses. Traditional methods for suppressing rotating stall and surge only partially protect against rotating stall or reduce compressor efficiency. The objective of this research is to design a stall suppression system that will introduce oscillatory blowing into one of the rotor blade (stall suppression blade). This oscillatory blowing method has been tested on a wing section in a wind tunnel and has shown to increase the stall angle-of-attack by several degrees. This increase in stall angle-of-attack will eliminate stall cells as they form in the compressor. The goal of this research is to design a single stage axial compressor that will incorporate the new oscillatory blowing stall suppression system; moreover, this research will design, build, and test a scaled down version of this suppression system.

ACKNOWLEDGMENTS

I wish to express my gratitude to my advisor Dr. Othon Rediniotis for supporting me financially and academically. I'd like to thank him for the opportunity to work for him as an undergraduate. It truly had a great impact on my choice to pursue a graduate degree. Moreover, I would like to thank him for his trust and confidence in my work, which motivated me to be diligent and thorough in my research.

I would also like to thank Dr. Paul Cizmas for his patience, enthusiasm, and guidance.

I would also like to thank Dr. Mark Holtzapple for taking the time to serve on my graduate committee. Furthermore, I would like to thank the Aerospace Department staff, especially Ms. Colleen Leatherman and Ms. Karen Knabe.

I would like to thank my parents and my sister for their unconditional love and support. In particular I would like to thank my brothers for there support and guidance throughout every one of my endeavors. I would also like to recognize Forrest Carpenter whom I cannot thank enough for his generosity in helping me throughout my college career. I would also like to thank my research team, Yogesh Babbar and Andrew Wilson Beckett, for their advice, recommendations, and help in my research. Finally, I would like to thank my friends, Celine Kluzak, Luis Calixto, Baljeet Singh, Brian Owens, Kevin Maxwell, David Liliedahl, James Doebbler, Jeremy Davis, Richard Margulieux, Manoranjan Majji, Lance Hughes, Josh Weimar, and Raktim Bhattacharya for their support and words of wisdom.

This work was sponsored by the Air Force Office of Scientific Research un-

der grant/contract number FA9550-07-1-0187. The views and conclusions contained herein are those of the authors and should not be interpreted as necessarily representing the official policies or endorsements, either expressed or implied, of the Air Force Office of Scientific Research or the U.S. Government.

TABLE OF CONTENTS

Page

CHAPTER Page

CHAPTER Page

CHAPTER Page

LIST OF TABLES

TABLE Page

LIST OF FIGURES

FIGURE Page

FIGURE Page

FIGURE Page

FIGURE Page

FIGURE Page

FIGURE Page

FIGURE Page

NOMENCLATURE

S	Arc length [m]
R	Radios [m]
DC	Duty cycle
n_{slot}	Number of slots
f	Frequency [Hz]
C	Chord of the blade [m]
x_{te}	Distance to the air injection slot/holes from the trailing edge of the blade [m]
$\Re$	The ratio of x_{te} and the chord of the blade
η_{shape}	The ratio between the width of the stationer and the rotating slot
RPM	Revolution pre minute
SSB	Stall suppression blade, A.K.A. "superblade"
sw	Stationer slot width
t	Time
C_x	Axial velocity of the compressor
I_{zz}	Moment of inertia around z-axis
SF	Safety factor
Symbols	
θ	Change in angle [rad]
Δ	Change in a value
ω	Angular velocity
ρ	Density
σ	Stress

Subscript

T	Full cycle
τ_n	Portion of a cycle that the pulse modulator slots are aligned
τ	Slot on the rotating section of the pulse modulator
ψ	Slot on the stationer section of the pulse modulator
comp	Values associated with the compressor
jet	Values associated with the jet slot
pm	Pulse modulator
tip	Tip of the rotor blade
mid	Middle of the rotor blade
hub	Hub of the rotor blade
t	Thickness of retainer ring

CHAPTER I

INTRODUCTION

Problem statement

Rotating stall and surge are instabilities that have plagued jet engines since the early days of their development. With the growing need for higher efficiencies, compressors are operated closer to the surge line. The breakdown of the flow into either rotating stall or surge is undesirable for three reasons. The first reason is that they can be catastrophic to engine performance. The second reason is that they can cause rapid heating of the blades, and the third reason is that they can induce severe mechanical stresses. This research attempts to implement oscillatory blowing, which has been prove to increase the maximum C_l on stationary airfoils by 50%, onto one or more of the rotor blade surfaces; therefore, suppressing the rotating stall.

Background

In a typical compressor as the mass flow rate is reduced, there is an increase in the pressure rise. There exists a point at which the pressure rise is at a maximum, and any further decrease in the mass flow rate results in a sudden change in the flow pattern. If the mass flow rate decreases past this critical point, the compressor can enter into either rotating stall or surge. The point at which the compressor enters either rotating stall or surge is known as the surge point.[1] During stall, the flow is no longer axisymmetric but has a circumferentially non-uniform pattern of regions of separated flow that rotate around the annulus.[2] These regions of separated flow are

---

This thesis follows the style of *American Institute of Aeronautics and Astronautics*.

known as stall cells. There may be one or more stall cells, and the cells may extend from hub to casing (full-span stall) or only over part of the span (part-span stall), as shown in Figure 1.[1] Blockage created by the stall cell(s) leads to a decrease in the angle-of-attack on one side of the cell and an increase on the other. As a result, the stall cell(s) rotates around the annulus at a fraction of the wheel speed. This phenomenon, in which the total flow rate through the annulus does not vary with time, is call rotating stall. Depending on the geometry and load of the compressor, the stall could be progressive, a small drop in performance, or abrupt a very large drop in the pressure ratio and mass flow.[3] Surge is defined as the phenomenon where the net flow rate through the entire annulus varies with time.[2] Violent flow instabilities associated with surge include audible thumping and honking at inlet and exit, at frequencies as low as 1 Hz, and severe vibration.[4] A photograph of an F-4 Phantom experiencing a compressor surge is shown Figure 2. The rotation stall and the surge both no longer have axisymmetric flow but has a circumferentially non-uniform pattern of separated regions of flow, which rotate around the annulus.[2]

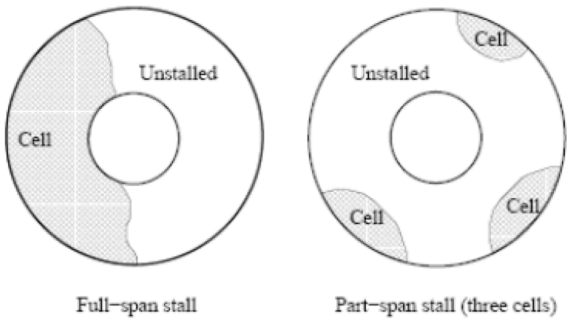

Figure 1. Full and part span stall cells

Figure 2. Back flow in the J-79 engine of an F-4 Phantom during surge

Experimental results have shown that rotating stall plays an important part in initiating a surge event, particularly for highly loaded axial compressors.[5] Consequently, the delaying of rotating stall also delays surge.

Traditional method for rotating stall suppression

Traditionally there are three methods for suppressing the onset of rotating stalls and surge. These traditional methods are briefly described in this section.

The bleed air off-take method allows compressed air to bleed out of the compressor. This bleeding of air effectively reduces the mass flow rate of the compressor and thereby reduces the compression ratio. This reduction in compression ratio is what suppresses the rotating stall. Bleed air off-take is an effective method of flow instability suppression; however, this method wastes energy by compressing air that is not used in power generation.

Casing air injection upstream of the blade tip has also been used to suppress instabilities. This method effectively reduces the tip clearance between the casing and the blades; thereby, increasing the maximum angle-of-attack the blade can operate at. Casing air injection works best for compressors that have instabilities near the tips of the blade. Air injection at the tip is not a viable option for compressors operating at part speed for extended periods of time because the aerodynamic performance of the compressor is reduced due to the efficiency penalty incurred by using tip injection.[6]

The most commonly used stall suppression method is done by actively controlling the variable inlet guide vanes (IGVs) and variable stator vanes. A photograph of Dr. Cizmas's jet engine at Taxes A&M University gives a good example of complexity of variable stator vanes, as shown in Figure 3.

These variable vanes suppress the rotating stall by reducing the angle-of-attack of the entire stage of the compressor. Active control of the vanes adds additional

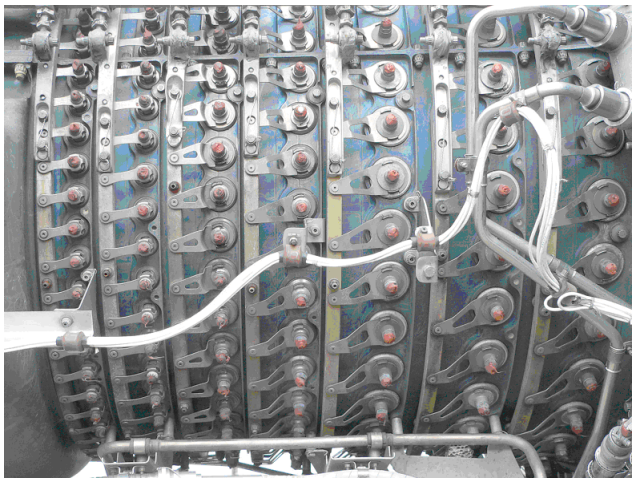

Figure 3. Photograph of variable inlet and stator vanes

power requirements for the engine, increases the total weight and complexity of the compressor. There is also a possibility that a malfunction in the IGVs could lead to a severe drop in engine performance.

New stall suppression system

The new method for rotating stall suppression currently under development uses pulse-width modulated injection along the span of one or more rotor blades. The rotor blade in which the jet actuation takes place is known as the stall suppression blade (SSB). Actuation flow control techniques have been shown to effectively control flow separation with lower required energy input than that of steady blowing or suction.[7- 8- 9] The injected air will energize the boundary layer of the SSB and reattach the stall cell. Gilarranz et al. showed that the stall angle-of-attack of a wing-section is increased through oscillatory blowing, as shown in Figure 4.[10]. An additional benefit of the new suppression system is that it is fail-safe, in that there are no complex moving parts.

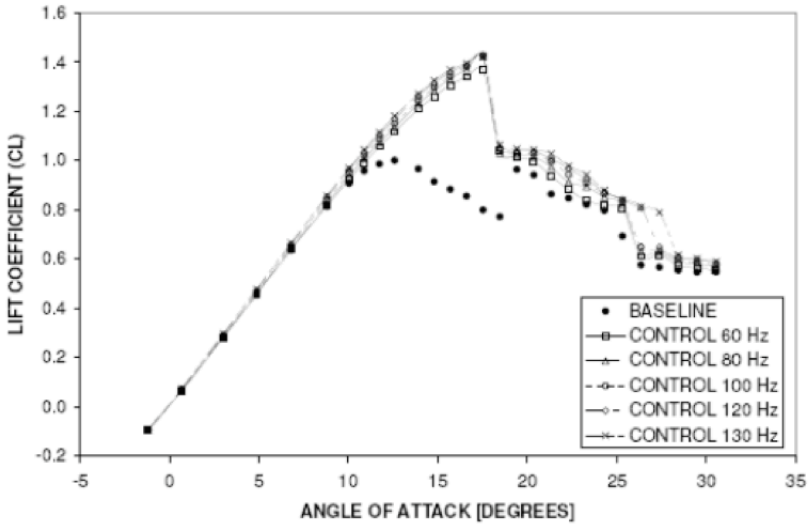

Figure 4. CL versus angle-of-attack with and without oscillatory blowing

Original contributions

The original contribution of this research is to do a detailed design of the axial compressor. This compressor will be used to study rotating stalls and different stall suppression methods.

Along with the overall design of the compressor, this research was targeted at designing, building and testing a scaled down version of the oscillatory blowing system. The flow characteristics of this scaled oscillatory blowing system was studied by developing three experimental setups. The first experiment allowed the system to be tested at a wide range of frequencies. The second experiment used a hot-wire anemometer to measure the jet slot velocity along in the span. The third experiment required a small wind tunnel to be designed and built around the pulsing system. This wind tunnel allowed effectiveness of the pulsing system to be directly measured on an airfoil section.

Summary of work

Four of the design stages have been completed. The first design stage was to design a drive system, a throttle system, and a frame for the compressor. The first stage also required that the disk/pulse modulator and the Type I blade be designed. This required an understanding of the internal plenum and the manufacturing techniques that were going to be used. The first stage also required a preliminary airfoil geometry to be developed for the blades, which was done by Forrest Carpenter, a Ph.D. student.

The second design stage required the Type I blade be built and tested. The testing included a structural test and an aerodynamic analysis using computational fluid dynamics (CFD), which was done by Carpenter. The second stage also required the design of the Type II blade. This was done using the lessons learned from the Type I blade design.

The third stage included an analysis of the structure of the disk and the Type II blade. this was done using a finite element model of each component.

In the fourth stage, a scaled down pulse modulator was built and its flow characteristics were tested. The fourth design stage also required a wind tunnel be design and built around the scaled down pulse modulator, which was used to study the effectiveness that pulse modulated blowing had on the lift characteristics of an airfoil section. All of the design stages in this project are shown in the flowchart in Figure 5. The green boxes indicate a completed task. The yellow boxes were completed by Carpenter.

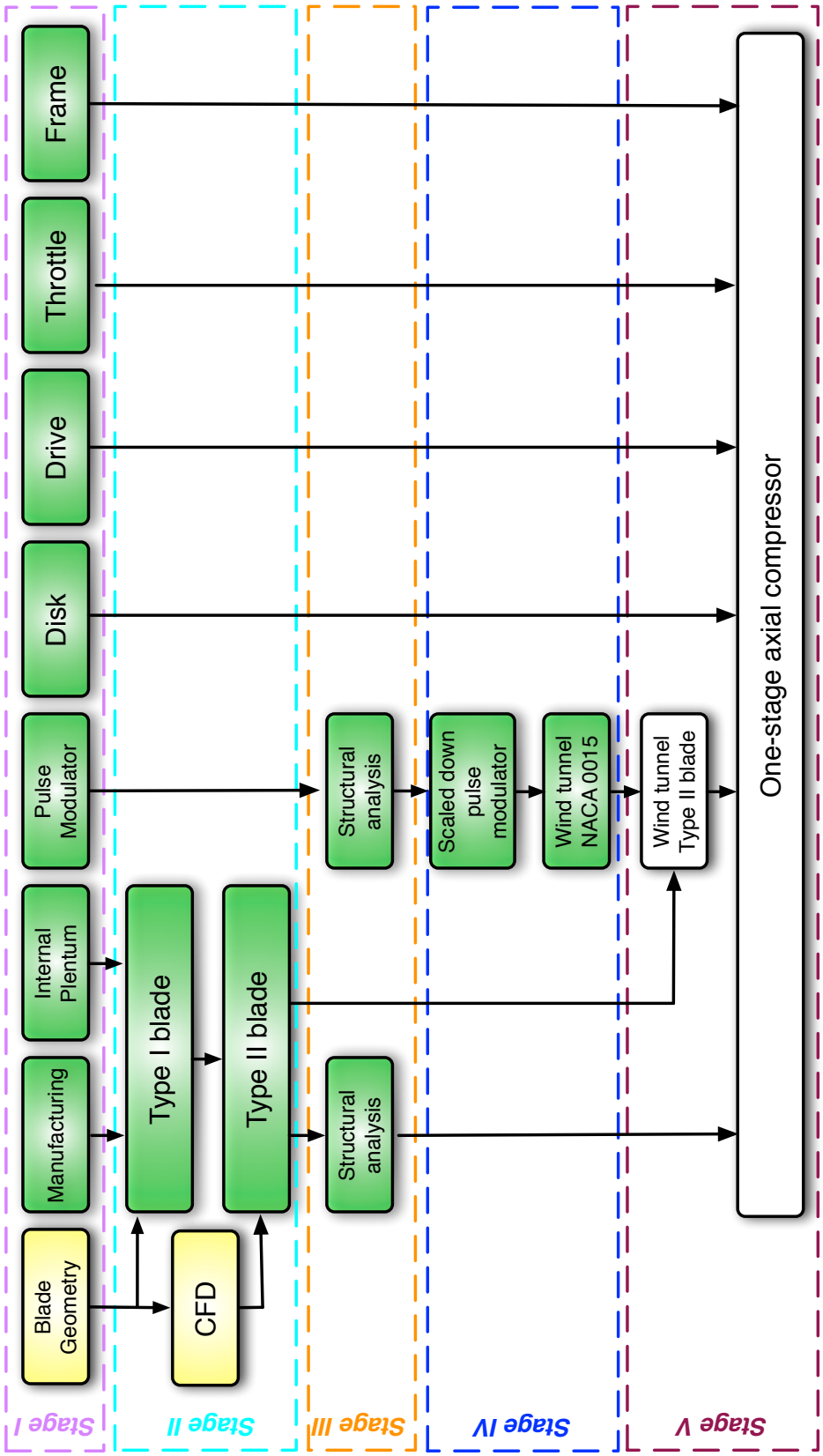

Figure 5. Flow chart of design stages

CHAPTER II

COMPRESSOR DESIGN

A one stage axial compressor was designed to test the new pulse modulated stall suppression system. This chapter describes the design of each of the subsystems used in the compressor. A brief description of each subsystem is listed bellow.

- The frame: used to mount and align all the subsystems
- The casing of the compressor: is the housing for the compressor, and holds the disk, blades, and pulse modulator.
- The throttle: controls the mass flow through the compressor, thus aids in producing rotating stalls.
- The drive system: Drives the compressor at a speed of 3500 RPM.
- The disk: Is the outer portion of the pulse modulator and holds the blade.
- The blades: responsible for the pressure rise in the compressor.
- The pulse modulator: is the stationary portion of the disk, and provides pulsing air to the SSB.

The following sections give a detailed descriptions of the design of each of these subsystems.

Compressor frame

A frame was designed and built for three reasons. The first reason a frame was needed was to mount all the subsystems on a central structure. This central structure would

maintain the alignment between the subsystems. The second reason was to raise the compressor inlet away from the ground, which will allow clean flow to enter the compressor. The third reason a frame was needed was to give the removable front of the compressor a track to roll on while staying aligned with the subsystems. The frame was constructed out of I-beam, square beam, and steel pipe, as shown in Figure 6. The finished frame is shown upside down in Figure 7.

Figure 6. Photograph of frame being constructed

Figure 7. Photograph of finished frame

Compressor casing

The casing that is used in the compressor was built by Westinghouse and donated to Texas A&M University. The casing is shown in Figure 8. The compressor casing consists of four major sections. The first section is composed of six aluminum bulkheads, which form the outer casing of the compressor. The second section is the plexiglass test section. The third section is the internal casing, which is a 10 inch diameter aluminum pipe that is supported by several rods that run from the outer

casing to the internal casing. The fourth section is the inlet, which consists of an inner and outer casing section. The internal casing has bearings along the central axes of the compressor. These bearing support the front and back of the drive-shaft, which is rigidly mounted to the disk. The inlet and two of the aluminum bulkheads are mounted on rollers. These rollers allows the front part of the compressor to be easily rolled out of the way. This removable compressor front allows easy access to the rotor and instrumentation.

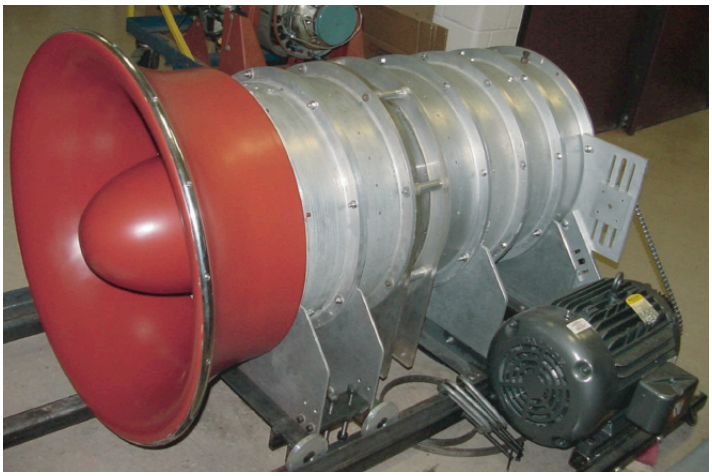

Figure 8. Photograph of the compressor casing

The compressor casing includes a 101.6 millimeter (4 in) long test section. This one stage axial compressor was modified to have 16 inlet guide vanes, 25 rotor blades, and 32 stator vanes. The compressor has an inner and outer diameter of 304.8 millimeters (12 in) and 508.0 millimeters (20 in) respectively. The blades have a span of 101.6 millimeters (4 in).

Throttle system

The throttle system was designed so that the mass flow rate through the compressor could be controlled while the compressor is in operation. The mass flow rate is controlled by varying the exit area of the compressor. This was achieved through the development of two components: (1) the throttle rack and (2) the throttle carriage, both shown in Figure 9. The throttle rack is a frame that supports, guides, and controls the throttle carriage. The throttle rack guides the throttle carriage using four linear bearings. The throttle carriage is controlled by a stepper motor and ball screw assembly that is attached to the rack and to the throttle carriage. The cone is mounted to the throttle carriage and moves forward and aft to control the exit area of the compressor. The fully constructed and a fully assembled throttle system is shown in Figure 10.

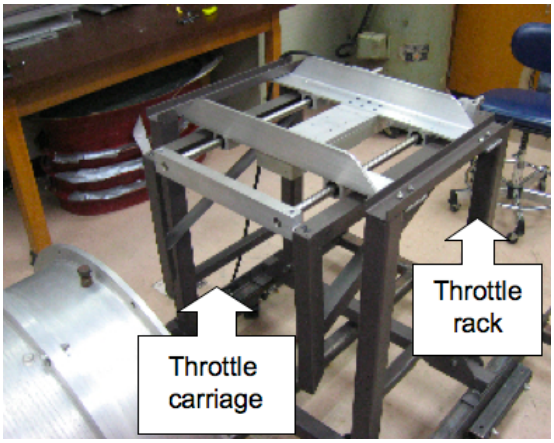

Figure 9. Photograph of the assembled throttle mechanism

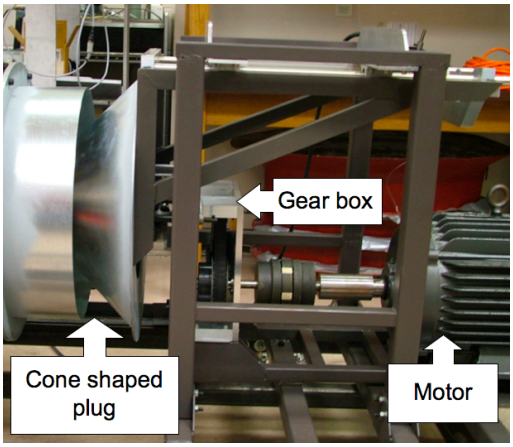

Figure 10. Photograph of the assembled throttle system

The exit area can be calculated with Equation (2.1). Where x is the linear distance the throttle is open and θ is the angle from the horizontal to the cone wall.

$$A = \frac{\pi x \tan(\theta)}{\cos(\theta)}(R - \frac{x}{4}\tan(\theta)) \tag{2.1}$$

Drive system

The drive system was designed to allow the drive shaft to pass through the center of the throttle system. The drive system consists of a mounting frame, drive shaft, a gearbox, and the electric motor. The frame was machined to ensure that the motor would align with the gearbox. A drawing of the motor and the motor mount is shown in Figure 11.

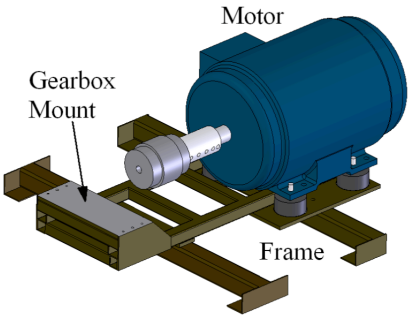

Figure 11. Frame and motor drawing

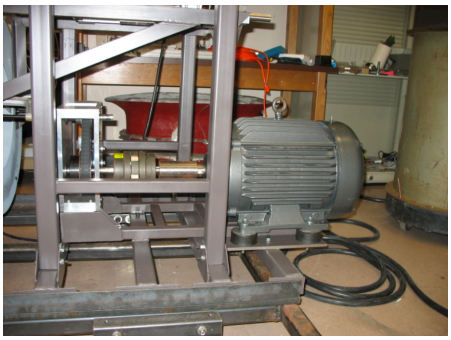

Figure 12. Photograph of drive system

The proper alignment between the gear box and motor was verified through the use of an indicator during the final assembly process. A belted-gearbox was constructed out of aluminum. The benefits of using a belted-gearbox are: (1) sound reduction and (2) gearbox wear is limited to the belt only. The gearbox has a two-to-one gear ratio. A drive shaft passes through the center of the throttle cone and connects the gearbox to the compressor shaft. The compressor is currently powered by a 20 horsepower electric motor. The assembled system is shown in Figure 12.

Blades

There are two Types of blades designed for the compressor. The first type of blade was designed using a combination of aluminum, steel, and plastic. The second blade design is machined out of a solid piece of aluminum.

Type I blade

The first blade design was developed using the preliminary airfoil blade geometry developed by Forrest Carpenter, a Ph.D. student. This blade had an aluminum dovetail mounting portion that was machined to fit into the old design of the disk. This dovetail mount is shown in Figure 13 and Figure 14.

a Manufacturing of Type I blade

The airfoil section of the blade was a combination of rapid prototype (RP) material and steel reinforcement. This blade was designed to take advantage of the ability of the RP machine to easily manufacture complex geometries, such as the airfoil section of the blade. The steel reinforcement was added to insure that the blade would withstand the centrifugal forces applied to it in the compressor.

The dovetail mounting was made in the CNC mill. The geometry of the dovetail made it difficult to measure to the dimensions of the dovetail accurately. This was overcome by making go/no-go gages, which are the brass parts shown in Figure 14. The alignment of each side of the dovetail attachment must be maintained throughout the gaging process. This was achieved by using the fourth-axis on the CNC mill, which allowed all sides of the dovetail to be machined without removing it from the machine.

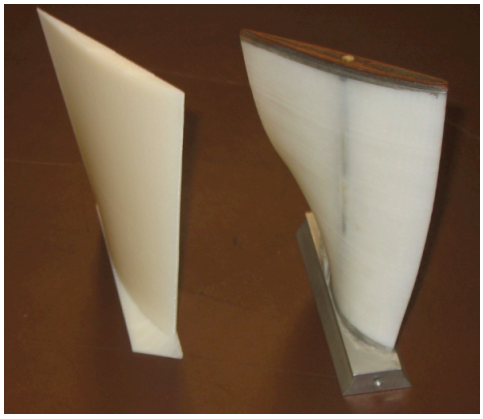

Figure 13. Photograph of the finish Type I blade

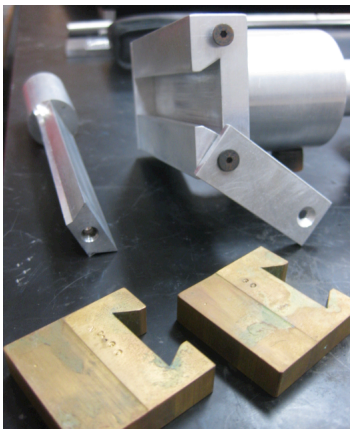

Figure 14. Photograph of Type I blade parts

b Structural testing of Type I blade

There were two difficult parts to the structural analysis. The first was the non-isotropic characteristics of the RP material. The second is the modeling of the steel reinforcement of the blade. Due to the complexity of the structural analysis required to accurately predict the stresses in the blade it was decided that a structural test would be easier and less time consuming. The test conducted on the Type I blade is shown in Figure 15. This test entailed building a mounting dovetail-slot similar to the one in the old disk design. The mounting dovetail is shown in Figure 14. This mounting dovetail-slot which would hold the blade would be mounted to a boring bar and would be spun to 1.5 times the RPM of the compressor. This was done in the CNC mill which was outfitted with a safety shield. The safety shield would protect the machine from damage during the testing. The blade was spun to 1.5 of the RPM of the compressor for an extended period of time and showed no structural damage. This gave a safety factor higher then 1.5 due to the nonlinear forces acting on the blade.

c Summary of Type I blade

Even though the airfoil geometry of the blade was easy to build, manufacturing the dovetail mount portion of the blade proved to be very difficult. There were also serious doubts about being able to make this Type of blade into a SSB. This difficulty in manufacturing and the uncertainty of the SSB blade design lead to a new blade design.

Figure 15. Blade test setup in CNC mill

Type II blade

The Type II blade design was developed for four reasons. The first reason was to implement the finalized airfoil geometry which Forrest Carpenter developed and analyzed using CFD. The second reason the Type II blade was designed was to make the blade easily modifiable into the SSB. The next benefit of the Type II blade was to allow a structural analysis to be conducted on the blade. The fourth reason the new Type II blade was designed was to improve the blade mounting system.

The all-aluminum Type II blade design allowed the SSB to be made using a 5-axis wire EDM, which would be used to make the internal plenum and the jet slot

in the blade.

The structural analysis could be conducted on the blade due to the isotropic characteristics of aluminum. This analysis is described in detail in the following section.

The new blade mounting design used two retainer rings to hold onto the mounting flanges of the blade. There was a transition flange that smoothly transitioned from the disk to the airfoil section. These mounting and transition flanges are shown in the drawing of the blade in Figure 16 and Figure 17. The design greatly reduced the manufacturing complexity of the mounting portion of the blade. This mounting design is presented in detail in the disk design chapter.

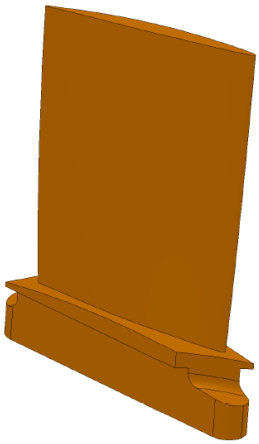

Figure 16. Side view of Type II blade

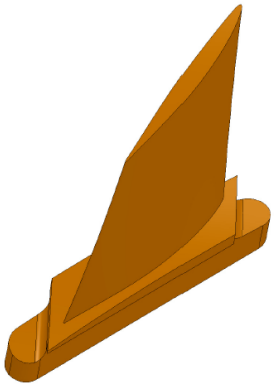

Figure 17. Top view of Type II blade

a Manufacturing Type II blades

The Type II blade was machined using the 4-axis CNC mill, shown in Figure 18. A MatLab code was written to machine the surface of the blade using a 1 inch ball-nose

end-mill. The G-code was developed from the coordinate files that where provided by Carpenter. An airfoil section of the blade was manufactured to test the g-code. This prototype of the airfoil is shown in Figure 19 and Figure 20. The airfoil section took 3.5 hours to machine; therefore, a full set of rotor blades could be manufactured in less then two weeks.

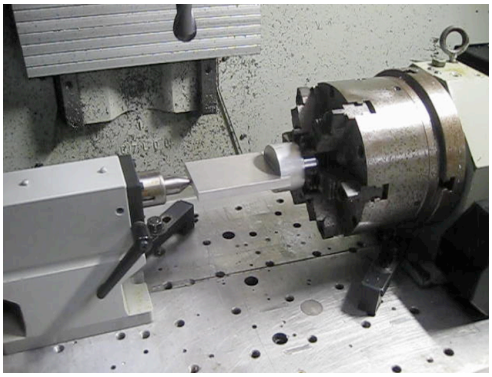

Figure 18. Pre-machined aluminum mounted in 4-axis CNC mill

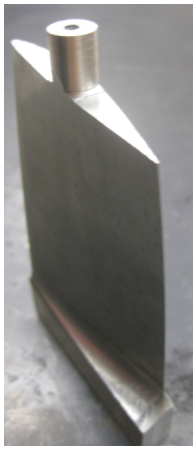

Figure 19. Top view of finished airfoil section of Type II blade

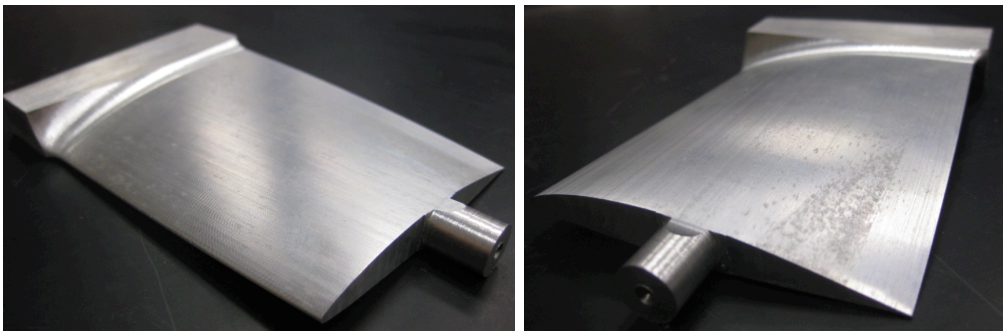

Figure 20. Photograph of finished airfoil section of the Type II blade

Pulse modulator

The pulse modulator has two purposes. The first purpose is to channel the high pressure air from the stationary supply line to the rotating SSB. The second purpose is to convert the steady air supply to an oscillating supply which will then be channeled into the plenum of the SSB.

The pulse modulator was design to have two portions, which are the stationary (pulse modulator) and the rotating portion (disk casing). The exploded view of the stationary portion is shown in Figure 21. The high pressure air supply enters though the front of this stationary portion. The holes around the perimeter of the stationary portion periodically lineup with the slots in the disk casing. This periodic alignment causes the air to pulse in the disk casing. The disk casing channels this pulsing air to the SSB, which is shown in Figure 22. This disk casing has a housing plate that prevents high pressure air from leaking out of the system.

Minimizing the volume from were the pulse was generated to were it gets injected into the free-stream proved to be a unique challenge. This volume would have an adverse effect on the frequency response of the system. This volume could be reduced by increasing the diameter of the stationary portion of the pulse modulator. However, this increase in diameter would force the adjacent surfaces to a high relative speed. This relative speed is referred to as relative velocity (RV). Both the volume and the RV are plotted verses the radius of the stationary portion of the pulse modulator and is shown in Figure 23.

The pulse modulator was designed to operated at high RV for an extended period of time. This was achieved by eliminating the need for seals, in the pulse modulator. By eliminating the seals the two surfaces would never come in contact; therefore, the RV would be irrelevant. This would force the two sections of the pulse modulator to

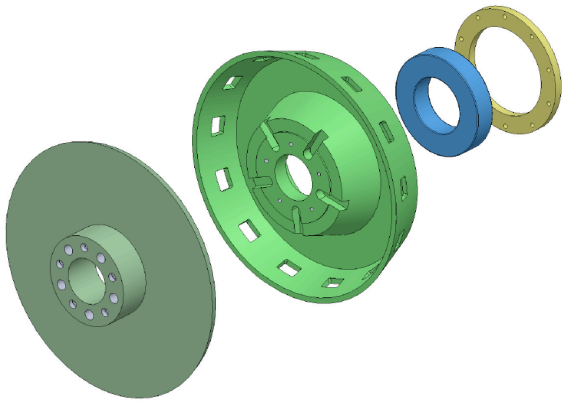

Figure 21. Exploded view of the inner portion of the pulse modulator

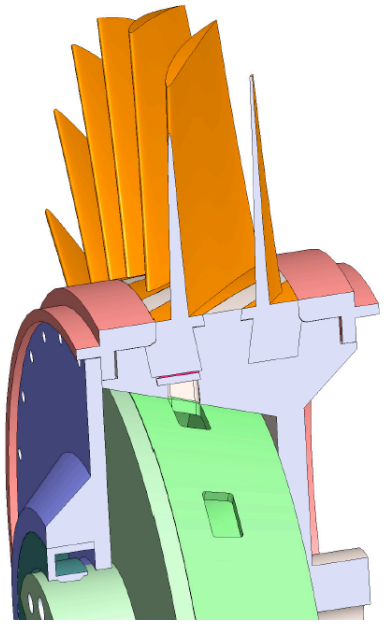

Figure 22. Cut view of the pulse modulator

have a small gap between them.

The gap between the stationary and rotating portions of the pulse modulator is critical to minimize the leakage into the rotating portion when the slots are not aligned. This leakage directly affects the minimum velocity that is injected for the SSB during one cycle. This gap is estimated to be between .05-.08 mm (.002-.003 inch). The inner and outer portion of the pulse modulator have a cone shape intersection. This type of intersection was chosen to allow very fine adjustments to be done to the gap by changing the shim between the inner and outer portions of the pulse modulator. This shim will change the height of the inner portion, thus increasing the gap.

The angle of the cone was chosen to divide the change in the shim by three, which allowed finer adjustments to be done relatively easily. The alignment between

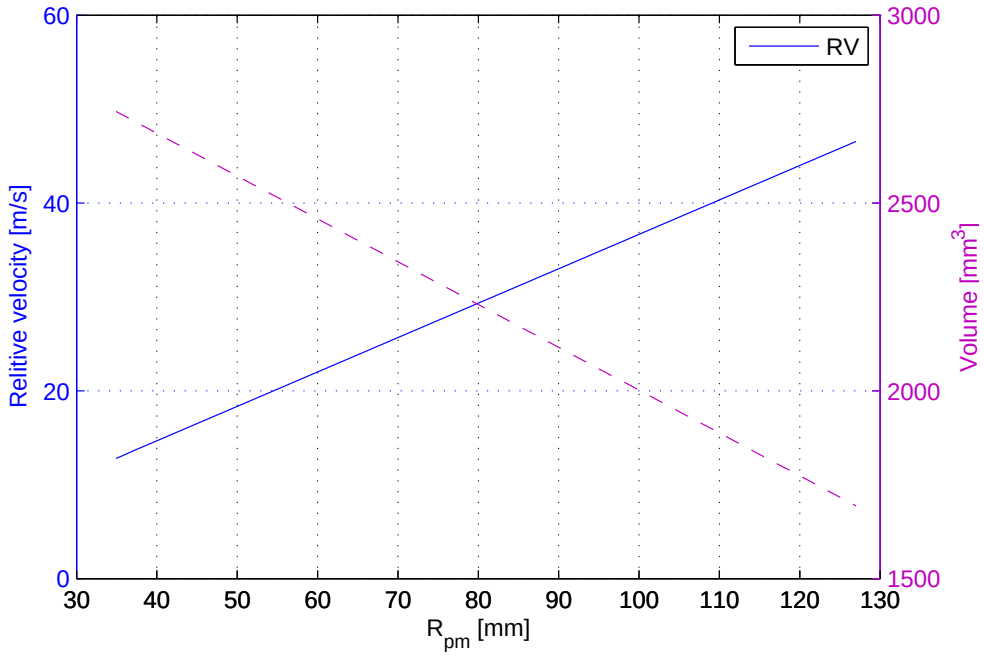

Figure 23. Comparing RV and internal plenum volume

the rotating and stationery portions of the pulse modulator is maintained using a large sealed ball bearing. This alignment is critical due to the small gap between the two surfaces. To eliminate any imperfection or misalignments the shim would be removed and the inner and outer portion would be honed together.

Dimensionless parameters

There are four dimensionless parameters that are used to describe the quality of the oscillatory supply. The first is a dimensionless frequency called the F^+ number, and defined in Equation (2.2).[11]

$$F^+ = \frac{f_{jet} x_{te}}{U_\infty} \tag{2.2}$$

The second parameter is the momentum ratio between the free stream and the injected air which is called C_μ, and is defined in Equation (2.3).[12].

$$C_\mu = \frac{2\, h \rho_{jet} V_{jet}^2}{C \rho_\infty U_\infty^2} \tag{2.3}$$

The third parameter is the Duty Cycle which will be denoted as DC, and is defined in Equation (2.4).

$$DC = \frac{T_{on}}{T_{total}} \tag{2.4}$$

The fourth parameter is the shape factor, η_{shape}, which describes the shape of the pulse. The shape factor is the ratio between the angle of the rotating and stationary slots in the pulse modulator, and is defined in Equation (2.16).Pulses with different η_{shape} are shown in Figure 24.

$$\eta_{shape} = \frac{\theta_\tau}{\theta_\psi} \tag{2.5}$$

Geometry and design parameters

This section will describe the relationship between the design parameters and the geometry of the pulse modulator. There are three design parameters used to design the pulse modulator:

1. The F^+ Number, which is a dimensionless frequency.
2. The Duty Cycle DC, which is the ratio between the pulse being on and off respectively.
3. The shape factor η_{shape} which describes the pulse shape.

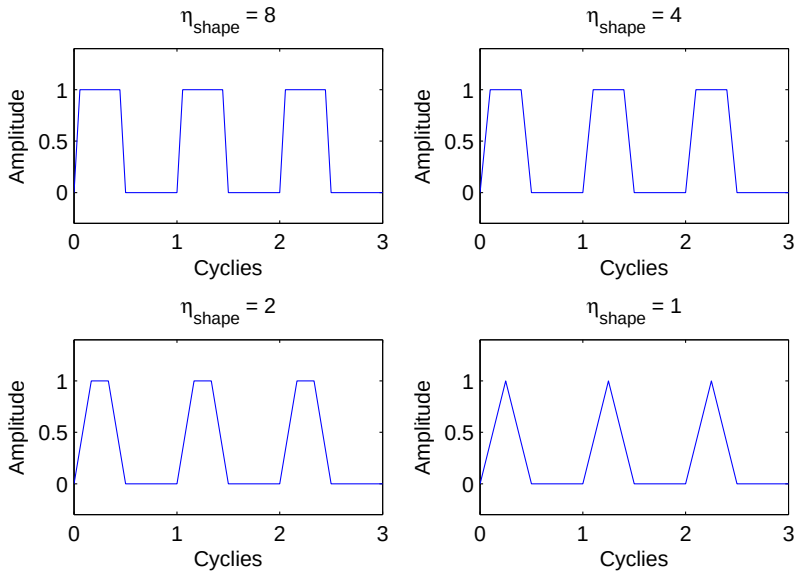

Figure 24. A plot of pulse shape with $DC = 0.5$

a F^+ number

The jet frequency (f_{jet}) can be solved for by rearranging Equation (2.2), which yields Equation (2.6)

$$f_{jet} = \frac{U_\infty F^+_{desired}}{x_{te}} \tag{2.6}$$

where U_∞ is the local free stream velocity that the blade sees, and x_{te} is the distance from the trailing edge to the jet slot location. The local free stream is the hypotenuse of the axial velocity and the angular velocity at a specific radius. This is shown in Equation (2.7).

$$U_\infty = \sqrt{{C_x}^2 + (f_{motor} 2\pi R_{blade})^2} \tag{2.7}$$

The distance from the trailing edge to the jet slot (x_{te}) is described in Equation (2.8), were $\Re$ is the ratio of x_{te} over the chord of the blade.

$$x_{te} = C\Re \tag{2.8}$$

The change in local $F^{+}_{desired}$ and U_{∞} as a function of R_{blade} is shown by Figure 25.

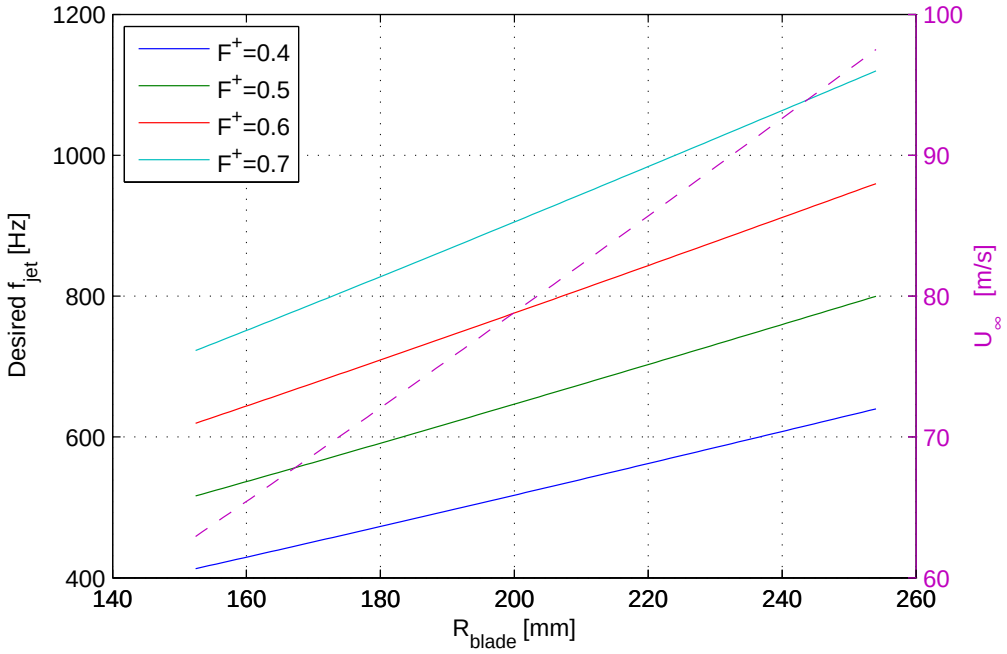

Figure 25. Desired f_{jet} and U_{∞} vs. blade radios

The number of slots, $n_{jet\,slot}$ in the rotating portion of the pulse modulator is the ratio between the desired frequency of the jet, f_{jet}, and the frequency of the compressor, f_{comp}

$$n_{slot} = \frac{f_{jet}}{f_{comp}} \tag{2.9}$$

where f_{comp} is the compressor RPM divided by 60. The value of n_{slot} is then rounded

to the nearest integer. The actual F^+ number is then calculated using this integer value with Equation (2.10)

$$F^+ = \frac{f_{comp} n_{slot} C \Re}{U_\infty} \tag{2.10}$$

b Duty cycle

The DC is a kinematic relationship between the rotating and the stationary slots. This relationship can be shown by dividing Equation (2.11) with Equation (2.12), which were derived using the relationship between angular velocity and tangental velocity.

$$\dot{\theta}_{\tau_n} R_{pm} = V \Rightarrow \Delta\theta_{\tau_n} R_{pm} = V \Delta t_{\tau_n} \tag{2.11}$$

$$\dot{\theta}_T R_{pm} = V \Rightarrow \Delta\theta_T R_{pm} = V \Delta t_T \tag{2.12}$$

This division of Equation (2.11) with Equation (2.12) yields Equation (2.13), which shows the relationship between the angle (θ) and the DC

$$\frac{\theta_{\tau_n}}{\theta_T} = \frac{t_{\tau_n}}{t_T} = DC \tag{2.13}$$

Drawings of the angular and time relationships are shown in Figure 26 and Figure 27 respectively

$$\theta_T = \frac{2\pi}{n_{slot}} \tag{2.14}$$

where θ_T is defined in Equation (2.14). The rotating and stationery slot angles can be summed to get θ_{τ_n}. By subbing Equation (2.14) and the relationship between the rotating and stationery slot angles into Equation (2.13) allows the DC to be written

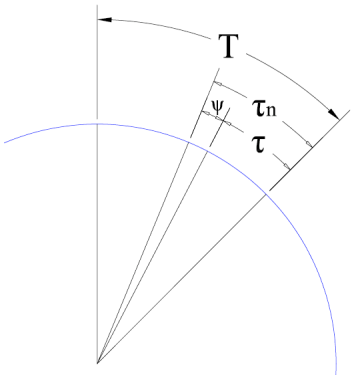

Figure 26. Relationship between DC and θ

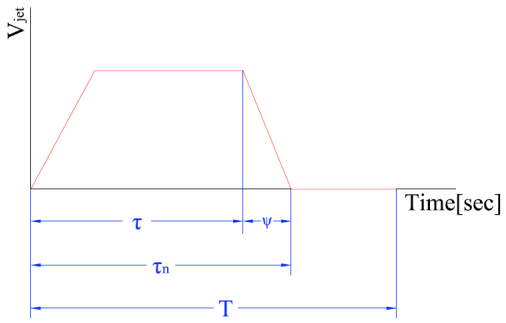

Figure 27. Drawing of the relationship between DC and time

as Equation (2.15).

$$DC = \frac{n_{slot}(\theta_\psi + \theta_\tau)}{2\pi} \tag{2.15}$$

c Shape factor η_{shape}

The shape of the pulse is a result of the rotating and stationery slots coming into alignment, and is described by Equation (2.16). The larger the value of η_{shape} the less effect it was on the pulse.

$$\eta_{shape} = \frac{\theta_\tau}{\theta_\psi} \tag{2.16}$$

The stationery slot width is limited by machinability of a small slot; therefore it is covenant to used slot width (sw) to describe θ_ψ. The relationship between the sw and θ_ψ is shown in Equation (2.17). This slot is small relative to the radius of the pulse modulator; therefore, small angle theory is used to simplify this equation.

$$\theta_\psi = 2\sin\left(\frac{sw}{2R_{pm}}\right) \approx \frac{sw}{R_{pm}} \tag{2.17}$$

By combining Equation (2.15), Equation (2.16), and Equation (2.17) the shape factor can be rewritten into Equation (2.18).

$$\eta_{shape} = \frac{2\pi DC\, R_{pm}}{n_{slot} sw} - 1 \tag{2.18}$$

It is apparent that larger values of DC and R_{pm} and smaller values of sw and n_{slot} will result in a high value of η_{shape}. The n_{slot} is directly related to the F^+ Number and is shown in Equation (2.9). The rationale for choosing each one of these values is listed below.

- DC: a value of 0.5 was estimated to provide adequate C_μ values; however, the value for DC could be optimized at a later time.
- F^+: The effective range of the F^+ numbers is approximately between 0.5-1.5 or 0.3-3.[11- 13]. Therefore, a low F^+ Number of 0.47 at the tip was chosen.
- sw: The slot width was set at the low limit due to manufacturing constraints; therefore, the minimum sw was chosen, and is 3.56 mm.
- R_{pm}: due to the geometry and structural constraints of the compressor disk the upper limit was chosen (115.75 mm).

All of the values used in the pulse modulator design are listed in Table I.

Table I. Values used in pulse modulator design

F^+	0.47
DC	0.5
η_{shape}	6.87
RPM_{comp} [rev/min]	3500
f_{comp} [Hz]	58.33
f_{jet} [Hz]	758.3
C [m]	0.076
$\Re$	0.8
n_{slot}	13
C_x [m/s]	29
sw [mm]	3.56
$R_{blade\,tip}$ [m]	0.254
$R_{blade\,hob}$ [m]	0.1524
R_{pm} [in]	0.1157
θ_{τ_n} [deg]	13.85
θ_τ [deg]	12.087
θ_ψ [deg]	1.76

Disk

The disk design is important in insuring safe operation of the compressor. The disk is responsible for holding the blades while the compressor is being operated. The disk is also an essential part of the pulse modulator. The disk was designed to be manufactured in the Aerospace Engineering Machine Shop, AEMS: this required that the design be tailored to the machinery and equipment available in the AEMS.

The disk consists of two parts, which are shown in an exploded view in Figure 28. The biggest part is the disk casing, which is shown in gray in Figure 28. The next part of the disk is the two retainer rings, which are shown in red in Figure 28. This retainer ring design was chosen to simplify the disk design. The rings are the primary structural component of the disk design which allows two benefits. The first is that the disk casing has minimal structural requirements which allows the casing to be manufacture out of aluminum. This design also simplified the structural analysis of the disk. This simplification was accomplished by eliminating the complex geometry of the casing for the structural analysis.

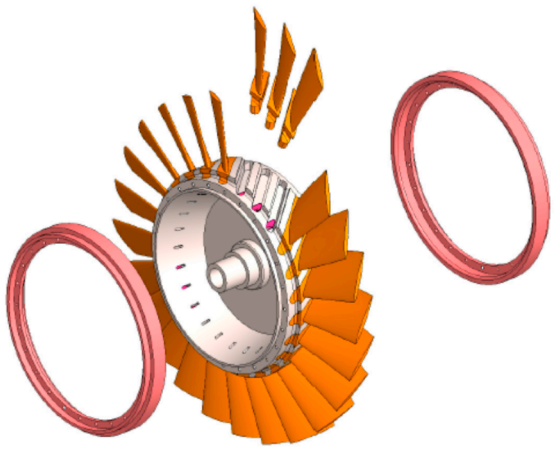

Figure 28. Exploded view of disk assembly

The casing has three purposes. The casing serves as the rotating portion of the pulse modulator and channels the pulsing air to the SSB. The stationary portion of the pulse modulator mounts to the inner cavity of the disk; consequently, the disk is responsible for the alignment between the rotating and stationary portions of the pulse modulator. The casing is also responsible for holding the blades at the right stager angle and perpendicular to the surface of the disk. Each blade mounting cavity has two counter bores, which are shown best by Figure 29 and Figure 30. The deepest counter bore maintains the blade alinement. The counter bore is the critical portion for the blade mounting cavity. The second counter bore is wider and accommodates the transition flange on the blade; therefore is less critical. The transition flange counter bore is designed such that it will not touch the transition flange. The no-contact design simplifies the structural analysis and the manufacturing of the disk casing.

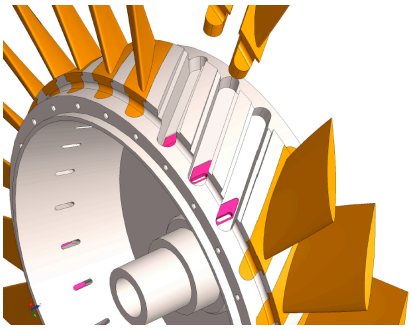

Figure 29. View of gaskets in the blade mounting cavities

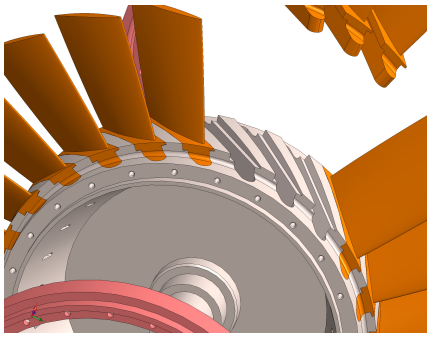

Figure 30. View of blade mounting cavities in disk casing

The disk was designed in a way that all of the blades could be substituted for SSBs. Inside each of the blade mounting cavities is a gasket which seals the channeled pulsing air from leaking between the casing and the blade. The gasket are shown in

purple in Figure 29. This gasket can also be used as a on-off-switch. The switch works by rotating the gasket 180 degrees, and thereby blocking the flow from the casing to the SSB. This type of design was chosen to allow optimization experiments to be done on the number and location of the SSBs. This design will minimize the change in the balancing of the disk while testing different configurations.

The retainer rings are responsible for holding the blades in position on the disk. The retainer rings design is such that they slide onto the disk casing; thus, over the front and rear of the blade mounting flanges, as shown in Figure 31. The retainer rings are held onto the disk casing by a series of bolts that connect the retainer rings to the disk casing. The retainer rings also help seal the disk with the internal channel of the compressor casing. The sealing is achieved by having a front and rear flange that is overlapped by the internal channel of the compressor: this is shown in Figure 32. The retainer rings have the same number of bolt holes as the number of blades. This configuration was chosen for two reasons: (1) to center the bolt between the blade mounting cavities in the disk casing, and (2) to provide the retainer ring with a load symmetry around each blade contact point (pressure pad) and bolt hole.

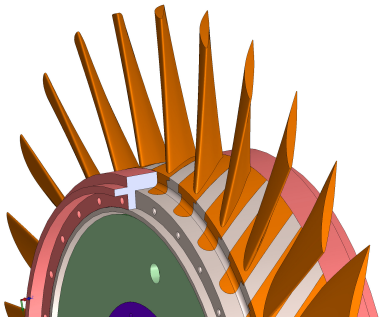

Figure 31. Cut view of the ring on the disk

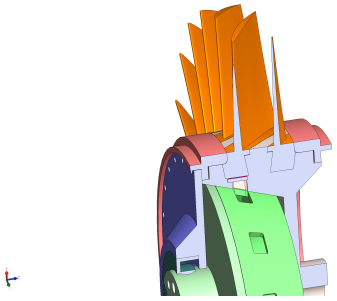

Figure 32. Cut view of the disk and pules modulator

Summary

This chapter described in detail the design of the one stage axial compressor, which consists of several subsystems. The frame, throttle, and drive systems have been built for the compressor; however, the disk, blades, and pulse modulator were more formidable and needed to be more closely analyzed or tested.

The structure of the disk and the blades will need to be analyzed to ensure that the structure will withstand the centrifugal forces that are to be experienced during compressor operation. These analyses are described in detail in the next chapter.

The design of the pulse modulator was described in this chapter; however, due to the complexity of the flow through the pulse modulator it was decided that a scaled down pulse modulator would be built and tested. These tests will give an insight to the sensitivity of different parameters used in the design phase.

The completed subsystems are assembled and shown in Figure 33.

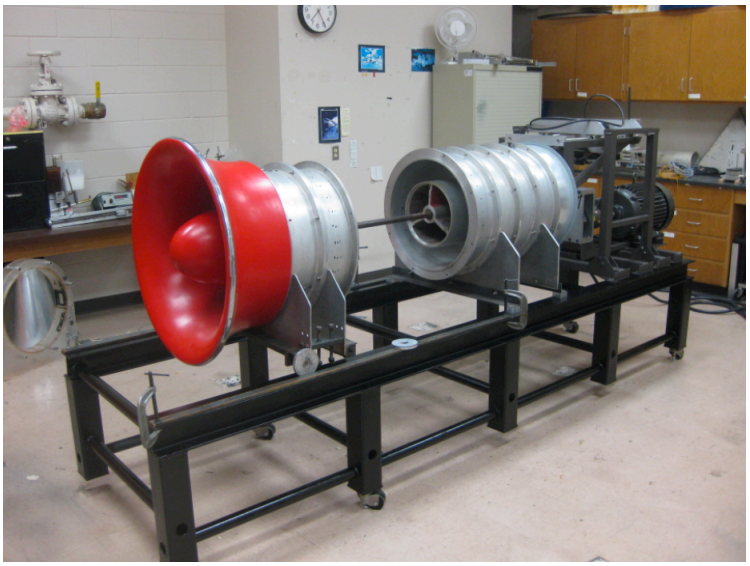

Figure 33. Photograph of the asssembled compressor

CHAPTER III

STRUCTURAL ANALYSIS

This chapter describes the structural analysis conducted on the blades and retainer rings of the disk. Both the blades and the rings were analyzed analytically and using a finite element model.

Structural analysis of Type II blade

The structural analysis of the Type II blade design was done analytically and using a finite element model in ABACUS.[14]

Material selection

The material selected for the Type II blade was 6061-T6 aluminum. This type of aluminum was chosen for its low density and high yield and fracture stresses, which are listed in Table II along with the Young's Modulus and yield shear stress.[15] This material was also chosen for its machinability, which is listed as 50% compare to other aluminum alloys.[15] The last column in Table II specifies the units used in ABACUS, which will be explained in a later section.

Analytical structural analysis

The Type II blade was analyzed using beam theory. The first step was to calculate the centrifugal force, F_c, acting on the blade. This required the cross sectional area as a function of radius. This was done by cutting the SolidWorks blade model into 150 sections and measuring the cross section and radius at each cut. Simpson's rule was used to approximate Equation (3.1) which calculates the centrifugal forces as a

Table II. Aluminum 6061-T6 material properties

σ_{yield}	276	MPa	40,000	psi	276,000	kg/(mm s^2)
σ_{max}	310	MPa	45,000	psi	310,000	kg/(mm s^2)
E	68.9	GPa	9.99×10^6	psi	68.9×10^{-6}	kg/(mm s^2)
ρ	2,700	kg/m^3	0.0975	lb/in^3	2.7×10^{-6}	kg/(mm s^2)
$Shear_{yield}$	207	MPa	30,000	lb/in^3	207,000	kg/(mm s^2)

function of radius, where N is the number of sections measured.

$$F_{c_i} = \rho\omega^2 \int_{r_i}^{r_{tip}} A(x_i)\, x_i\, dx \qquad i = 1, 2, 3, ..., N \tag{3.1}$$

The cross sectional area and the centrifugal force is plotted in Figure 34.

The stress in the blade was calculated assuming the blade was a simply supported beam. This configuration is shown in Figure 35. There are three assumptions made in this analysis. The first is that the F_c is distributed evenly across the bottom of the blade. This assumption was an approximation used to simplify the calculations. The second assumption is that the blade is pinned between the front and rear contact points of the blade. This pin assumption is a good approximation for this mounting configuration. The third assumption is that the blade is a beam with a constant I. This assumption ignores the structure of the airfoil section of the blade and only uses the mounting portion to calculate the stress.

The stress was calculated using Equation (3.2).[16]

$$\sigma_{xx\,i} = \frac{F_{dist} L^2(y_i)}{8 I_{zz}} \tag{3.2}$$

where y_i is distance from the centroid of the of the mounting portion of the blade;

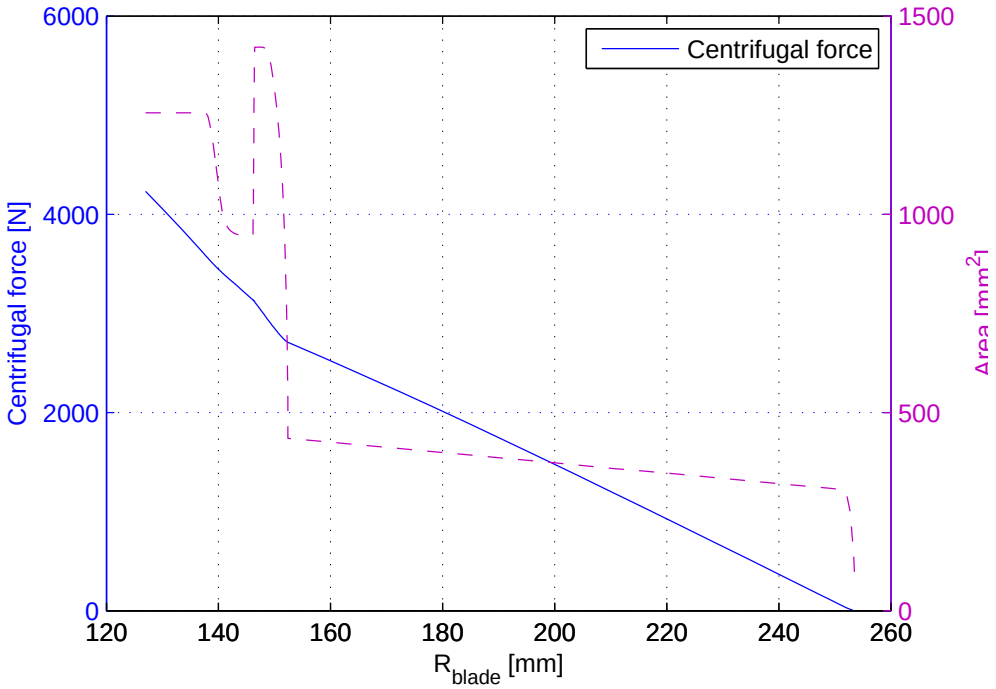

Figure 34. Plot of the centrifugal force and cross sectional area of the blade

therefore, i is ether the top or the bottom of the mounting flange. The values used in this stress calculation are shown in Table III.

The results from the analytical structural analysis are shown in Table IV.

FEA of blade

A FEA model was developed in ABACUS. The unstructured triangular mesh was chosen to accommodate the complex geometry of the blade. This mesh contained approximately 97,000 elements. The centrifugal forces were calculated in ABACUS by adding a rotation force field. This blade was modeled having an angular velocity equal to the angular velocity of the compressor. Each contact pad is fully constrained in the blade model. The contact pads are shown in blue in Figure 36. These boundary

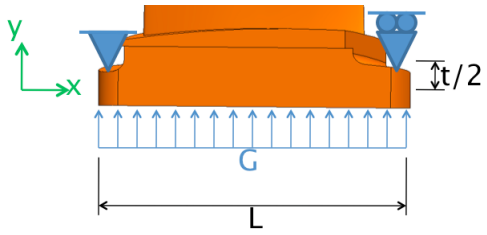

Figure 35. Drawing of the contact points of the blade to the retainer ring

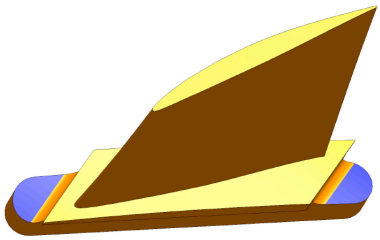

Figure 36. Drawing of the contact points of the blade to the retainer ring

Table III. Values used in Type II blade stress calculations

$F_{c\,blabe}$	4231.4	N
I_{zz}	$10,460$	mm^4
y_{top}	10.04	mm
y_{bottom}	10.76	mm
L	101.6	mm

conditions were used to simulate the retainer rings holding the blade. The Von Misses stress is shown in Figure 37. The color scale shows the maximum stress in the blade. This maximum stress comes from a stress concentration at the trailing edge of the blade.

The stress concentration occurs at the junction between the transition flange and the airfoil section. A zoomed-in view of the trailing edge is shown in Figure 38.

Comparing analytical and FEA structural analysis

This section compares the analytical results from the beam calculation to the results from the FEA. This comparison is done by looking at the safety factors of both type

Table IV. Beam theory calculations of stress and safety factors for the Type II blade

F_{dist}	$41,648$	N/m
$\sigma_{xx\,top}$	51.6	MPa
$\sigma_{xx\,bottom}$	55.3	MPa
SF_{yield}	4.99	
$SF_{fracture}$	5.6	
$\sigma_{sheer\,yield}$	$2,116$	Pa
SF_{sheer}	< 1000	

of analysis. The safety factors (SF) values from the analytical and FEA structural analysis is shown in Table V.

Table V. Comparing results from analytical and FEA structural analysis

	Analytical results	FEA results
SF_{yield}	4.99	2.43
$SF_{fracture}$	5.6	2.83

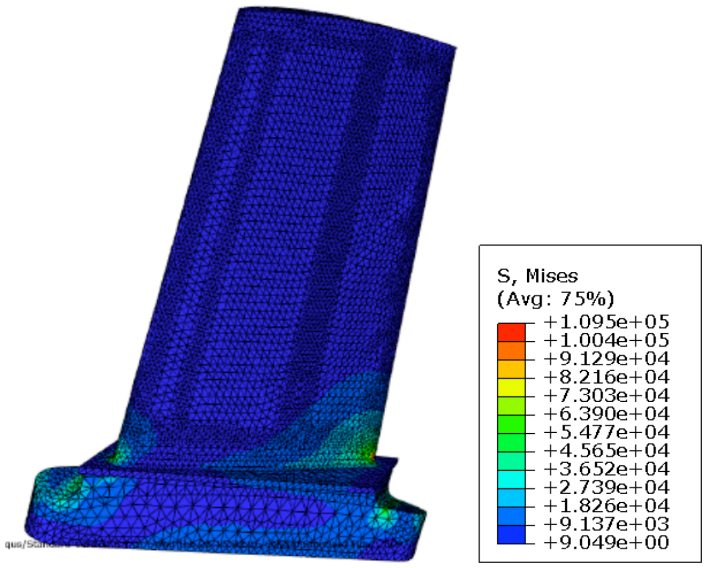

Figure 37. Full view of the blade

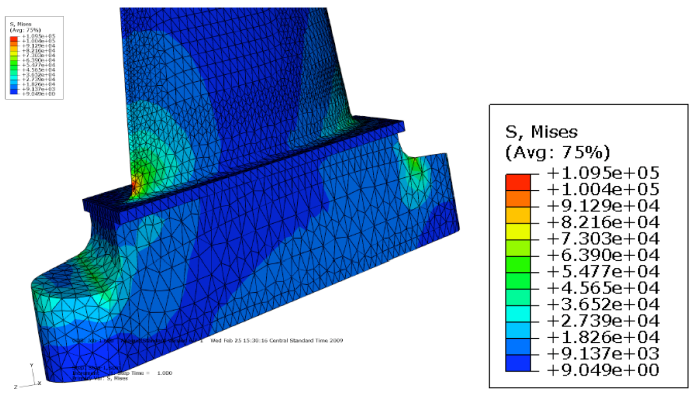

Figure 38. Junction of the trailing edge of the blade and the mount flange

Structural analyses of retainer rings

The structural analysis of the retainer rings was done analytically and using a finite element model in ABACUS.[14]

Material selection

The material chosen for the retainer ring is 410 stainless steel due to its high yield and fracture stresses, as listed in Table VI along with the density and Young's modulus.[15] This material was also chosen for its machinability which is listed as good in the machinist hand book.[17] The last column in Table VI are the units used in ABACUS, which will be explained in a later section.

Table VI. 410 stainless steel retainer rings

σ_{yield}	1,225	MPa	177,700	psi	1,225,000 kg/(mm s^2)
σ_{max}	1,525	MPa	221,200	psi	1,525,000 kg/(mm s^2)
E	200	GPa	29×10^6	psi	200×10^6 kg/(mm s^2)
ρ	7,800	kg/m^3	0.282	lb/in^3	7.8×10^{-6} kg/mm^3

Analytical structural analysis

The analytical analysis was done using the hoop stress equation, which is shown in Equation (3.3).[16]

$$\sigma_h = \frac{R\, P_{distributed}}{t} \tag{3.3}$$

Three assumptions were made in the derivation of Equation (3.3). The first

assumption is that the pressure is evenly distributed on the inside of the pipe. This assumption is not valid in the ring case; therefore, an equivalent distributed load is calculated using Equation (3.5). The equivalent distributed load was calculated using the pressure applied to the ring by each blade. This applied pressure was calculated using Equation (3.4). The calculation was also carried out using the $P_{applied}$ equal to $P_{distributed}$. Using $P_{applied}$ assumes that the ring is holding 8 times the number of blades that are actually being held. The result from this conservative calculation is as σ_h.

$$P_{applied} = \frac{F_{c\,blade}}{2\,A_{applied}} \tag{3.4}$$

where $A_{applied}$ is the contact area on each side of the blade mounting flange. The force $F_{c\,blade}$ was calculated in the blade design chapter and is the total centrifugal force coming from the blade

$$P_{distributed} = \frac{F_{c\,blade}\,N_{blades}}{2\,A_{total}} = \Big(\frac{F_{c\,blade}}{2\,A_{applied}}\Big)\frac{N_{blades}A_{applied}}{A_{total}} = P_{applied}\frac{A_{total\,applied}}{A_{total}} \tag{3.5}$$

where $A_{total\,applied}$ is equal to N_{blade} times $A_{applied}$. Equation (3.6) is derived by combining Equation (3.3) and Equation (3.5) which is a modified version of the hoop equation.

$$\bar{\sigma}_h = \frac{R\,P_{applied}}{t}\Big(\frac{A_{applied}}{A_{total}}\Big) \tag{3.6}$$

The second assumption made in the hoop stress equation is that the cross section of the pipe has a uniform thickness. This is not true in the ring case, which is shown in the cross section view of the ring in Figure 39. Therefore, to be conservative only the portion of the ring that is uniformly thick is used in the calculations. The uniform

section of the ring used in the hoop calculations is shown in blue in Figure 39.

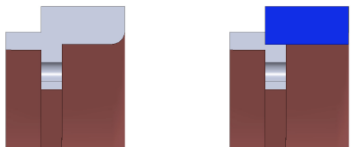

Figure 39. Cross section of the retainer ring

The third assumption is that the thickness of the ring is less that 10% of the radius. This is valid in the ring case, which has a thickness equal to 6.66% of the radius.

The values used to calculate the hoop stress are shown in Table VII. The calculation for $F_{c\,blade}$ can be found in the blade design section. The values from these calculation are shown in Table VIII.

Table VII. The values used in the hoop stress calculations

$F_{c\,blabe}$	4231.4	Number/blade
t_{ring}	0.1016	m
R_{ring}	0.1524	m
$A_{applied}$	1.05×10^{-4}	m^2
A_{total}	.02123	m^2
N_{blades}	25	*blade*

Table VIII. Results from hoop stress calculations using 410 stainless steel

$A_{total\ applied}$	2.625×10^{-3}	m^2
$P_{distributed}$	20.15	MPa
$\bar{\sigma}_{hoop}$	37.4	MPa
$\bar{SF}_{yield}$	32.8	
$\bar{SF}_{fracture}$	40	
σ_{hoop}	302.2	MPa
SF_{yield}	4.05	
$SF_{fracture}$	5.05	

FEA of retainer ring

A finite element model was developed using ABACUS. As mentioned in the blade chapter, this modeling was accomplished by importing the SolidWorks model into ABACUS.[18] This importing of a SolidWorks part file forced the length scale to be set to the default units of millimeters. ABABUS offers a scaling factor which allows the user to convert to the desired units. Using the scaling factor offered by ABACUS introduces errors into the geometry; consequently, the units of length in the FEA were kept in millimeters. These units are shown in the last column of Table VI.

The part was made into two sections by adding a partition. This partition allowed two type for meshes to be used. These sections are shown in Figure 40. The yellow section was meshed using sweep mesh; however, the pink section was meshed with a unstructured triangular mesh. The total number of elements used in this model was 97,500.

There were two types of loads applied to the retainer ring. The first load is the

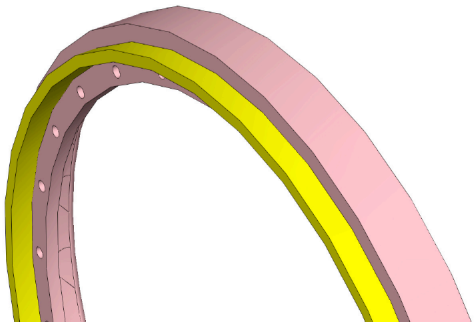

Figure 40. Drawing of the different meshing sections

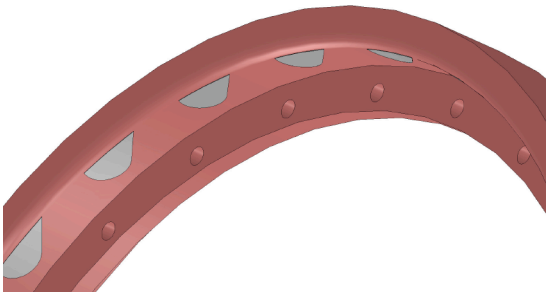

Figure 41. Drawing of the applied pressure pads

pressure load coming from the centrifugal force of the blades. The force was converted into $P_{applied}$ using Equation (3.4). This $P_{applied}$ was applied to all of the pressure pads. The pressure pads have the exact shape and location as the blade mounting flanges. These pressure pads are shown in Figure 41.

The second load is the centripetal forces acting on the retainer ring itself. This load was applied by adding a rotational load in ABACUS. The angular velocity of the ring is calculated using Equation (3.7)

$$\omega = RPM_{comp}\frac{2\pi}{60} \tag{3.7}$$

The bolt holes were fully constrained in the FEA model. This boundary condition was used to imitate to retainer ring being bolted to a rigid disk casing. This is only a conservative assumption which yields higher stresses around the bolt holes than would be present if the casing was allowed to deform.

The Von Misses stress of the retainer ring is shown in Figure 42. A zoomed in view of the bolt holes is shown in Figure 43. All the figures are shown with the color scale associated with that particular analysis.

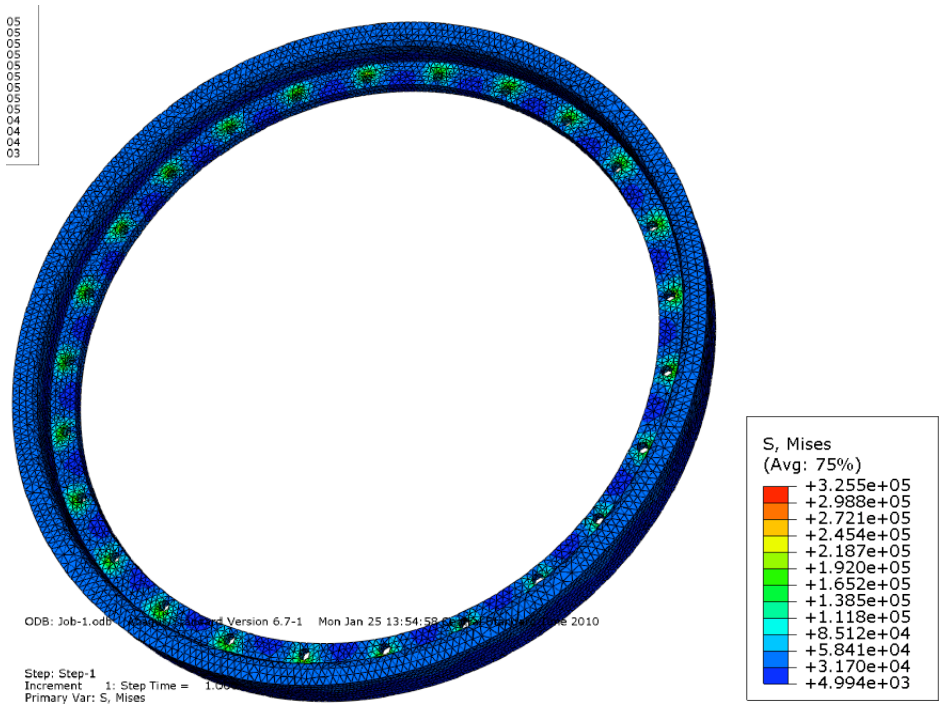

Figure 42. Von Misses stress of the retainer ring

The upper limit of the color scale shows the maximum stress in the retainer ring to be $3.255 \times 10^5 \ \frac{kg}{mm\ s^2}$. This maximum stress value is the result of the conservative assumption made in the boundary conditions, which is that the disk casing is rigid. As predicted, in Figure 42 and in a zoomed-in view in Figure 43 it is apparent that the majority of the stresses are around the bolt holes. To more precisely understand the stress concentration around the hole a more elaborate model of the bolt hole would have to be developed. However, using Saint-venant's principle it is assumed that the outer part of the ring analysis is accurate.[19]

To better analyze the outer portion of the retainer ring the outer surface of the ring was viewed separately as shown in Figure 44, and in a zoomed in view in Figure 45. The color scale was changed to view the stresses on this portion of the retainer ring. The maximum stress is shown to be $5.478 \times 10^4 \ \frac{kg}{mm\ s^2}$, and the average stress

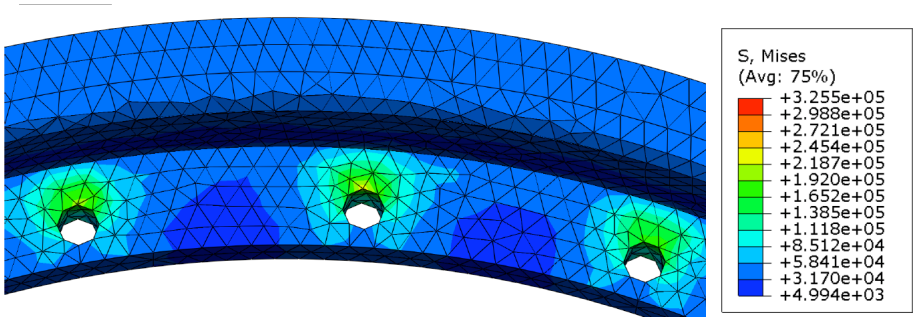

Figure 43. Von Misses stress of the zoomed-in view of the retainer ring

is approximately $3.5 \times 10^4 \ \frac{kg}{mm\ s^2}$.

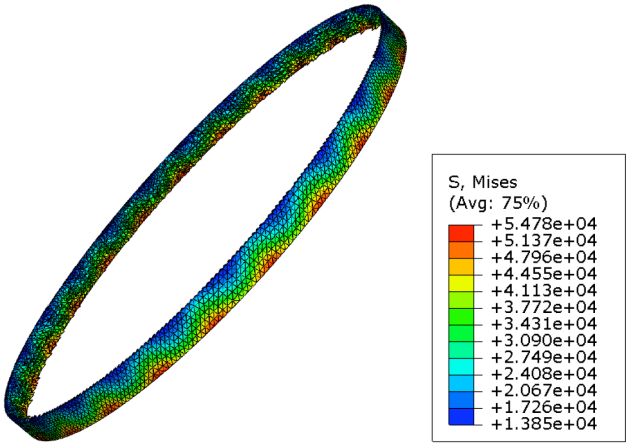

Figure 44. Von Misses stress of outer portion of retainer ring

Comparison of analytical and FEA results

This section compares the analytical results from the hoop calculation to the results from the FEA. This comparison is done by looking at the safety factors of the maximum and average stress values for both type of analysis. The safety factors (SF) values from the analytical and FEA structural analysis is shown in Table IX.

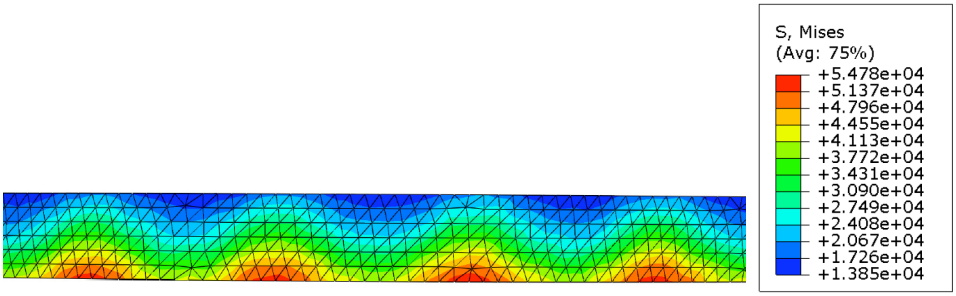

Figure 45. Zoomed-in view of Von Misses stress of the outer portion of retainer ring

Table IX. Comparison of results from hoop stress calculations and FEA

Analytical results		FEA results	
$\bar{SF}_{yield}$	32.8	$SF_{yield\,average}$	22.3
$\bar{SF}_{fracture}$	40.0	$SF_{fracture\,average}$	27.8
SF_{yield}	4.05	$SF_{yield\,max}$	3.79
$SF_{fracture}$	5.05	$SF_{fracture\,max}$	4.72

Summary

An analytical and finite element structural analysis was done on the Type II blades, which gave a minimum yield safety factor of 2.4. An analytical and finite element structural analysis was done on the retainer ring of the disk, which gave a minimum yield safety factor of 4.05. Both the retainer ring and the blade calculations provide conservative estimations of the safety factors; they were considered acceptable.

CHAPTER IV

EXPERIMENTAL SETUP

This chapter describes the design of the equipment used in the experimental phase of this work. Thus, this chapter is broken into six sections: (1) the instrumentation used in the experiments, (2) a description of the high pressure air supply system that was used with the scaled down pulse modulator, (3) the designing and manufacturing of the scaled down pulse modulator, (4) the design and construction of the wind tunnel around the scaled down pulse modulator, (5) the construction of all of the test-blades, and (6) the implementation of two hot-wire traversing systems.

Instrumentation

This section discusses the measurement devices used throughout the experiments.

Hot-wire anemometer

Due to the high frequencies of the pulsed air, a hot-wire anemometer was used to measure jet velocities. The hot-wire was calibrated with respect to the velocity ranges that were being measured.

Pressure measurements

A Barocell pressure transducer in conjunction with a scanivalve was used to measure the pressure distribution on the airfoil sections. The scanivalve allowed a single pressure transducer to be used to measure several pressure ports. The accuracy of the Barocell pressure transducer is $\pm$ 6 Pa.

High pressure air supply

The high pressure supply system was needed to provide the pulse modulator with the required mass flow rate. This was accomplished by having the air supply from the building routed to a compressed air tank. The pressure in the tank was regulated during an experiment. The tank pressure was regulated using the pressure gage on the tank itself. This configuration prevented the flow from choking in the pressure regulator.

Scaled down pulse modulator

A scaled down version of the pulse modulator was designed and built as a proof of concept. The scaled down pulse modulator design allowed several features of the design to be better understood.

One of these features is the role that frequency has on the flow characteristics. These measurements were made possible by swapping the stationary and rotating portions of the pulse modulator. The scaled down pulse modulator had a stationary blade and a rotating inner section. The jet frequency was controlled by changing the RPM of the inner portion of the pulse modulator. This design allowed the frequency response of the system to be studied.

The scaled down pulse modulator was also used to study the flow parameters with different types of internal geometry and exit slots. This was made possible by having an interchangeable test section that consisted of the internal plenum and jet slot.

Another feature that is now better understood are the tolerances that can be maintained on the gap between the stationary and rotating portions of the pulse modulator. This gap directly affects the amount of flow that leaks into the internal

plenum while the slots are not aligned. This leakage directly affects the amplitude of the pulses exiting the jet slot.

Overview of scaled down pulse modulator

The scaled down pulse modulator was designed to preserve the physics of the internal flow. It consists of the same parts as the full size pulse modulator design, as shown in Figure 46 and Figure 47.

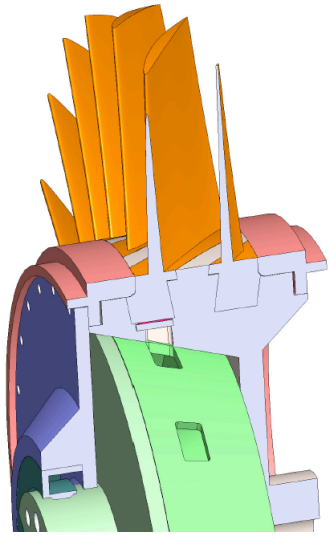

Figure 46. Cut view of the full size pulse modulator

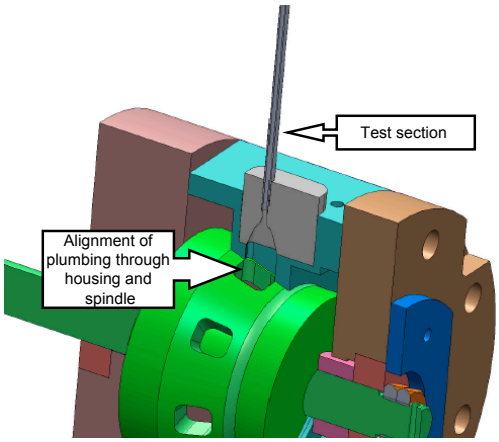

Figure 47. View of plumbing through the scaled down pulse modulator

The high pressure supply air is injected through the top housing end-plate and fills the internal chamber of the pulse modulator. This configuration is exactly the same as the full size pulse modulator. The spindle and casing of the scaled down pulse modulator has a tapered intersection for fine adjustments of the gap between the two sections. This is the same as the full size pulse modulator. The inner portion,

the spindle, has a series of holes around its circumference. While the spindle rotates the holes periodically align with the channel in the casing. This periodic alignment of the holes provides the pulsing air to the blade section. The spindle was spun with a drill press, or for the higher speed a CNC mill was used. An exploded view of the scaled down pulse modulator in shown in Figure 48.

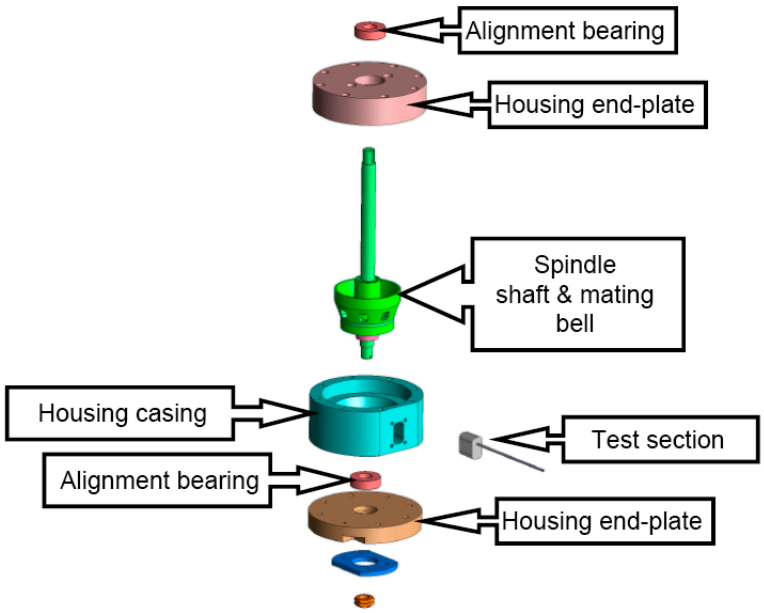

Figure 48. Exploded view of scaled down pulse modulator

The benefit of the this pulse modulator is that it allows a large portion of the internal plumbing and jet slot to be easily manufactured and replaced. This replaceable part of the scaled down pulse modulator is called the test-section, and consists of two parts: (1) the test-blade, which is described in detail in the test-blade section of this chapter, and (2) the insert that models the internal plumbing of the disk casing. There were two types of inserts used in these experiments.

a Casing insert 1

The first insert was used in the frequency response experiment. The insert had exactly the same length as the full size channel. However, this channel is an insert that was constructed using the RP machine. By using RP, different shaped contraction sections could be tested.

b Casing insert 2

This insert is used in the small wind tunnel and is used with the Type II test-blade. The second channel had the same contraction shape as the first insert and was also made using the RP machine; however, this insert was designed to allow the test-blade to rotate inside of the insert. This was accomplished by using an o-ring to seal the insert and the aluminum brace that led to the test-blade. This insert forms a channel that is 25 mm longer than the channel in the full size compressor. This was unavoidable due to the geometry of the small wind tunnel. A cut view of the casing insert 2 is shown in Figure 49.

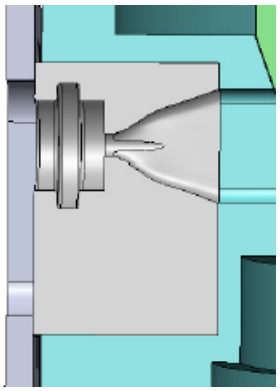

Figure 49. Cut view of insert used in wind tunnel testing

Parameters used to scale down the pulse modulator

This section describes five parameters considered when scaling down the pulse modulator, which are listed below:

- The maximum f_{jet} is equal to the operating f_{jet} of the compressor.
- ΔP: pressure difference between the high pressure supply air and the surface of the SSB. This value is one of the parameters that will be studied; therefore, it is controllable in both the full and scaled down pulse modulator .
- Exit area and geometry of the exit jet slot, on the surface of the blade, will be studied using the scaled down pulse modulator . The study will aid in the final design of the exit slot on the full size compressor.
- Internal volume (υ) of the plenum, which runs through the disk and SSB, is approximately the same size as in the full size pulse modulator design. This study will be used to determine the final shaped used in the full size pulse modulator.
- Due to the no-contact design of the pulse modulator, the SFM was not preserved in the scaling process.

The values used in the scaled down pulse modulator are listed in Table X.

Manufacturing of the scaled down pulse modulator

The casing was machined on the CNC mill. The bell portion of the spindle was partially machined on the CNC mill, and then pressed onto the shaft. The assembled spindle was then machined to the final dimensions using a CNC lathe, which allowed the bell portion to be perfectly concentric with the shaft. The casing and the spindle

were honed together on the manual mill, which insured that the two surfaces were the exact same shape.

A shim was machined to provide a gap, between the rotating and stationary portions, of .0635 mm (.0025 inches). However, due to the slight misalignments of the assembled scaled down pulse modulator, the spindle and the casing are .0889 mm (0.00035 inches) out of concentricity. This slight misalignment varies the gap between .0546 mm (.00215 inch) and.0724mm (.00285 inch). This was measured by inserting an indicator in the pulse modulator through the plumbing of the insert. This small variation in the gap is noticeable in the jet velocity versus time data from the frequency response and jet characteristics experiments. Therefore, the jet velocity is very sensitive to the gap size. The finished scaled down pulse modulator is shown in Figure 50.

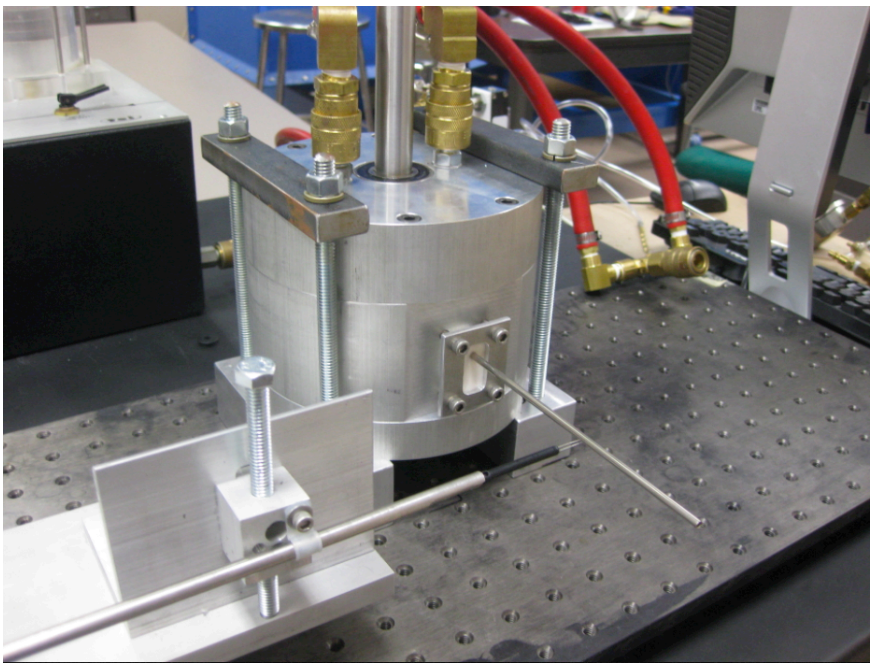

Figure 50. Photograph of the finished scaled down pulse modulator

Table X. Values used in scaled down pulse modulator

F^+	0.5
DC	0.5
η_{shape}	3.15
RPM_{system} [rev/min]	6000
f_{comp} [Hz]	100
f_{jet} [Hz]	800
C [m]	0.076
$\Re$	0.8
n_{slot}	8
C_x [m/s]	29
sw [mm]	3.81
$R_{blade\,tip}$ [m]	0.254
$R_{blade\,hob}$ [m]	0.1524
R_{pm} [in]	0.0402
θ_{τ_n} [deg]	22.5
θ_{τ} [deg]	17.07
θ_{ψ} [deg]	5.43

Wind tunnel

A small wind tunnel was designed and built around the scaled down pulse modulator, to study the effects of the pulsing air on the upper surface pressure distribution of an airfoil section. The small wind tunnel was needed for two reasons:(1) to allow the wind tunnel to be modular enough to be put in the CNC mill and, (2) to allow the size and volume of the internal plenum of the test blade to closely match that of the full size pulse modulator. Consequently, the drive system was required to be near the test section. It was decided that a wind tunnel needed to be specifically designed to fit these two needs.

The following sections describe the design of the wind tunnel, which consists of several subassemblies. A list of these subassemblies and a brief description of the role they play in the small wind tunnel system is given below. A photograph of the finished wind tunnel is shown in Figure 51.

- Diffuser: smoothly transitions from the test-section to the fan inlet.
- Fan: responsible for providing the necessary mass flow rate through the wind tunnel.
- Mounting plate: allows the subassemblies to be align and also aids in making the wind tunnel modular.
- Scaled down pulse modulator: provides the test-blade with pulsing air.
- Inner walls: prevents the inlet boundary layer from entering the test-section.
- Blade cylinder: holds the test-blades (or cascade) and allows the blades to be moved as a single unit.

- Angle-of-attack mechanism: responsible for moving the blade cylinder to different orientations.

- Inlet and flow conditioner: provides clean air to the test-section.

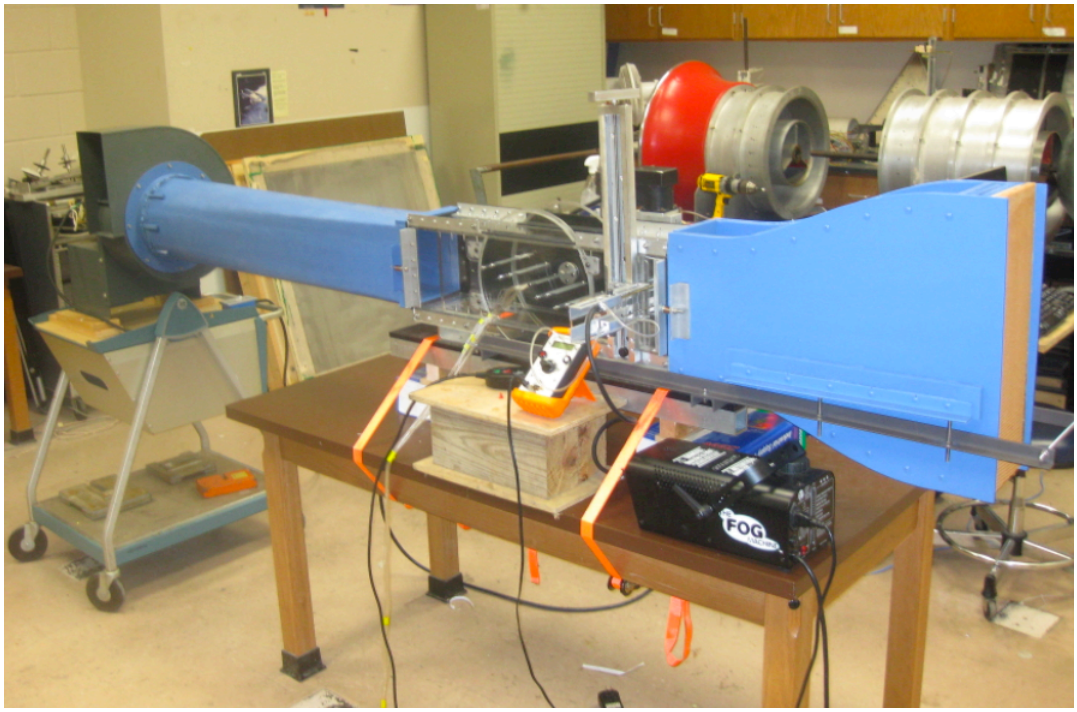

Figure 51. The fully assembled wind tunnel

Diffuser

The diffuser is a fiber glass cylinder that smoothly transitions from the rectangular test-section, 177.6 by 155.6 mm, to the round fan inlet, 244.5 mm diameter. This diffuser has an area ratio (A_{ratio}) of 1.70, and an equivalent diffuser angle (Φ) of 1.42 deg, which was calculated using Equation (4.1).[20] It is suggested that the area ratio be no greater than 6:1 and the diffusion angle be no greater then 7 degrees.[20] The

length of the diffuser was determined by the size of the CNC mill, and drove both the area ratio and the diffuser angle to small values. The diffuser is shown in Figure 52.

$$\Phi = \tan^{-1}\left(\frac{1 - \frac{1}{\sqrt{A_{ratio}}}}{\frac{L_{deff}}{R_{fan}}}\right) \tag{4.1}$$

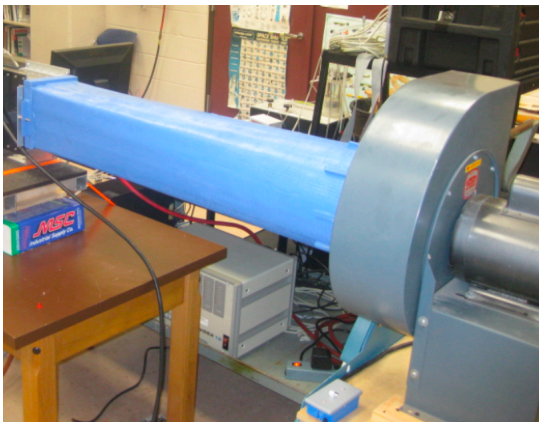

Figure 52. Photograph of diffuser and fan

Fan

The fan, provided by the Flight Research Lab (FRL), has a 1.12 KW [1.5 hp] electric motor and spins a centrifugal compressor. This fan has a volumetric flow rate of approximately 1,290 L/s [2,230 cfm] and provides the wind tunnel with a velocity range between 32 to 38 m/s [72 to 85 mph]. The mass flow rate of the fan was not adjustable; therefore, the velocity varied as the blockage of the wind tunnel varied. This is the reason the velocity is given as a range.

Mounting plate

The mounting plat is a modified aluminum breadboard, which conveniently provided a 1" grid of tapped bolt holes. The breadboard was mounted to two, 2"x2" square aluminum bars, which provided rigidity to the platform. A small frame, which supports the inlet, was bolted to the top of the breadboard. A photograph of the mounting plate is shown in Figure 53. The scaled down pulse modulator was mounted to a raised platform in the center of the mounting plate. This platform locates and aligns the scaled down pulse modulator with the mounting plate, as shown in Figure 53. The mount, which attaches the test-section to the mounting plate was made easily adjustable. This adjustment allows the test-section to be aligned with the scaled down pulse modulator plumbing.

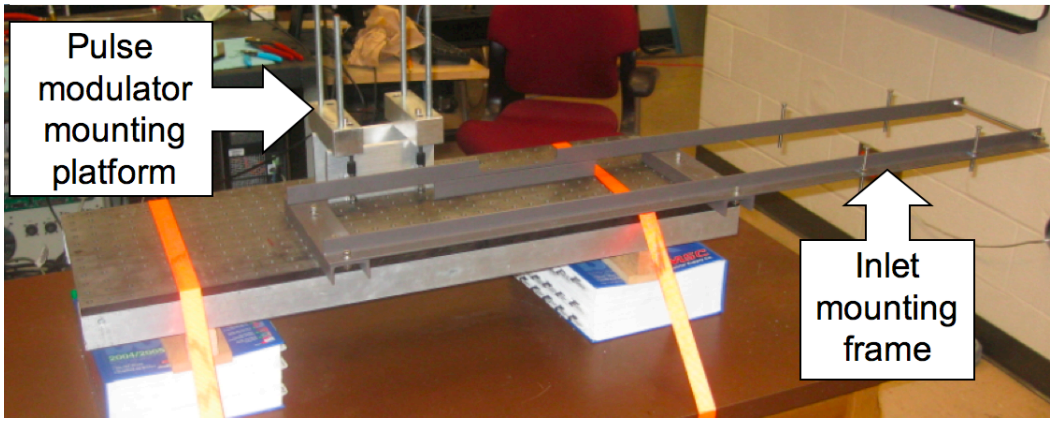

Figure 53. Fully assembled mounting plate

Scaled down pulse modulator

The pulse modulator was spun using a drill press that was mounted to the mounting plate. However, for larger F^+ Numbers the entire test-section could be mounted in

the CNC mill, and spun using the mill spindle. The drill press drive system is shown in Figure 54.

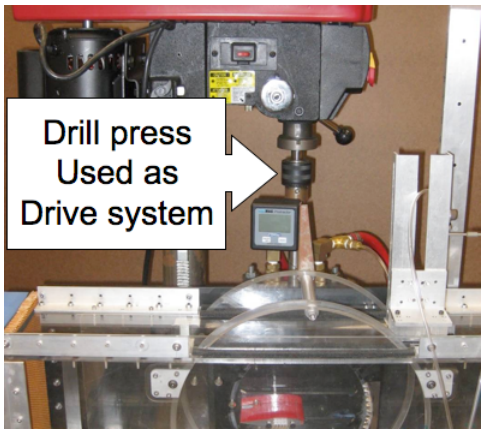

Figure 54. Drill press drive system

Inner walls of wind tunnel

The wind tunnel has an inner and outer set of walls, which provide two benefits. The first benefit is that the boundary layer, which is formed in the inlet, is absorbed in the gap between the inner and outer. The second benefit is that there is a small pressure difference between the test section and the gap between the walls; therefore, there is less leakage around the blade-cylinder.

Blade-cylinder

A single blade or a cascade of blades can be mounted in the blade-cylinder, which is shown in Figure 55. The blade-cylinder allows the angle-of-attack of the blade (or cascade) to be adjusted as a single unit. The blade-cylinder has an aluminum bracket on the pulse modulator side which is supported by a ball bearing on the outer wall.

The bracket is also connected to the angle-of-attack arm, as shown in Figure 56. The angle-of-attack arm is used to rotate the blade-cylinder. The front side of the blade-cylinder is supported with four ball bearing around the perimeter of the cylinder, as shown in Figure 55. This support configuration allows the view of the blade surface to be unobstructed, which allows for flow visualization to be done on the surface of the blades.

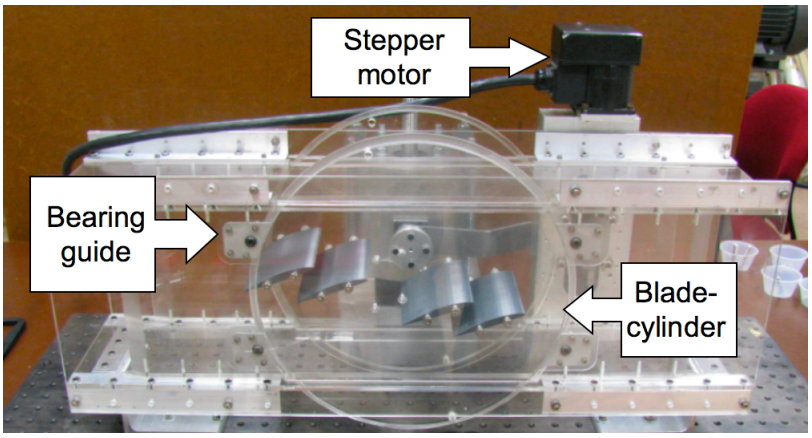

Figure 55. Photograph of the blade-cylinder

The blade-cylinder is designed to allow a primitive cascade setup to be tested. This cascade setup may be used to better understand the effect that other blades have on the flow; however, currently there have been no cascade tests done using this wind tunnel.

Instrumentation

A Barocell pressure transducer was used to measure the pressure in the wind tunnel. A scanivalue was used to switch to all the pressure ports. There were eleven pressure ports on the top surface of the airfoil, and a total pressure measurement from a pitot

tube located upstream of the blades. All of the pressures were relative to the static pressure of the pitot tube. This allowed Cp to be easily calculated by dividing the pressure port measurements with that obtained from the pitot tube.

$$C_p = \frac{P_{airfoil\,port} - P_{static}}{P_{total} - P_{static}} = \frac{\Delta P}{q_\infty} \tag{4.2}$$

The pitot tube was mounted to the top of the tunnel, and the hight of the pitot tube was adjustable. This same mounting system could be mounted on the ball-screw machines on the side of the wind tunnel. This mount was used to hold the smoke outlet pipe, which allowed the height and spanwise location of the smoke outlet pipe to be adjusted.

Angle-of-attack control

The angle-of-attack of the blade or cascade is adjustable and is controlled with a stepper motor. The stepper motor drives a ball-screw assembly that rotates the blade cylinder, as shown in Figure 56 and Figure 57. The angle-of-attack was calibrated using a digital protractor. The protractor was aligned with the chord line using an alignment tool, which has a bottom surface that is exactly the same shape as the upper surface of the airfoil and a top surface that is aligned with the chord line. The alignment tool was made using the RP machine.

Inlet and flow conditioner

The shape of the inlet is described by a fifth-order polynomial, which is shown in Equation (4.3). The polynomial is in inches and x ranges from 4" to 20". The polynomial coefficients are given in Table XI. The inlet is 609.6 mm long and 155.58 mm wide and has a flat 101.6 mm section before and after the polynomial contraction.

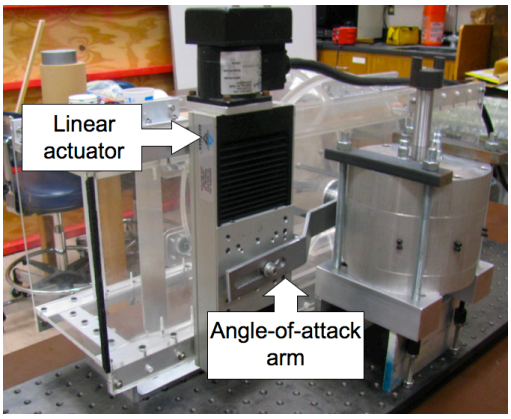

Figure 56. Photograph of angle-of-attack controller

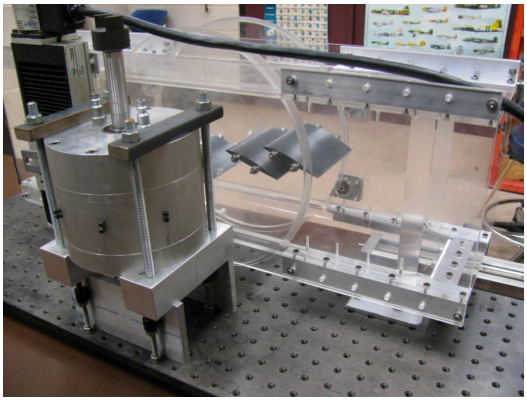

Figure 57. Scaled down pulse modulator mounting platform

There is a honeycomb flow conditioner on the front of the inlet, which is 19 mm thick.

$$Y = a_5x^5 + a_4x^4 + a_3x^3 + a_2x^2 + a_1x + a_0 \tag{4.3}$$

The inlet is aligned and mounted to the wind tunnel used to brackets on each side of the of the inlet; however, the weight of the inlet is supported by a frame that is mounted directly to the mounting plate. This frame has four jack-bolts that are used to align the inlet of the with tunnel.

Table XI. Coefficients used in inlet design

Coefficients			
a_0	3.91	a_3	6.05×10^{-3}
a_1	-0.148	a_4	-3.66×10^{-4}
a_2	-7.03×10^{-3}	a_5	6.10×10^{-6}

Smoke assembly

An assembly was mounted to the side of the wind tunnel that allowed smoke to be injected into the test section of the tunnel, which is shown in Figure 58. The assembly allowed for fine adjustments of the location of the smoke steam.

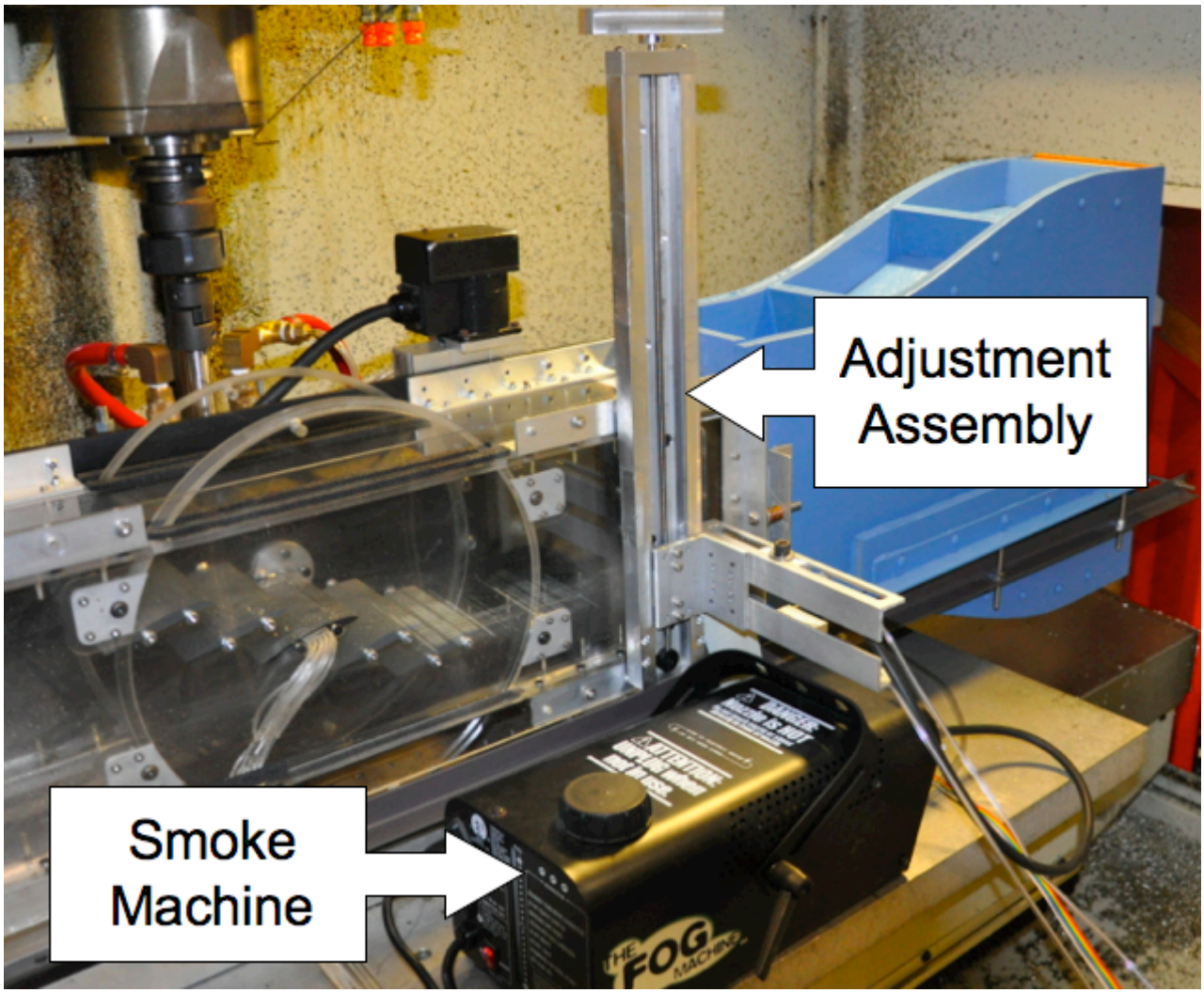

Figure 58. Smoke system in wind tunnel

Test-blades

There were two types of test-blades made for the scaled down pulse modulator and wind tunnel. The second type of test-blade had three different internal pipes and a set of wing fences that were used in the experiments. All of the test-blades and their configurations are explained in this section.

Type I test-blades

The Type I test-blade was used in the frequency response experiment. This test-blade was a 3.35 mm diameter pipe that had five, 2.03 X .33 mm [0.08 X .013 inches], slots along the span, as shown in Figure 59. This test-blade has the same plenum volume and length as the full scale SSB. The square shaped slots allowed the hot-wire probe to be completely submerged in the jet velocity. The Type I test-blade and the insert used in the scaled down pulse modulator is shown in Figure 60.

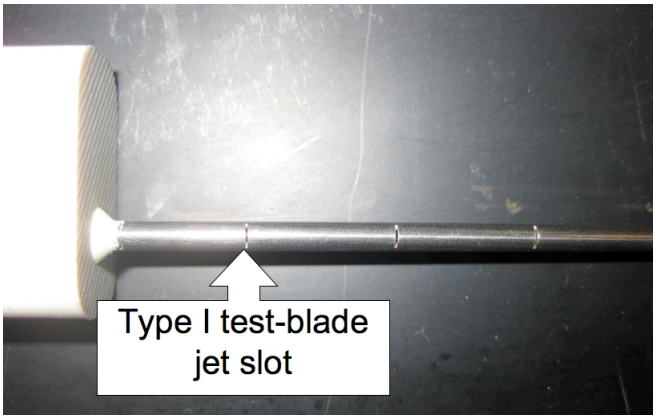

Figure 59. Jet slot in Type I test-blade

Figure 60. Type I test blade

Type II test-blades

The Type II test-blade was used in the jet slot flow characteristics experiment, which studied the effect that the pulse modulated blowing has on the pressure distribution of an airfoil section. The test-blade contained of an internal plenum that has the same volume and length as the full scale SSB. The outer shape of the test blade is a NACA 0015 airfoil with a chord of 76.2 mm [3 in]. The jet velocity exiting the slot was measured using a hot-wire probe. The Type II blade is shown in Figure 61.

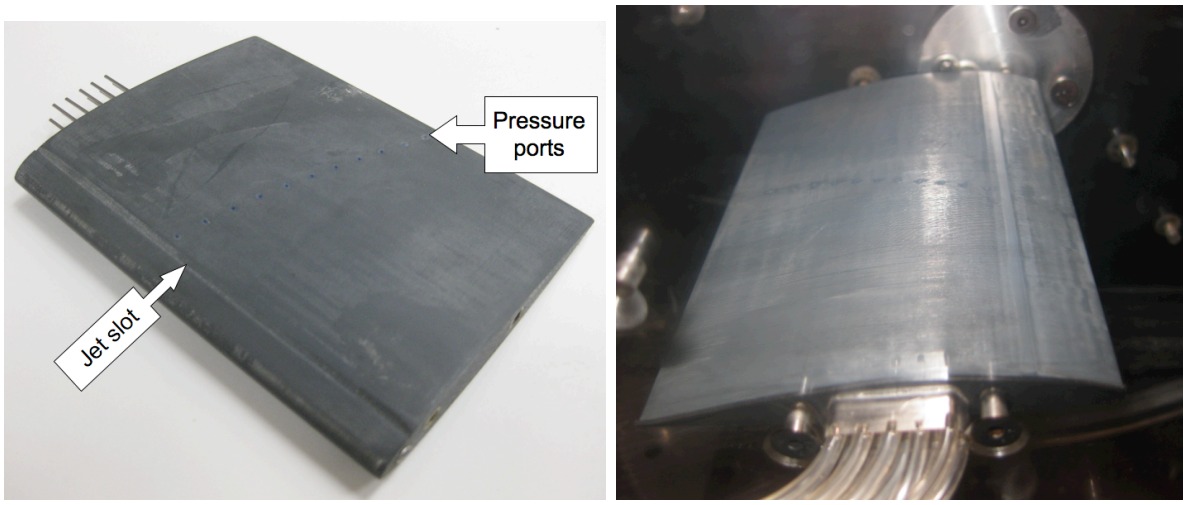

Figure 61. Type II test-blade

The test-blade had eleven pressure ports along the chord, which were put on a diagonal across the top surface of the blade, as shown in Figure 61. These pressure ports were used to measure the pressure distribution on the top surface of the test blade. The plumbing consisted of stainless steel hypodermic tubes and Teflon plastic tubes. The plastic tubes were plumbed to the upper surface of the blade. The plastic tubes were then trimmed flush with the top surface of the test-blade. The plumbing is shown in Figure 62 and in Figure 63. The plumbing chamber was then filled with epoxy and sanded to mach the bottom surface of the test-blade.

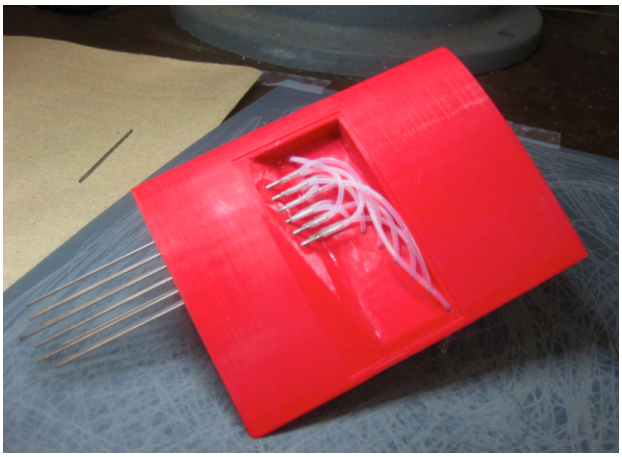

Figure 62. Type II test-blade pressure ports plumbing

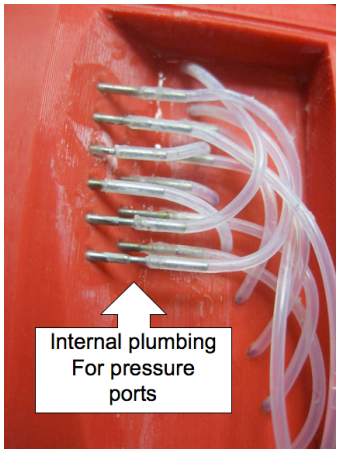

Figure 63. Zoomed in view of plumbing used in the pressure ports

Pipes used in the Type II test-blade

There were three pipes made for the Type II test-blade, each having the same diameter and volume as the SSB. The pipes consisted of a full-span pipe (FSP) and two part-spans (PSP1 & PSP2). Each of the part-span pipes have twenty, 0.66 mm diameter holes that are located in the center of the blade. The holes were spaced 1.04 mm

apart. The full-span pipe had 93, 0.66 mm diameter holes distributed evenly across the full span of the blade. The holes were again spaced 1.04 mm apart.

An error in the drilling process led to a misalignment in the hole pattern on the first part-span pipe, as shown in Figure 64. A second part-span pipe was made after the drilling process was improved. The PSP1 was used in this experiment to study the sensitivity of the jet slot velocity to irregularity in the pipe shapes. The FSP was drilled using the same drilling process as the second part-span pipe, and is shown in Figure 65.

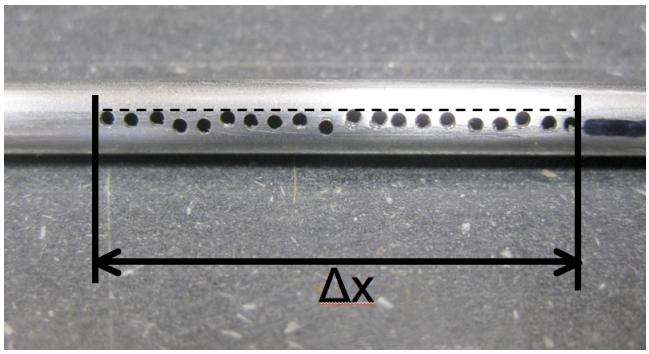

Figure 64. The zoomed in view of the PSP1

The Type II test-blade has a slot that runs along the span, which is connected to the pipe that supplies the pulsing air, as shown in Figure 66. The slot was sanded to be 0.127 mm wide. This gave the FSP jet slot an area of 12.9 mm^2 and the PSPs an area of 2.58 mm^2.

When using the part-span pipe, the Type II test-blade was equipped with wing fences. The wing fences served two purposes:(1) it isolated the portion of the blade that was being stimulated by the pulse modulated blowing, and (2) it was used to eliminate some flow irregularities in the small wind tunnel. The wing fences were

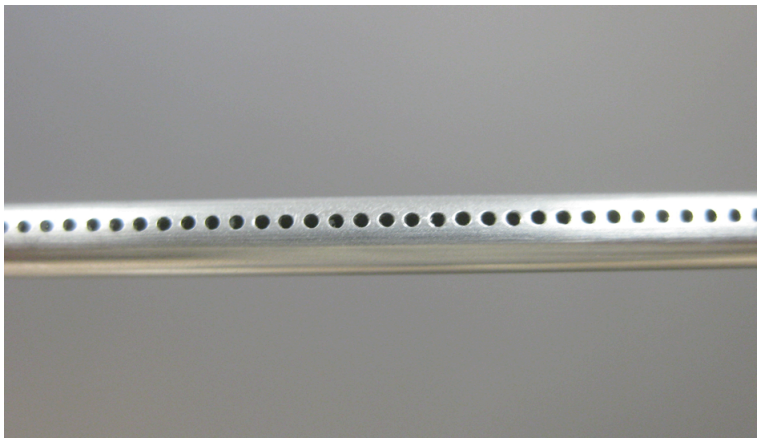

Figure 65. Photograph of the FSP using the revised drilling process

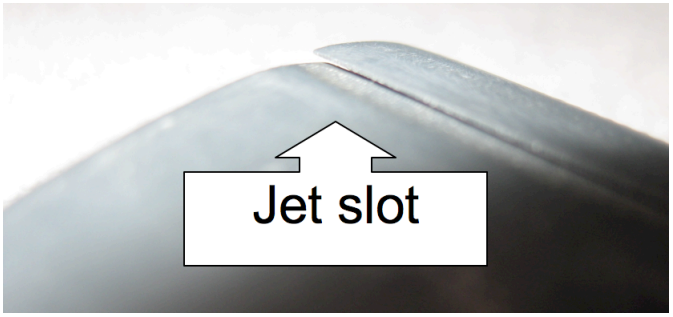

Figure 66. View of the slot in the Type II test-blade

added to each side of the pressure ports. The Type II blade, with wing fences, installed in the wind tunnel is shown in Figure 67.

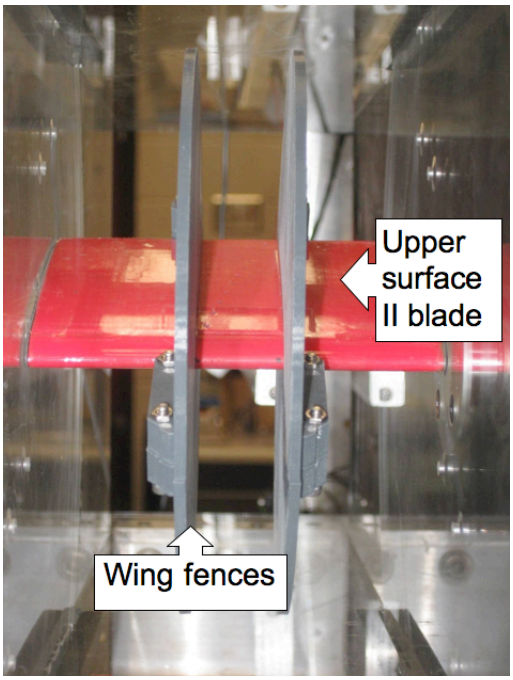

Figure 67. The wing fences mounted on the Type II test-blade

Hot-wire traversing systems

There were two traversing systems used to move the hot-wire. A single-axis system was used in the frequency response experiment, and a 3-axis traversing system was used in the jet slot characterization experiment.

Single-axis traversing system

This single-axis traversing system consisted of a stepper motor that drove a linear actuator. The system was controlled using an Aerotech UNIDEX 12 system that was connected to the main computer via a serial port; therefore, the traversing system was commanded by a Labview code. This allowed the movement to be coordinated with the hot-wire measurement. The stepper motor was equipped with a angular encoder, which ensured that there were negligible location errors. The linear actuator was equipped with a home switch, thus allowing the system to retain the relative location after a power-cycle. The one-axis traversing system is shown in Figure 68.

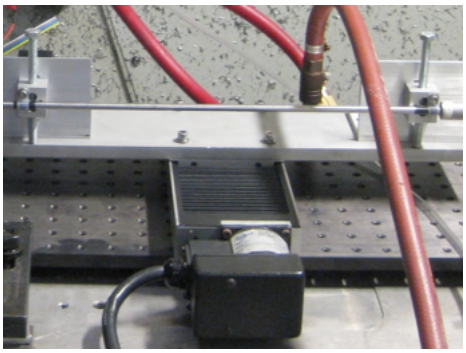

Figure 68. Single-axis traversing system

3-axis traversing system

The 3-axis traversing system was built in-house. All of the axes were controlled with a ball-screw assembly; however, only two of the axes were driven with a stepper motor. The third axis was hand operated. The two automated axes were equipped with limit switches that were also used to home each axis. An Aero-probe controller was used to operate the stepper motors. A driver for this controller was written in Labview. Thus the traversing system was controlled via a Labview code. The 3-axis traversing system is shown in Figure 69. This system has no position feedback; therefore, it needed to be homed periodically to prevent location errors from accumulating.

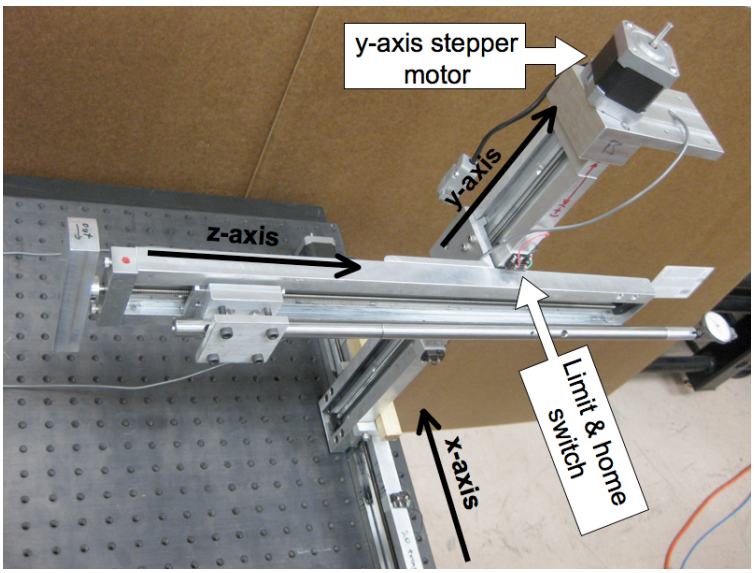

Figure 69. Three axis traversing system

Summary

This chapter described the systems used in all of the experiments. This chapter consisted of five sections: (1) the instrumentation used in the experiments, (2) a description of the high pressure air supply system that was used with the scaled down pulse modulator, (3) the designing and manufacturing of the scaled down pulse modulator, (4) the design and construction of the wind tunnel around the scaled down pulse modulator, (5) the construction of all of the test-blades, and (6) the implementation of two hot-wire traversing systems.

CHAPTER V

EXPERIMENTAL RESULTS

This chapter describes each four experiments that were done using the scaled down pulse modulator. Each test was conducted to study specific traits of the system. The first experiment was used to study the frequency response of the exit jet slot. The second experiment was used to study the flow characteristic of the exit jet. The third experiment was used to study the baseline stall characteristics of a NACA 0015 airfoil in the wind tunnel. The fourth experiment evaluated the effect the stall suppression system has on the stall characteristics of a NACA 0015 airfoil.

Exit jet frequency response experiment

A test was done to investigate the effect that the jet frequency has on the amplitude of the pulses; however, due to the rounded jet slots the actual C_μ values were inaccurate. The rounded jet slot is shown in Figure 70. This frequency response test was primarily done to investigate the change in C_μ with frequency, thus the inaccuracy in the C_μ values where deemed acceptable.

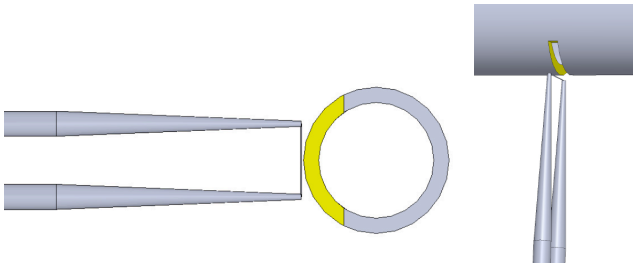

Figure 70. The hot-wire probe aligned with the jet slot in Type I test-blade

Experiment configuration

This test allowed the F^+ Number and the pressure difference of the scaled down pulse modulator to be varied while the jet velocity was being measured. This was done by using an aluminum breadboard as a base plate, which allowed the experiment to be modular enough to put into the CNC mill, as show in Figure 71. The CNC mill was used to spin the pulse modulator to allow for a wide range of RPMs to be tested.

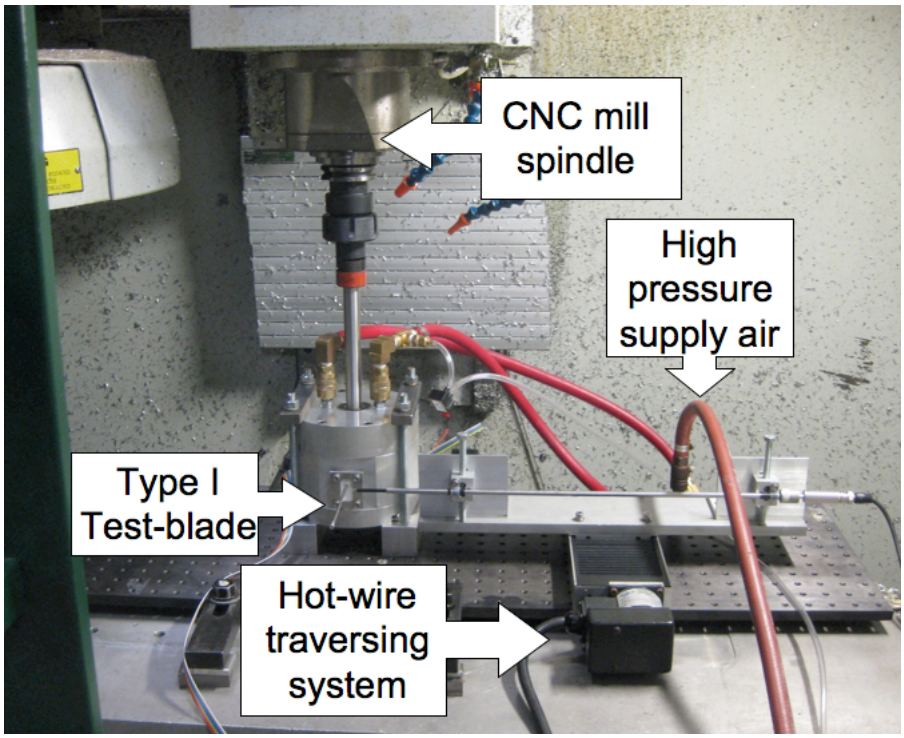

Figure 71. Photograph of experimental configuration

The layout of the data acquisition system, pressure system, and traverse control system is shown in Figure 72. The main computer operated the data acquisition and the traversing system using a Labview code. This configuration made it possible to coordinate the movements and the measurements of the hot-wire.

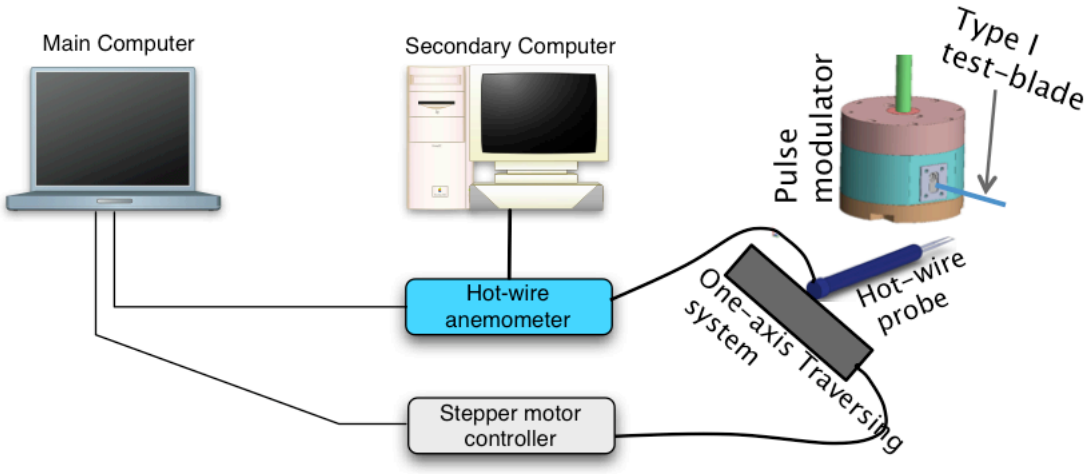

Figure 72. Layout of the exit jet frequency response experimental

a Test-blade

The Type I test-blade was used in this experiment. The Type I test-blade consisted of a pipe and an RP insert. The pipe had an outer diameter of 3.35 mm, an inner diameter of 3.0 mm, and a length of 114 mm, which was the estimated size of the actual compressor blade.

b Traversing system

The one-axis linear traversing system was used in this experiment. This traversing system allowed the hot-wire to be incrementally moved over the jet slot of the Type I test-blade. This incremental move allowed the position of the velocity measurement to be precise.

c Instrumentation

Due to the high frequencies, the hot-wire anenometer was used to measure the jet velocity. The hot-wire was aligned with the slots of the Type I test-blade, which allowed the hot-wire to be completely submerged in the flow exiting the jet slot.

Test matrix

The experiment consisted of three supply pressures and twelve RPM values, as listed in the test matrix shown in Table XII. The sweep of hot-wire measurements were centered over each hole in the Type I test-blade. The hot-wire probe was moved in increments of 0.031 mm and velocity measurements were taken at each location. The sample rate was varied with the jet frequency to obtain a sample frequency that is thirty times the jet frequency ($f_{sample} = 30 f_{jet}$).

Table XII. Full-span exit jet test matrix

Test-blade	Type I test-blade
Supply pressure [psi]	1.19, 2.57, 3.81
RPM [rev/min]	500 to 6000 ΔRPM of 500
f_{jet} [Hz]	66.6 to 800 Δf_{jet} of 66.6
Spanwise location [mm]	25 location sweeping across each hole Δx of 0.031 mm

Results

The C_μ and F^+ Numbers were calculated in this section using the values for the full size compressor. These values are listed in Table XIII.

Table XIII. Values used in the calculation of C_μ and F^+ for frequency response test

U_∞ [m/s]	$\sqrt{(\omega R)^2 + C_a^2}$
ω [rad/s]	367
C_a [m/s]	29
h [mm]	1.52
C_{blade} [mm]	76.2
$\Re$	0.85
ρ_{jet} [kg/m^3]	1.225(add equation rho=f(Vjet))
ρ_∞ [kg/m^3]	1.225

Result of C_μ calculations

The standard deviation of the jet velocity was calculated for the different spanwise locations, jet frequencies, and supply pressures. The maximum values for each spanwise location were used to calculate C_μ for each supply pressure and jet frequency. This variation of C_μ with frequency and pressure is shown in Figure 73.

The C_μ versus span for an F^+ Number of 0.47, at the tip of the blade, is shown in Figure 74: However, the remaining plots corresponding to all of the F^+ Numbers values are shown in the Appendix. This plot of C_μ versus radius shows higher amplitudes at the smaller radii; however, this was ignored due to the error in the measurement of the velocity. The important thing in this experiment is that the C_μ values do not change much due to frequency variation. This is especially true for the high pressure case, where C_μ is approximately flat across the range of F^+ Numbers, as shown in Figure 73.

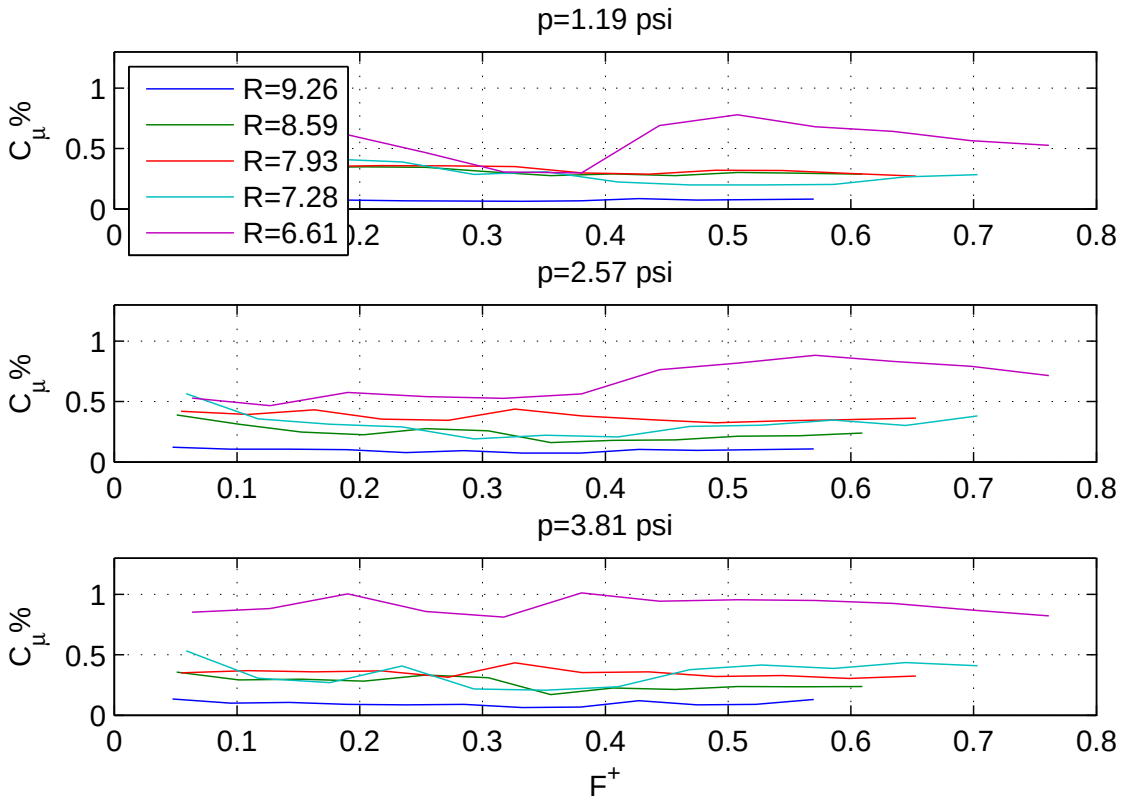

Figure 73. C_μ vs. F^+

Summary

This experiment was done primarily to investigate the trend of C_μ as jet frequency was changed. This trend gives an insight on the effect of frequency on C_μ. It can be seen from the C_μ versus F^+ Number plot that frequency has little effect on the values of C_μ. At this stage in testing the pulse modulator design was found to be acceptable; however, experiments detailing the jet velocity distribution will be done to better understand the flow characteristics of the jet velocity.

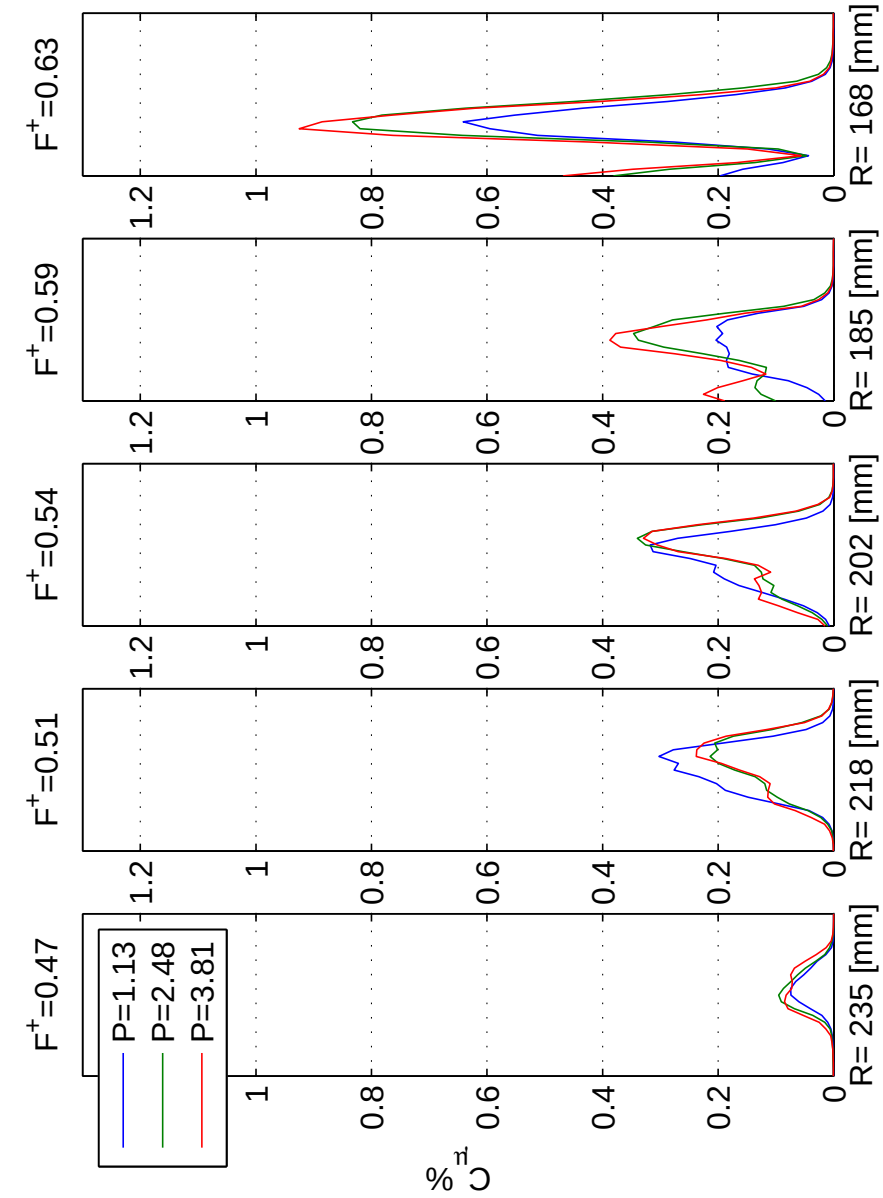

Figure 74. C_μ vs. radius of 5 holes

Exit jet characteristics experiment

This experiment studies the characteristics of the jet slot at different supply pressures and with three jet slot configurations. This experiment was conducted to understand the range of C_μ that can be produced with the scaled down pulse modulator. Different internal plenums were used to study the effect of the jet exit area C_μ. This study will aid in the development of the full size pulse modulator and the design of the jet slot on the compressor blades.

Experimental configuration

This experiment was done in the small wind tunnel, which allowed the pressure distribution experiment to be done without changing setup. This configuration insured that the test-blade did not change in anyway between the two experiments. This was accomplished by removing the diffuser and motor from the wind tunnel, and then inserting a hot-wire probe, which was mounted to the 3-axis traversing system, through the back of the wind tunnel. the layout of the systems used in the experiment is shown in Figure 75.

a Test-blade

The Type II test-blade was used in this experiment; however, there were three different internal pipes used. There was one full-span pipe (FSP) and two part-span pipes (PSP1 & PSP2) used in the Type II test-blade.

b Instrumentation

The hot-wire anenometer was used to measure the jet velocity exiting the slot, allowing high frequency measurements to be made. The sampling frequency of the hot-wire

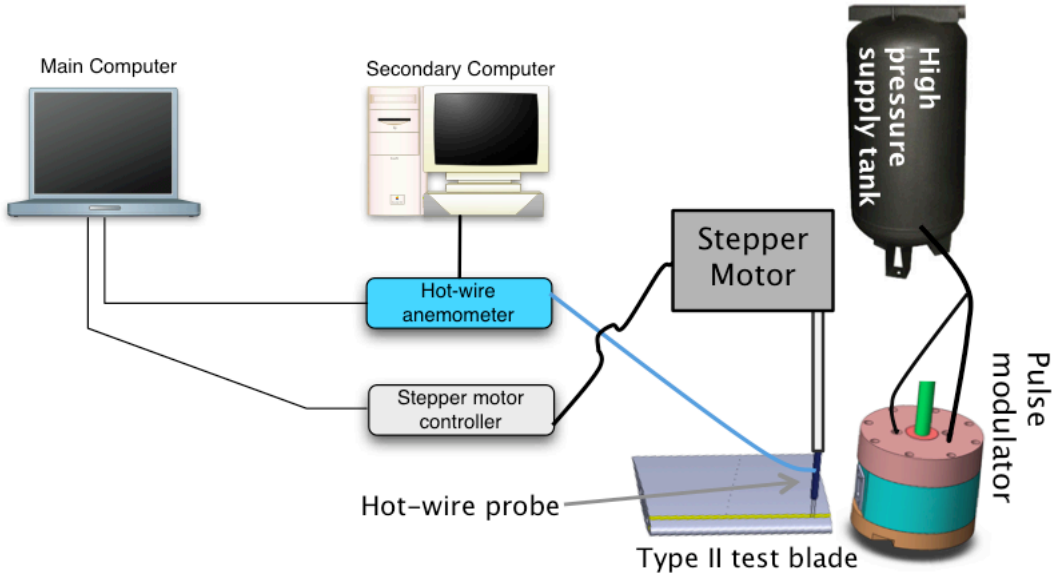

Figure 75. Layout of the exit jet characteristics experiment

was set to be thirty times the jet frequency ($f_{sample} = 30 f_{jet}$).

c Traversing system

The three-axis traversing system was used in this experiment, allowing several measurements to be taken along the span and chord of the blade. The traversing system was aligned with the test-blade with a test indicator, as shown in Figure 76. This was accomplished by adjusting the position of the traversing system until it was aligned with the test-blade. The hot-wire is shown in alignment in Figure 77.

The height of the hot-wire probe above the top surface of the test-blade was adjusted by hand; therefore, the repeatability in height was ± 0.125 mm. The measured jet velocity proved to be sensitive to this height adjustment. The height of the pipe had to be reset for each test-blade configuration; consequently, the velocity values relative to each test-blade configuration are accurate but may have different magni-

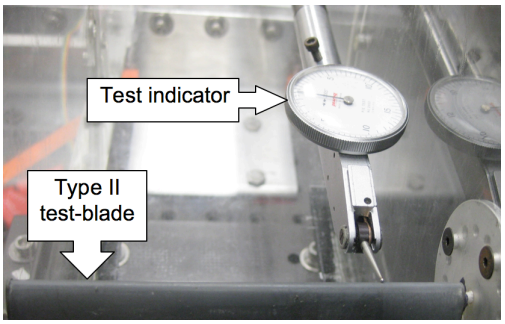

Figure 76. The alignment being done using test indicator

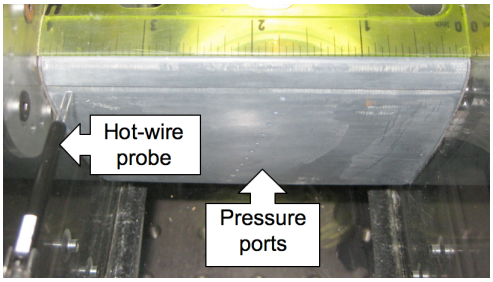

Figure 77. Aligned hot-wire probe

tudes due to the height difference. A photograph of the hot-wire probe in position for a test is shown in Figure 78 and Figure 79.

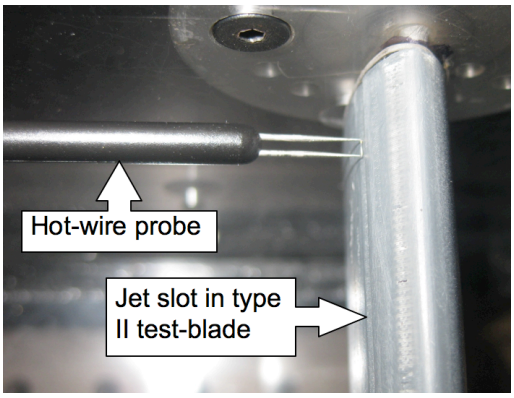

Figure 78. Top view of hot-wire probe in position for test

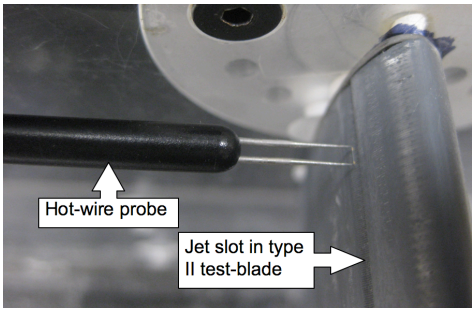

Figure 79. Side view of hot-wire probe in position for test

The traversing system was homed after every sweep in span, ensuring that any location errors would not accumulate throughout the experiment. The chordwise axis was homed after a full sweep in the chord was completed. The location of the homing switch did not change between the full and part-span blades. This was achieved by

adding a spacer in-front of the spanwise homing switch while conducting the part-span pipe test.

Test matrix

All three blade configurations (FSP, PSP1, and PSP2) were tested under the same conditions. The hot-wire probe was moved in increments of 1.01 mm in the spanwise direction, and increments of 0.127 mm in the chordwise direction. The FSP and PSP test matrix is listed in Table XIV and Table XV respectively.

Table XIV. Full-span exit jet test matrix

Test-blade	Full-span Type II test-blade
Supply pressure [psi]	25
Chordwise locations [mm]	0.00 to 0.76 mm Δy of 0.127 mm
Spanwise location [mm]	5.05 to 85.3 mm Δx of 1.01 mm

Table XV. Part-span exit jet test matrix

Test-blade	Part-span Type II test-blades
Supply pressure [psi]	5, 10, 15, 20, 25
Chordwise locations [mm]	0.00 to 0.76 mm Δy of 0.127 mm
Spanwise location [mm]	38.7 to 56.0 mm Δx of 1.01 mm

Results

The C_μ and F^+ Numbers were calculated in this section using the values from the small wind tunnel. These values are listed in Table XVI.

Table XVI. Values used in the calculation of C_μ and F^+ for jet characteristics test

U_∞ [m/s]	36
h [mm]	1.52
C_{blade} [mm]	76.2
$\Re$	0.85
ρ_{jet} [kg/m^3]	1.225
ρ_∞ [kg/m^3]	1.225

a C_μ calculations

The standard deviation of the jet velocity was calculated for all of the spanwise and chordwise locations. The maximum chordwise values were used to calculate the spanwise C_μ distribution. These calculations were done for all of the test cases given in Table XIV and Table XV. The plots of C_μ for the FSP, PSP1,and PSP2 are shown in Figure 80, Figure 81, and Figure 82 respectively. Table XVII shows the average of C_μ for all the supply pressures and test-blade configurations.

The values of C_μ at each supply pressure and test-blade configuration were averaged and plotted, as shown in Figure 83.

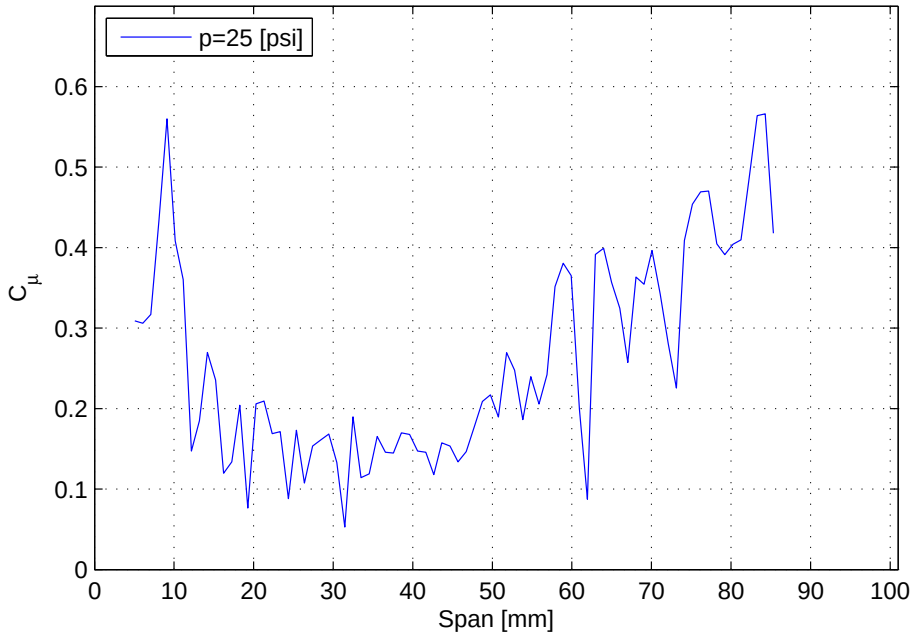

Figure 80. FSP: C_μ of jet slot vs. span

Table XVII. Averaged C_μ% values for different supply pressures and test-blade configurations

Supply pressure [psi]	5	10	15	20	25
PSP1	0.34	0.54	0.73	1.16	1.55
PSP2	0.39	0.55	0.75	1.19	1.03
FSP					0.24

b Mean velocity results

The mean jet velocity was calculated for all the spanwise and chordwise locations. This was done for all five supply pressures and three test-blade configurations. The

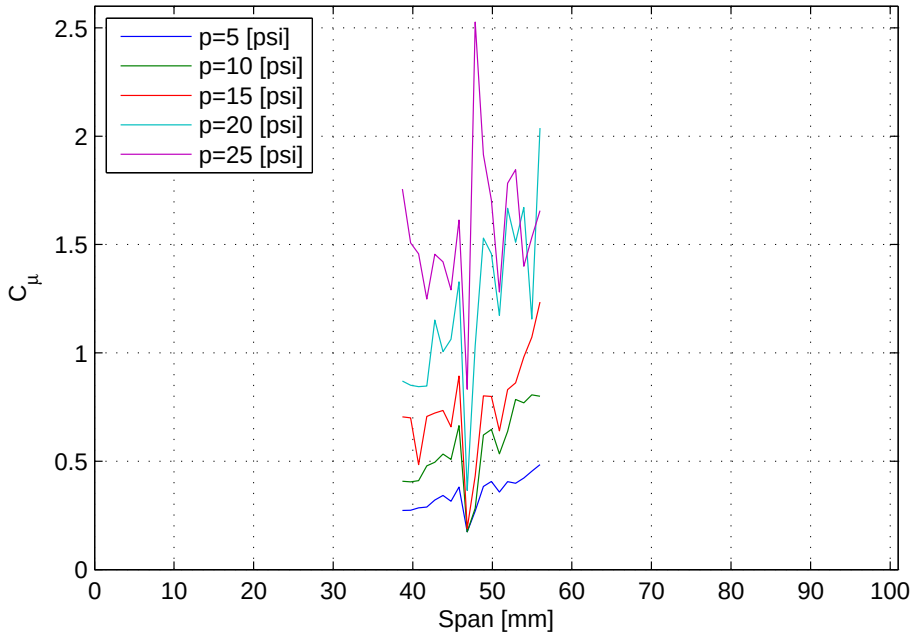

Figure 81. PSP1: C_μ of jet slot vs. span

maximum chordwise values for each test blade were plotted and are shown in Figure 84, Figure 85, and Figure 86. Table XVII shown the average of C_μ for all the supply pressures and test-blade configurations.

Summary

The average C_μ values obtained for the part-span test-blades matched very closely, except for one data point; however, the profiles were dramatically different. The one averaged data point (PSP2 @ 25 psi) that does not match the trend of C_μ values is most-likely due to a change in the direction of the jet velocity. This change in direction would change the velocity component being measure by the hot-wire, but would not yield a smaller magnitude of the velocity. This is only a theory and would need to be tested further to be verified. The dramatic differences in the part-span

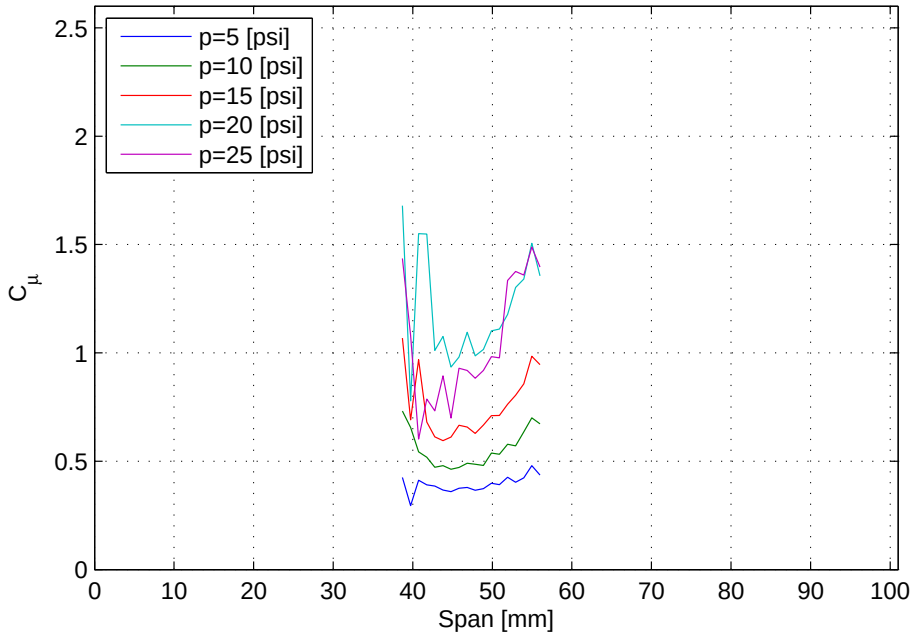

Figure 82. PSP2: C_μ of jet slot vs. span

jet velocity profiles are due to the irregularities in the PSP1 test pipe, which are discussed in the experimental setup chapter.

The mean velocity values are used for two reasons. (1) to provide boundary conditions for CFD analysis, and (2) to calculate the density of the air exiting the jet slot.

The PSP1 test-blade was chosen for the flow control experiment. The PSP1 test-blade was chosen for two reasons: (1) because it yielded the highest C_μ values, and (2) the part-span test-blade will need to be used in the wind tunnel, which will be explained in detail in the baseline pressure distribution experiment.

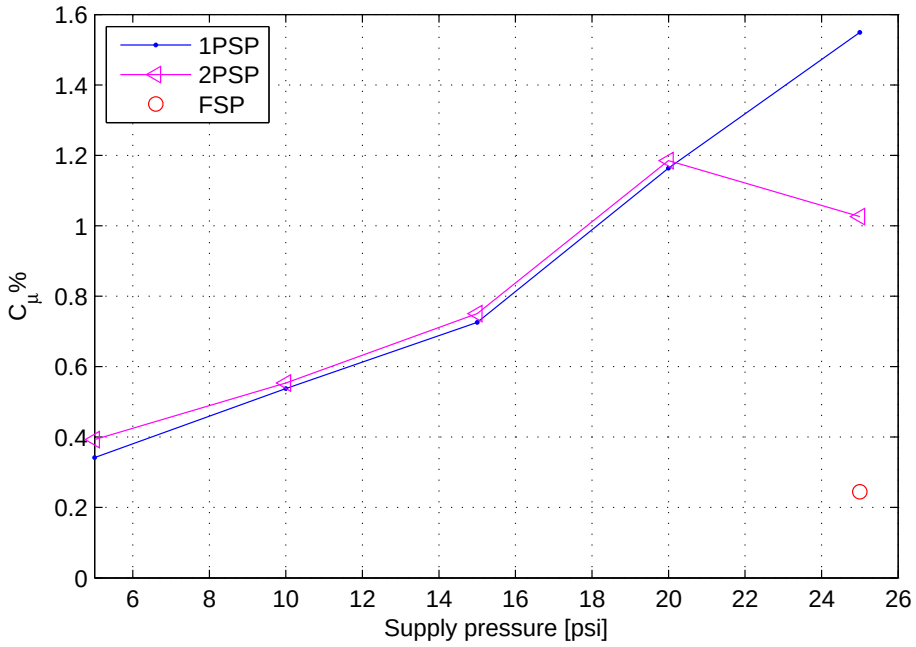

Figure 83. C_μ vs. supply pressure for three test-blade configurations

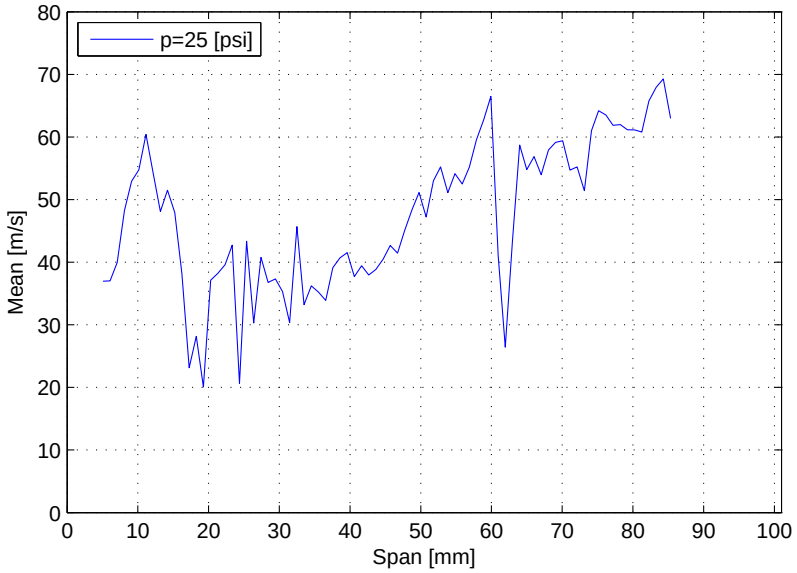

Figure 84. FSP: Mean velocity of jet slot vs. span

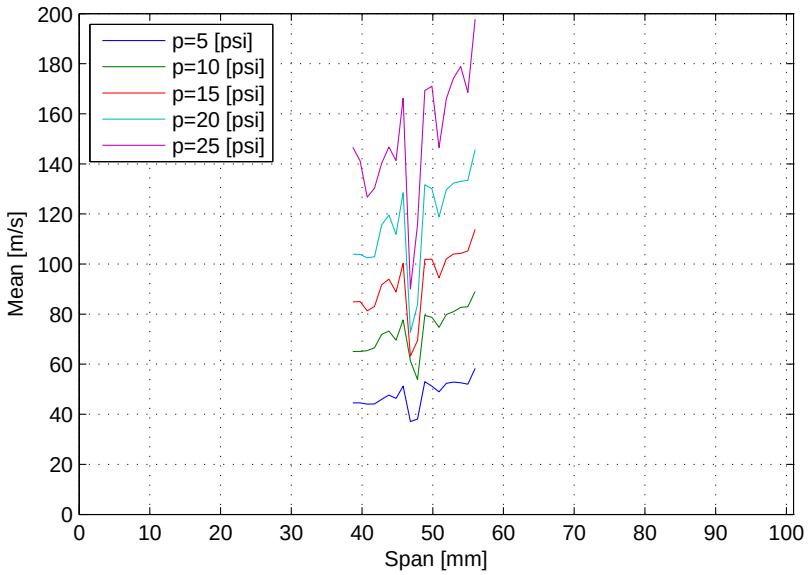

Figure 85. PSP1: Mean velocity of jet slot vs. span

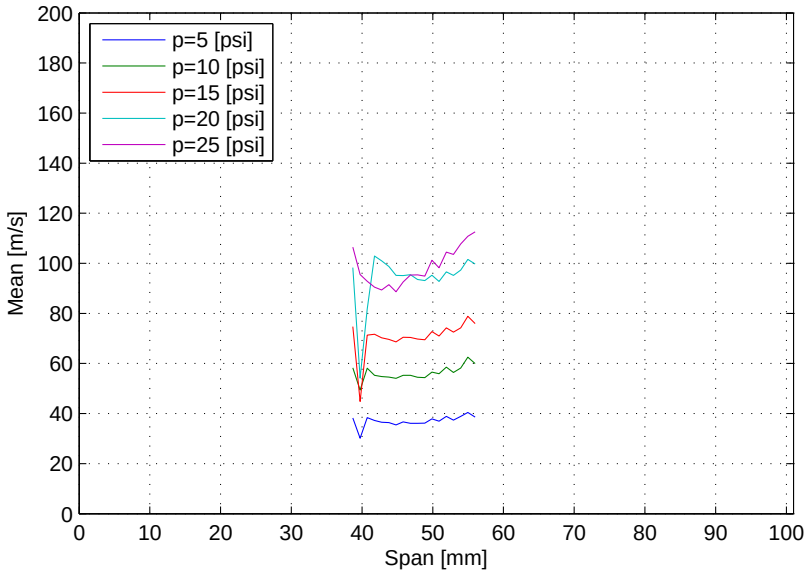

Figure 86. PSP2: Mean velocity of jet slot vs. span

Baseline pressure distribution experiment

An experiment was done on the NACA 0015 blade section to ensure that the measured pressure distributions match trends of other experiment data. This experiment investigates the flow quality of the new wind tunnel; therefore, allowing for modifications to be done to correct any irregularities.

Experimental configuration

This experiment was done using the small wind tunnel which was developed around the scaled down pulse modulator. The main computer operates the data acquisition (DAQ) and angle-of-attack systems, which allowed the two systems to be coordinated. The layout of the experimental systems is shown in Figure 87.

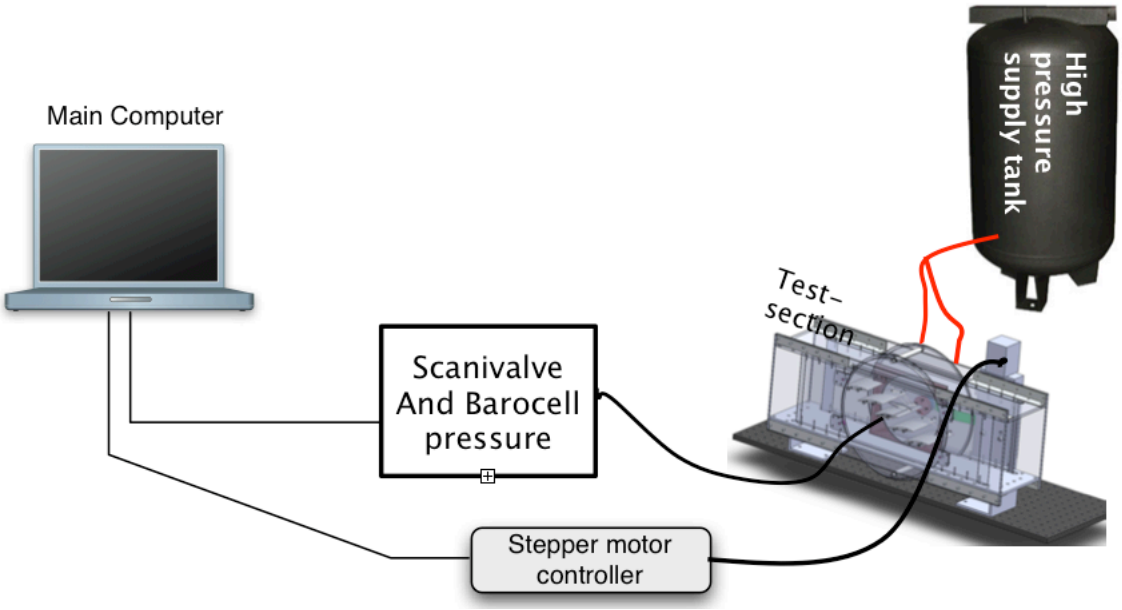

Figure 87. Layout of DAQ and angle-of-attack system

a Test-blade

There were two configurations of the Type II test-blade used in this experiment. The first configuration is the full-span Type II blade which used the FSP. The second configuration is a part-span Type II test-blade. As described in the experimental setup chapter, the part-span test-blade was equipped with wing fences on each side of the pressure ports to isolate that portion of the blade from non-uniformities in the tunnel.

b Instrumentation

The pressure distributions was measured using a Barocell pressure transducer in conjunction with a scanivalve. A detailed description of this system was given in the experimental setup chapter.

Test matrix

The pressure distribution were measured at several positive and corresponding negative angles-of-attack, as listed in Table XVIII. The values from the negative angles-of-attack were assumed to be similar to the pressure distribution at the bottom surface of the blade for the positive angles-of-attack. This assumption could be made due to the symmetry of the test-section and the test-blade. However, the pressure ports only covered a portion of the chord, thus only a reduced normal coefficient could be calculated. The reduced normal coefficient was then converted to a reduced lift coefficient ($C_{l_{red}}$) by multiplying it by $cos(\alpha)$.

Table XVIII. Test matrix for baseline pressure distribution experiment

Test-blade	FSP and 1PSP Type II test-blade
Angle-of-attack [deg]	-18 to -9, -6, -3, 0, 3, 6, 9 to 18

Results

The calculated $C_{l_{red}}$ versus angle-of-attack was plotted for both the FSP and the PSP1 test-blade, and is shown in Figure 88. The PSP1 $C_{l_{red}}$ curve shows a stall clearly beginning at 12 degrees angle-of-attack. The FSP test-blade shows a slight decrease in $C_{l_{red}}$ between 14 and 16 deg angle-of-attack; however, this is not a clear break that would indicate that the blade is stalling.

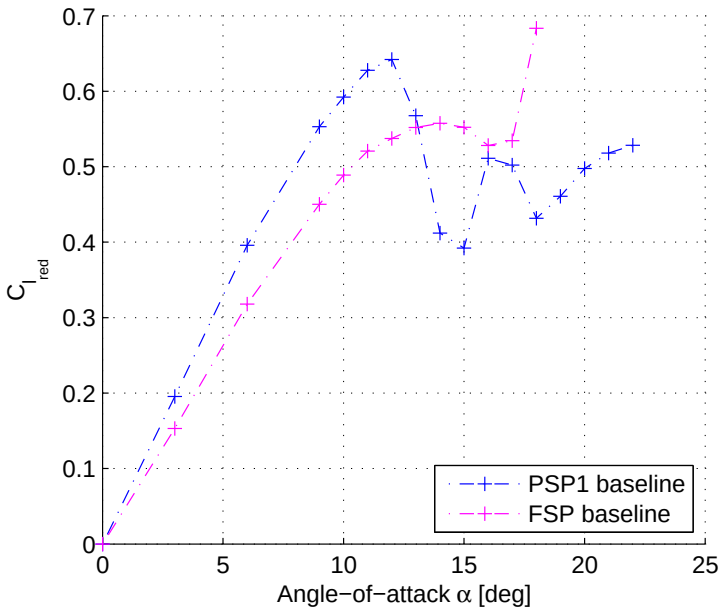

Figure 88. Part and full span $C_{l_{red}}$ vs. α

a Pressure distribution results

These trends in the $C_{l_{red}}$ plot can be further investigated by studying the pressure distributions at the critical angles-of-attack. The pressure distributions for these critical angles-of-attack are shown below; however, the pressure distributions for all the angles-of-attack can be found in the Appendix.

The stall of the PSP1 test-blade, beginning at 12 degrees angle-of-attack, can also be seen in the pressure distributions, as shown in Figure 89 through Figure 94. The stall is detected by the flattening of the pressure distribution at the trailing edge of the test-blade. This flat portion of the pressure distribution propagates forward, toward the leading edge of the blade, as the angle-of-attacks increases to 15 degrees. This phenomena can also be seen in several studies.[21]

The FSP test-blade shows some flattening at 15 and 16 deg; however, this is minimal and does not give a clear indication of stall. This trend does not match any documented experiments found; therefore, the behavior was attributed to flow irregularities in the wind tunnel. These irregularities most-likely come from the inlet of the wind tunnel. One of the problems with the inlet is the surface streamlines of a rectangular contraction intersect the side walls, which leads to secondary flows in the corners with attendant lower velocities and the possibility of separation.[20] This hypothesis will need to be investigated further to prove that this is causing the abnormal trends in the pressure distribution of the full-span test-blade.

Summary

The FSP test-blade pressure distribution provided evidence that there are flow irregularities in the wind tunnel. Further studies will need to be conducted to elimnate the irregularities in the flow. The cause for the irregularities is most-likely due to the

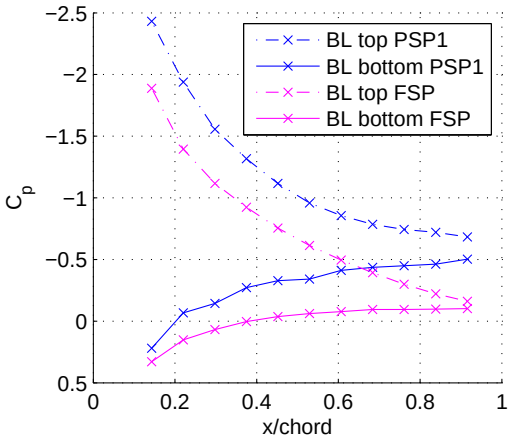

Figure 89. Cp vs. x/c @ α=12 [deg]

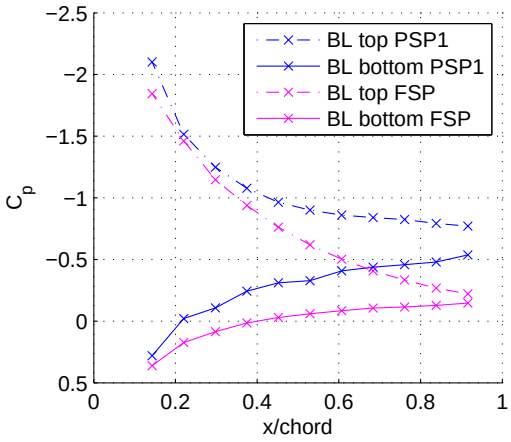

Figure 90. Cp vs. x/c @ α=13 [deg]

square contraction cone.

Adding wing fences to the test-blade appeared to isolate the instrumented portion of the blade from irregularities in the flow. As a result , the PSP1 test-blade had clear stall characteristics that matched the trends found in other investigation.[22] The clear stall characteristics and the validation of the pressure distribution allowed this PSP1 test-blade to be used in the flow control experiment.

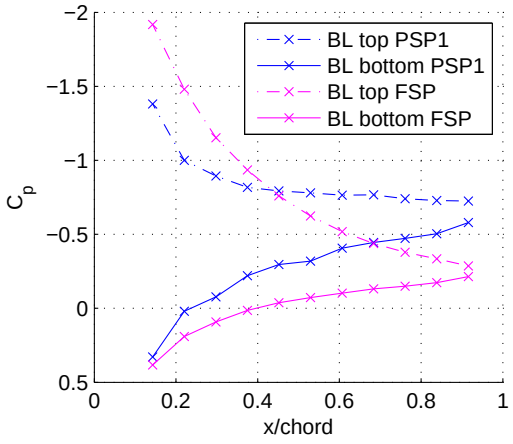

Figure 91. Cp vs. x/c @ α=14 [deg]

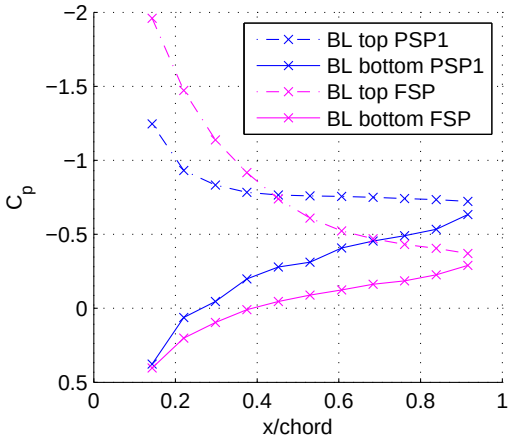

Figure 92. Cp vs. x/c @ α=15 [deg]

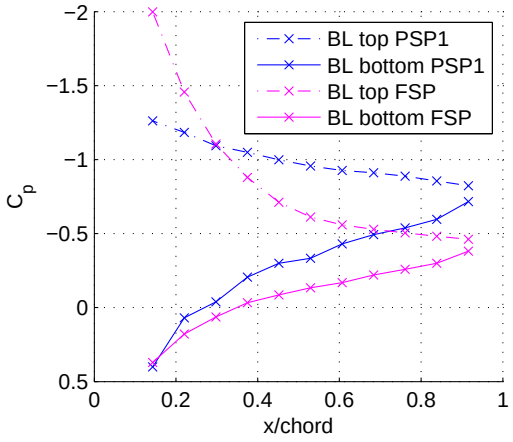

Figure 93. Cp vs. x/c @ α=16 [deg]

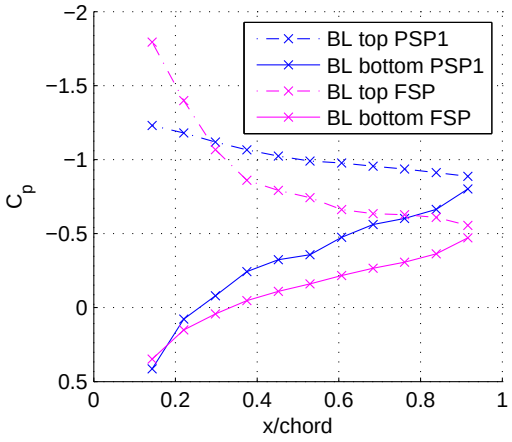

Figure 94. Cp vs. x/c @ α=17 [deg]

Flow control experiment

This experiment tests the effectiveness of the stall suppression system with different C_μ values. This test will determine if the C_μ values produced by the scaled down pulse modulator are adequate for stall suppression.

Experimental configuration

Similar to the baseline experiment, this experiment was done using the small wind tunnel, which was developed around the scaled down pulse modulator. The main computer operates the data acquisition and angle-of-attack systems, which allowed the two systems to be coordinated. The layout of the experimental systems is shown in Figure 95. The supply pressure was controlled manually; however, this was done rather easily be allowing the pressure system to stabilize before conducting the test.

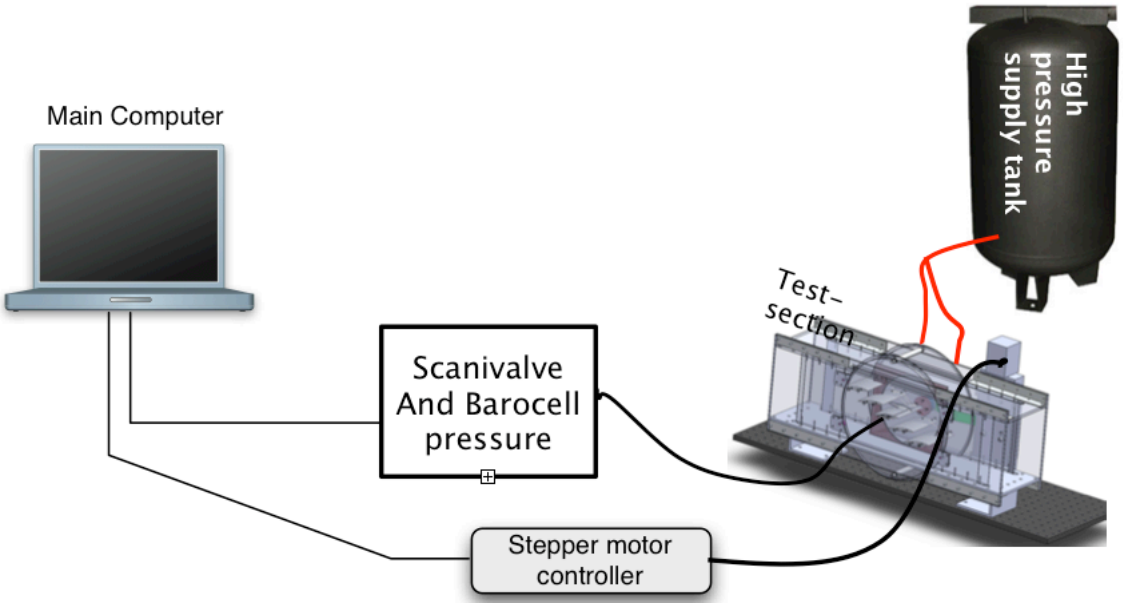

Figure 95. Layout of the experiment

a Test-blade

This experiment used the Type II test-blade equipped with wing fences and with the PSP1. This blade configuration was chosen for its clear change in pressure distribution during stall. This clear change in pressure distribution allowed the effectiveness of the stall suppression system to be evaluated.

b Instrumentation

The pressure distributions were measured using a Barocell pressure transducer in conjunction with a scanivalve. A detailed description of this system was given in the experimental setup chapter.

Test matrix

The pressure distribution was measured at several positive angles-of-attack, as listed in Table XIX. The values of the reduced lift coefficient were calculated as described in the "Baseline Pressure Distribution Experiment" section. This experiment also varied the supply pressure to the pulse modulator, which is also listed in Table XIX.

Table XIX. Test matrix for flow control pressure distribution experiment

Test-blade	PSP1 Type II test-blade
Angle-of-attack [deg]	0, 3, 6, 9 to 22
Supply pressure [psi]	5, 10, 15, 20, 25

Results

The calculated $C_{l_{red}}$ versus angle-of-attack was plotted for the baseline and flow control cases, and is shown in Figure 96. The five flow control cases are shown in black, and from this plot it is apparent that the introduction of pulse modulated blowing, even with C_μ values as low as 0.34% still, increases the maximum $C_{l_{red}}$. The baseline $C_{l_{red}}$ was subtracted from the $C_{l_{red}}$ values obtained with the flow control on, which yielded the change in $C_{l_{red}}$, as shown in Figure 97.

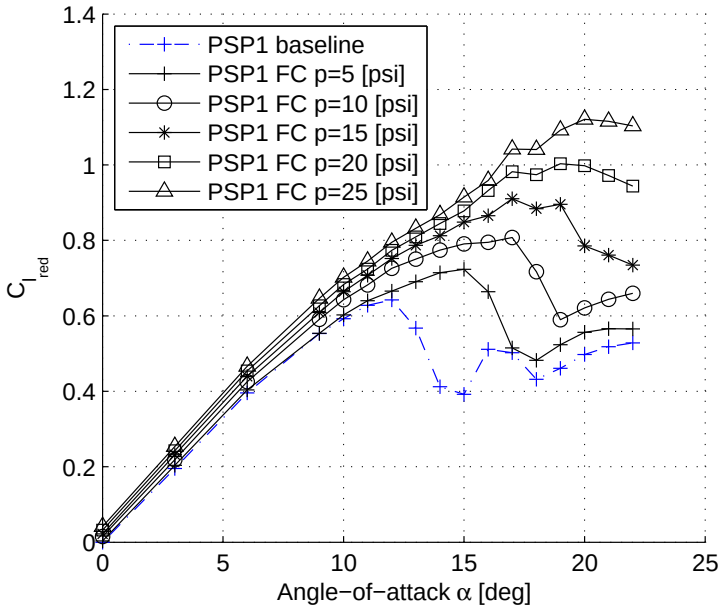

Figure 96. $C_{l_{red}}$ vs. α

The increase in the $C_{l_{red}}$ is clear in the pressure distribution plots at high angles-of-attack. The high angle-of-attack pressure distribution plots are shown below, in Figure 98 through Figure 103; however, The pressure distribution for all angle-of-attack can be found in the Appendix. Table XX compares the supply pressure, C_μ

values, and the change in the all of the $C_{l_{red}\,max}$.

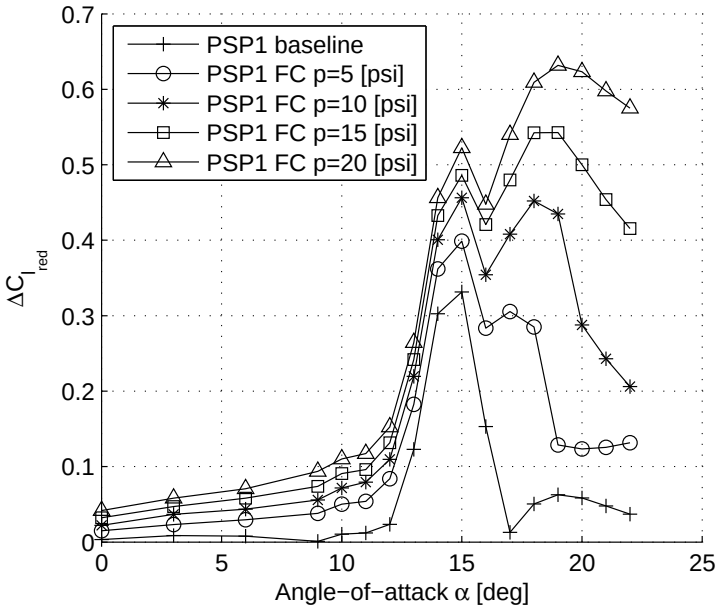

Figure 97. $\Delta C_{l_{red}}$ vs. α

Table XX. Comparison of supply pressure, C_μ values and the change in $C_{l_{red}\,max}$

Supply pressure [psi]	5	10	15	20	25
C_μ%	0.34	0.54	0.73	1.16	1.55
% Increase $C_{l_{red}\,max}$	51.6	62.1	71.1	84.5	98.4
$\Delta C_{l_{red}\,max}$	0.332	0.400	0.456	0.543	0.632

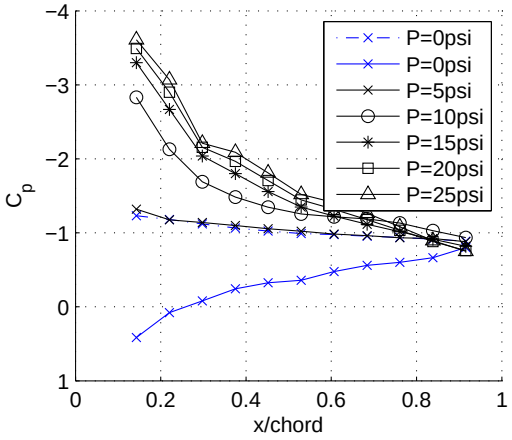

Figure 98. Cp vs. x/c @ α=17 [deg]

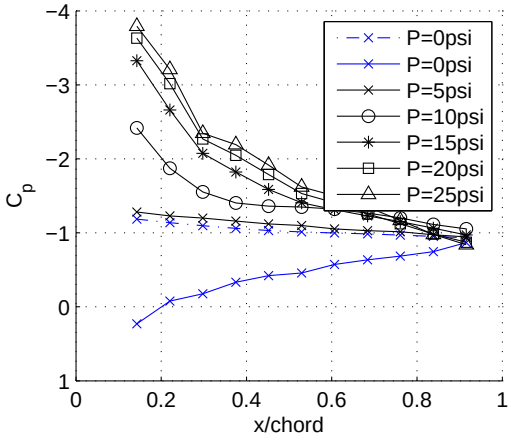

Figure 99. Cp vs. x/c @ α=18 [deg]

Summary

The pulse modulated blowing on the top surface of a NACA 0015 blade showed an increases the $C_{l_{red}\,max}$ and the critical angle-of-attack of the blade. Thus, the current design of the pulse modulator proved to be adequate for stall suppression on a NACA 0015 airfoil section in a wind tunnel.

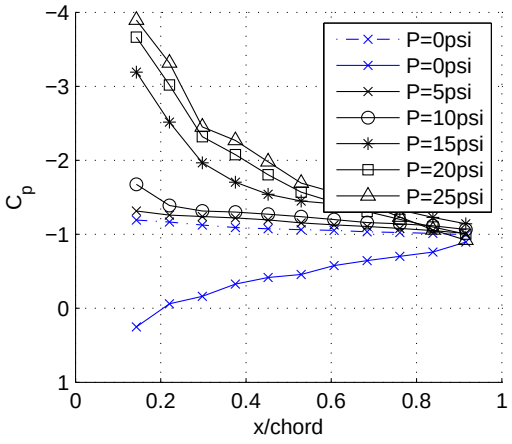

Figure 100. Cp vs. x/c @ α=19 [deg]

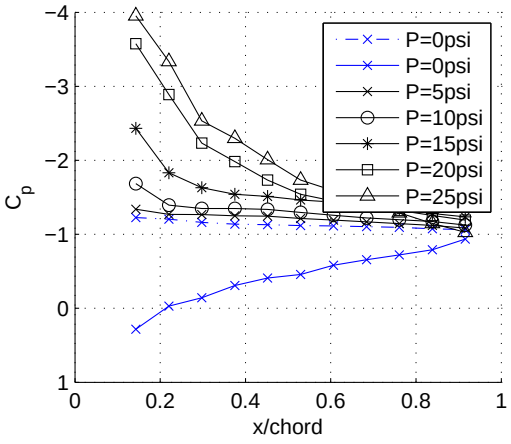

Figure 101. Cp vs. x/c @ α=20 [deg]

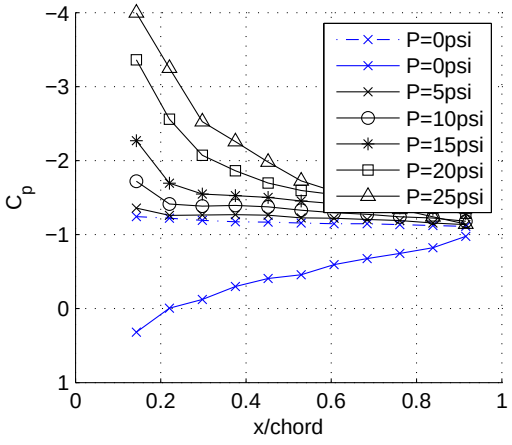

Figure 102. Cp vs. x/c @ α=21 [deg]

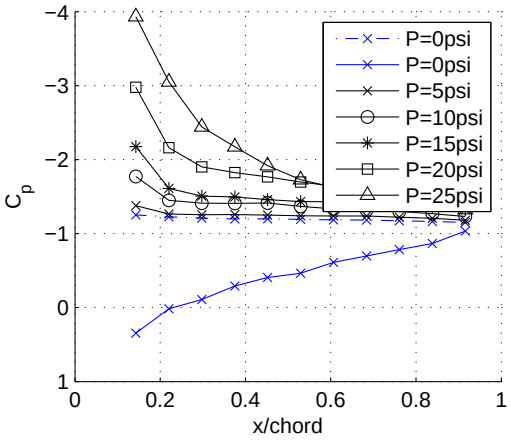

Figure 103. Cp vs. x/c @ α=22 [deg]

CHAPTER VI

CONCLUSIONS

A oscillatory blowing stall suppression system was designed to be implemented on the rotor blades of a one stage axial compressor. One of the requirements of this stall suppression system was to developed high frequency air pulses on the airfoil section of the rotor blades. This pulsing air was created using a pulse modulator that was design to be installed in the compressor. A scaled down version of the pulse modulator was built and tested to insure that the design would achieve the required flow parameters.

There were four experiments conducted on the scaled down pulse modulator. The first two studied the frequency response and the flow characteristics of the jet slot. The second two experiments required a small wind tunnel to be built around the scaled down pulse modulator. The these last two experiments studied the effects that oscillatory blowing had on the pressure distribution on the upper surface of an NACA 0015 airfoil section.

The frequency response experiment proved that, within the operating range of this compressor test rig, jet frequency did not have a significant effect on C_μ. The flow characteristic experiment showed that jet slot exit area must match the area of the inlet to the internal plenum of the blade to obtain the C_μ values that are required to effectively suppress stalls. It was also shown that the distribution of the holes in the internal pipe played an important role in the spanwize C_μ distribution; however, did not effect the mean C_μ value.

The third experiment tested the stall characteristics of the NACA 0015 airfoil in the new wind tunnel. This was done by measuring the pressure distribution on

the suction side of the airfoil. It was clear from the result of this test that the airfoil stalled between 12 and 13 degrees. Inner walls were added on the airfoil to eliminate non-uniform flow which made the stall of the blade more defined on the pressure distribution.

The fourth experiment studied the pressure distribution on the suction side of the airfoil with the oscillatory blowing stall suppression system in operation. This test was conducted with the inner walls on the airfoil. The results showed that the oscillatory blowing stall suppression system increases the $C_{l_{red\,max}}$ as well as the critical angle-of-attack of the blade.

These four tests conducted on the scaled down pulse modulator yielded results that proved that the full size pulse modulator is would be worth building for the compressor.

BIBLIOGRAPHY

[1] Cumpsty, N. A., *Compressor Aerodynamics*, Longman, 1989.

[2] Iura, T. and Rannie, W. D., "Experimental Investigations of Propagating Stall in Axial-Flow Compressors," *Transactions of the ASME*, Vol. 76, No. 3, April 1954, pp. 463–471.

[3] McKenzie, A. B., *Axial Flow Fans and Compressors, Aerodynamic Design and Performance*, Cranfield Series on Turbomachinery Technology, Ashgate, Aldershot, 1997.

[4] Emmons, H. W., Pearson, C. E., and Grant, H. P., "Compressor Surge and Stall Propagation," *Transactions of the ASME*, Vol. 77, No. 4, May 1955, pp. 455–469.

[5] Day, I. J., "Review of stall, surge and active control in axial compressors," *Eleventh International Symposium on Air Breathing Engines*, AIAA, Tokyo, Japan, September 1993, pp. 97–105.

[6] Suder, K. L., Hathaway, M. D., Thorp, S. A., Strazisar, A. J., and Bright, M. B., "Compressor Stability Enhancement Using Discrete Tip Injection," *Journal of Turbomachinery. Transactions of the ASME*, Vol. 123, No. 1, January 2001, pp. 14–23.

[7] Greenblatt, D., Darabi, A., Nishri, B., and Wygnanski, I., "Separation Control By Periodic Addition of Momentum with Particular Emphasis on Dynamic Stall," *Proceedings Heli Japan 98*, Paper T3-4, 1998.

[8] Amitay, M., Smith, L., and Glezer, A., "Aerodynamic Flow Control Using Synthetic Jet Technology," *36th Aerospace Science Meeting and Exhibit*, AIAA Paper 1998-0208, January 1998.

[9] Traub, L., Miller, A., Ukpai, U., Rediniotis, O., Jeong, G., and Kim, K., "Reconfigurable Synthetic Jet Actuation And Closed-Loop Flow Control," *41st Aerospace Sciences Meeting and Exhibit*, AIAA Paper 2003-0217, January 2003.

[10] Gilarranz, J. L., Traub, L. W., and Rediniotis, O. K., "Characterization of a compact, high-power synthetic jet actuator for flow separation control," *40th AIAA Aerospace Sciences Meeting & Exhibit*, AIAA-2002-127, January 2002.

[11] Traub, L., Miller, A., and Rediniotis, O. K., "Effects of Active and Passive Flow Control on Dynamic Stall Vortex Formation," *Journal of Aircraft*, Vol. 41, No. 2, March-April 2004, pp. 405–408.

[12] Melton, L. P., Hannon, J., Yao, C.-S., and Harris, J., "Active Flow Control At Low Reynolds Numbers on a NACA 0015 Airfoil," *Applied Aerodynamics Conference*, No. AIAA 2008-6407, AIAA, August 2008.

[13] Seifert, A., Greenblatt, D., and Wygnanski, I., "Actice Separation control: an overview of Reynolds and Mach numbers effects," *Aerospace Science and Technology*, June 2004, pp. 569–582.

[14] "ABACUS, Software Package," ABACUS, Software Package, Ver 6.8 2008 Dassault Systems, Lowell, MA, 2008.

[15] Automation Creation, Inc, Website, www.matweb.com, 1996-2010.

[16] Allen, D. H. and Haisler, W. E., *Introduction to Aerospace Structural Analysis*, John Wiley & Sons, 1985.

[17] McMaster-Carr Supply Comp., Website, www.mcmaster.com.

[18] SolidWorks, Software Package, Ver. 2009 SP4, Dassault Systems, Lowell, MA, 2009.

[19] Ugrural, A. C. and Fenster, S. K., *Advanced Strength and Applied Elasticity*, Elsevier, Upper Saddle River, NJ, 3rd ed., 1981.

[20] RAE, H. W. and Pope, A., *Low-speed Wind Tunnel Testing*, John Wiley & Sons, Hoboken, NJ, 2nd ed., 1984.

[21] Seifert, A. and Pack, L., "Oscillatory Excitation of Unsteady Compressible Flows Over Airfoils at Flight Reynolds Number," *37th Aerospace Science Meeting and Exhibit*, AIAA Paper 99-0925, January 1999.

[22] Traub, L., Miller, A., and Rediniotis, O. K., "Effects of Synthetic Jet Actuation on a Pitching NACA 0015 Wing," *Journal of Aircraft*, Vol. 41, No. 5, September-October 2004, pp. 1153–1162.

APPENDIX A

EXPERIMENTED DATA

A.1 C_μ values gathered from frequency response experiment

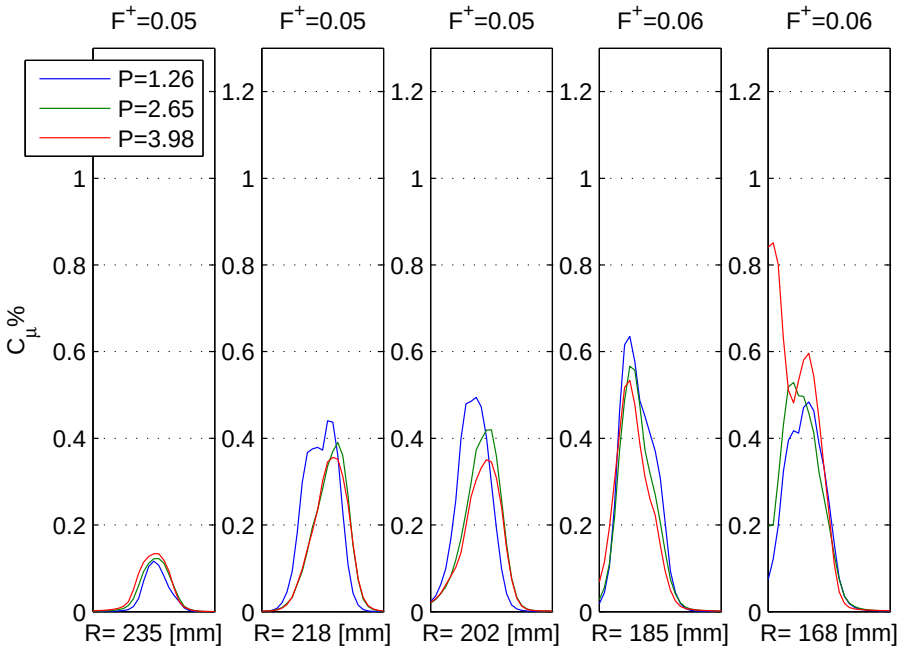

Figure A.1. C_μ @ $F^+ = 0.05$ at tip

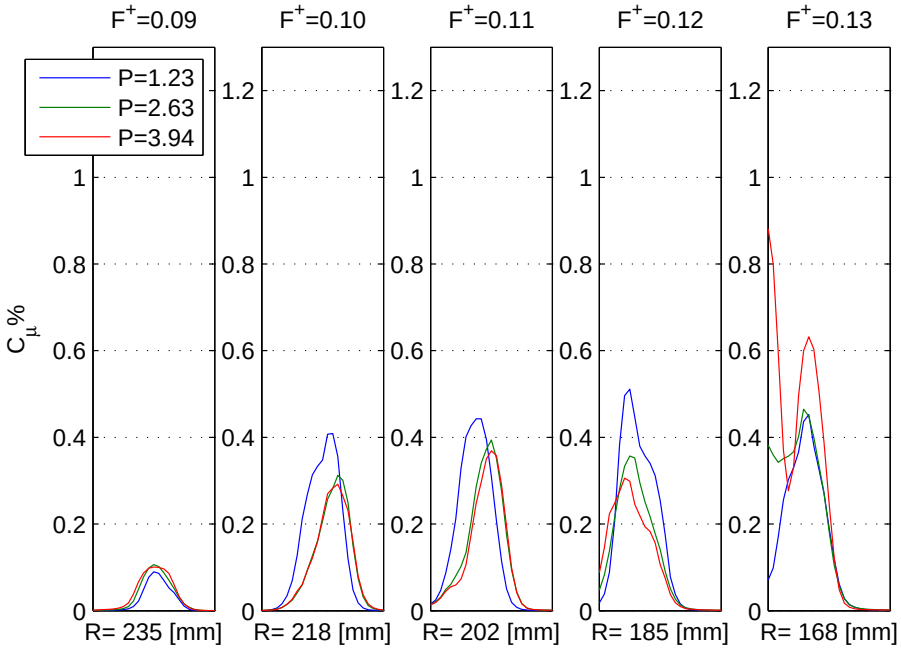

Figure A.2. C_μ @ $F^+ = 0.09$ at tip

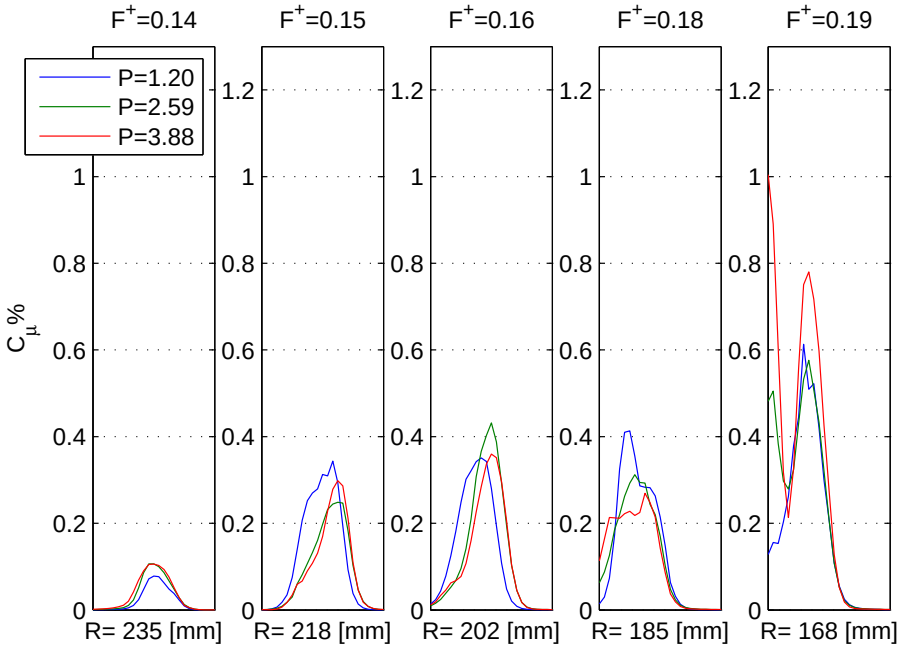

Figure A.3. C_μ @ $F^+ = 0.14$ at tip

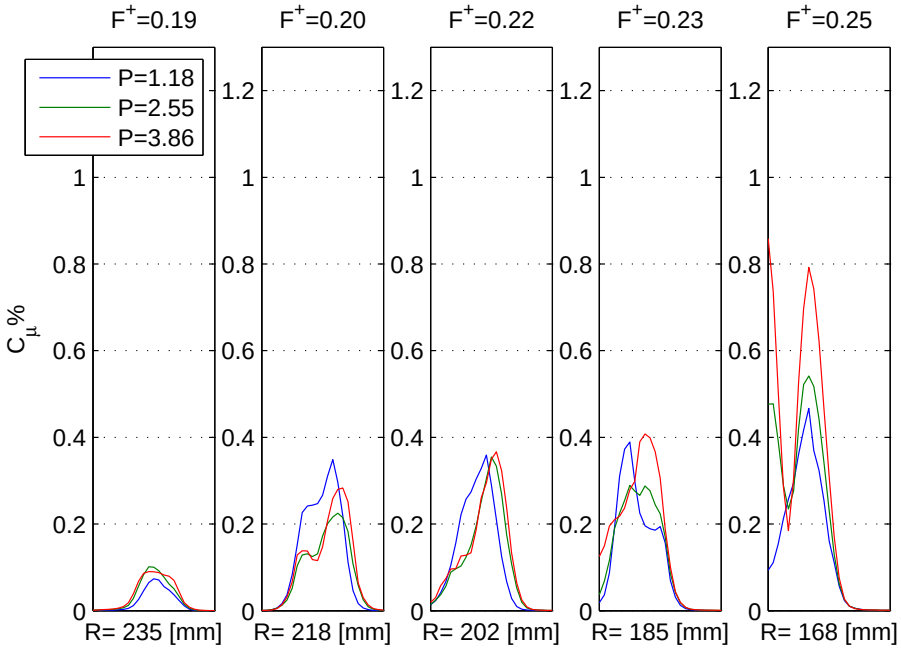

Figure A.4. C_μ @ $F^+ = 0.19$ at tip

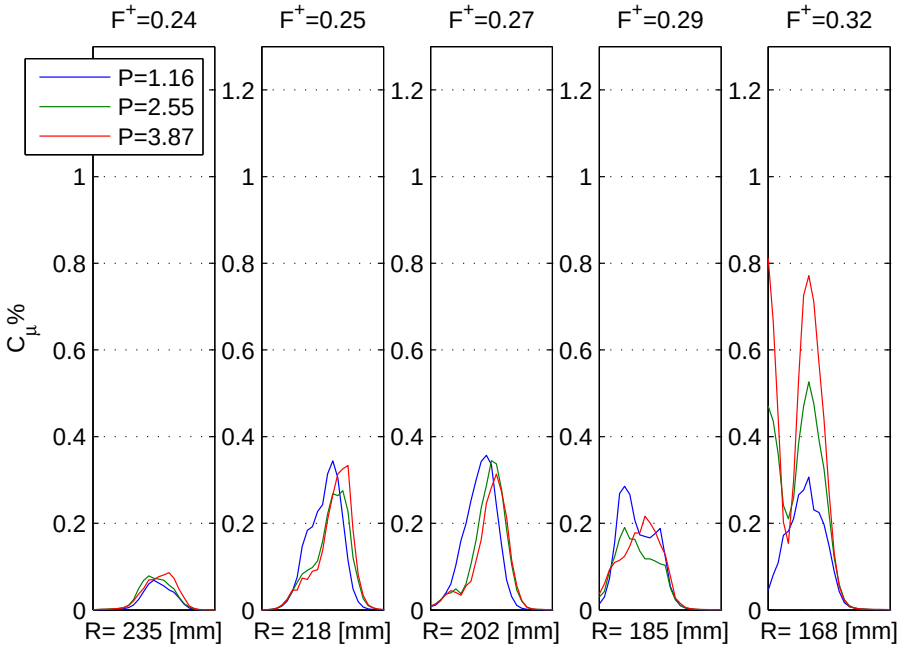

Figure A.5. C_μ @ $F^+ = 0.24$ at tip

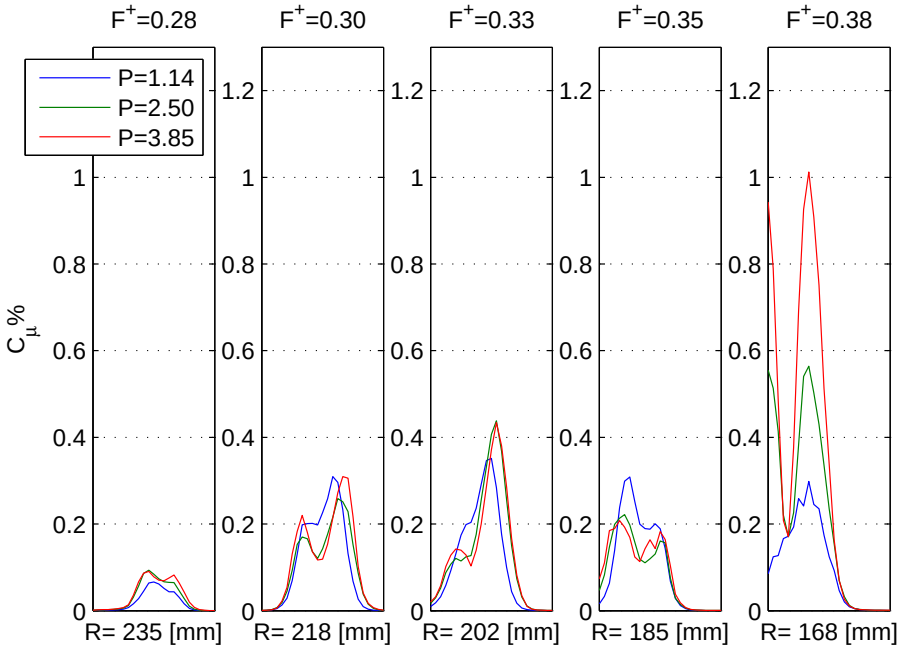

Figure A.6. C_μ @ $F^+ = 0.28$ at tip

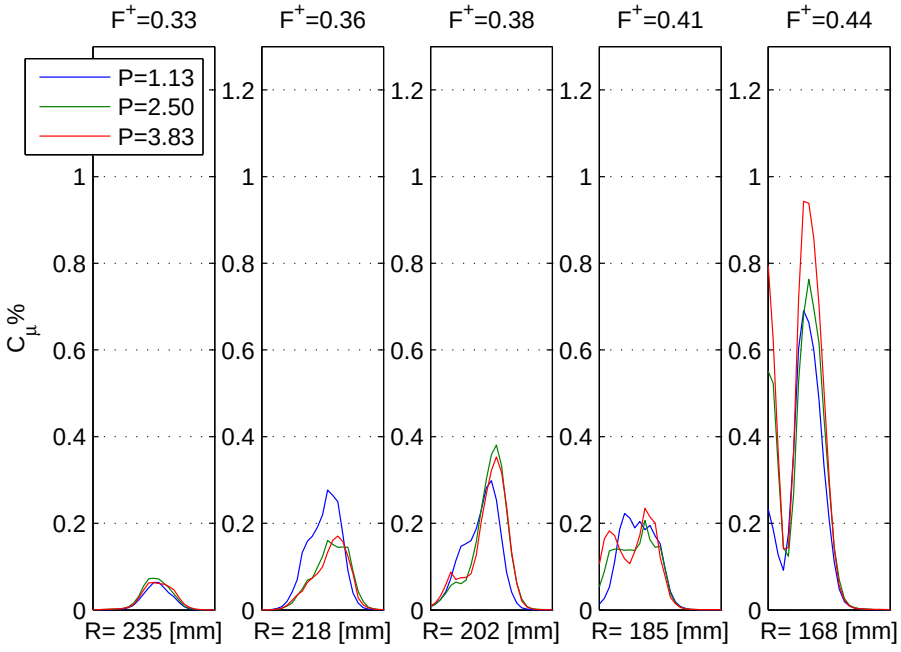

Figure A.7. C_μ @ $F^+ = 0.33$ at tip

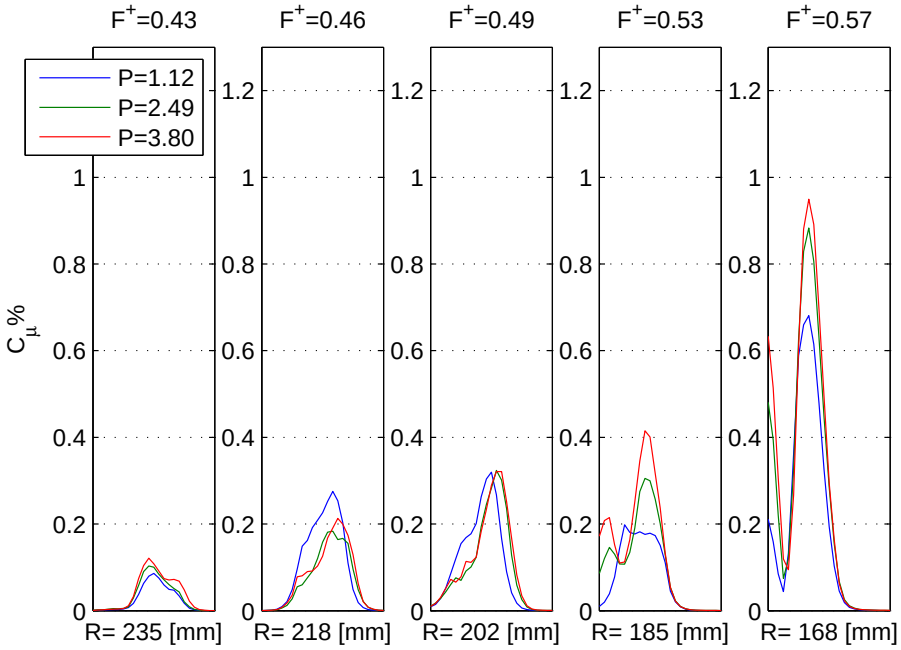

Figure A.8. C_μ @ $F^+ = 0.43$ at tip

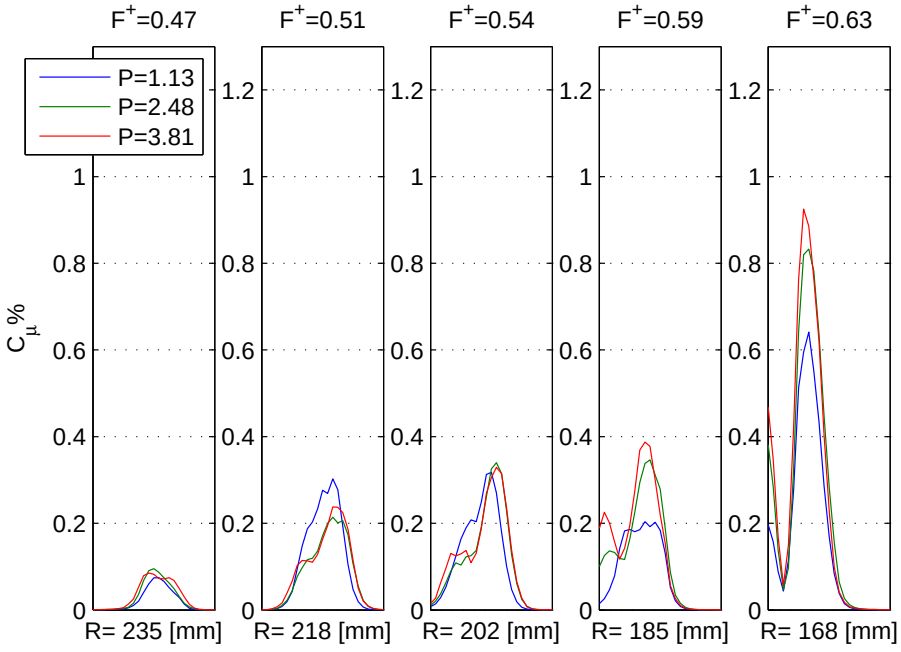

Figure A.9. C_μ @ $F^+ = 0.47$ at tip

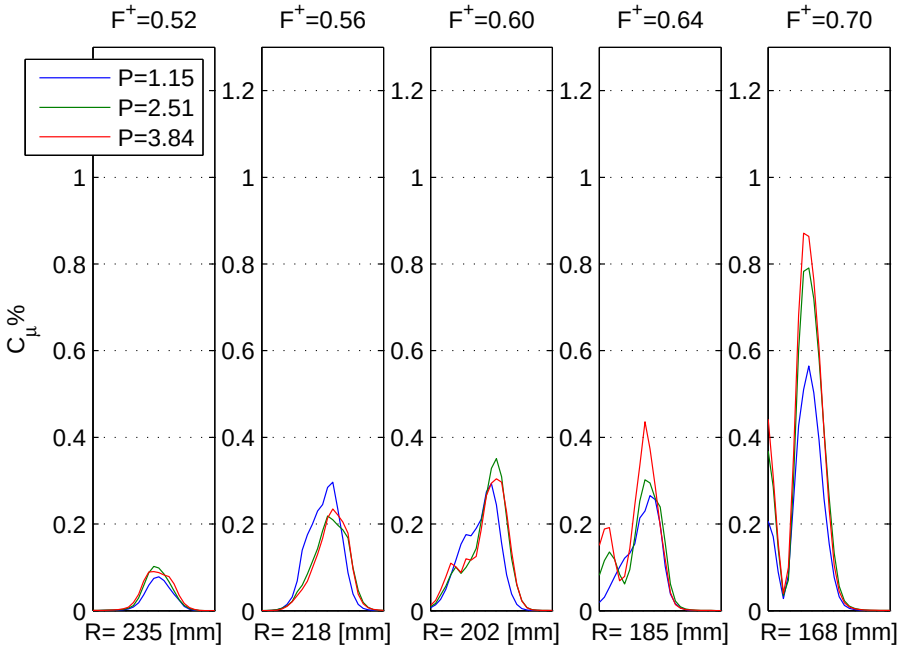

Figure A.10. C_μ @ $F^+ = 0.52$ at tip

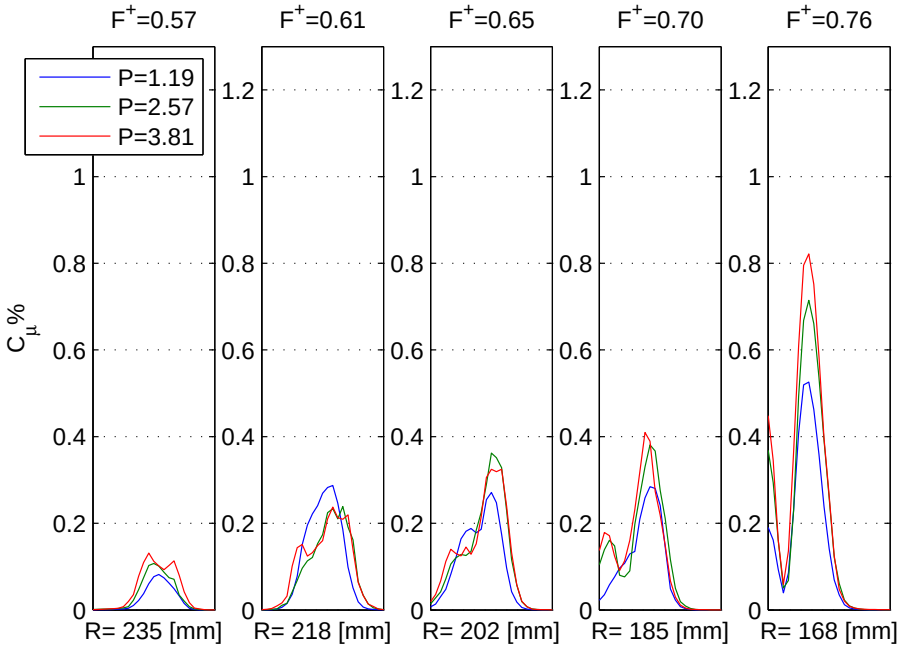

Figure A.11. C_μ @ $F^+ = 0.57$ at tip

A.2 $C_{l_{red}}$plot of baseline

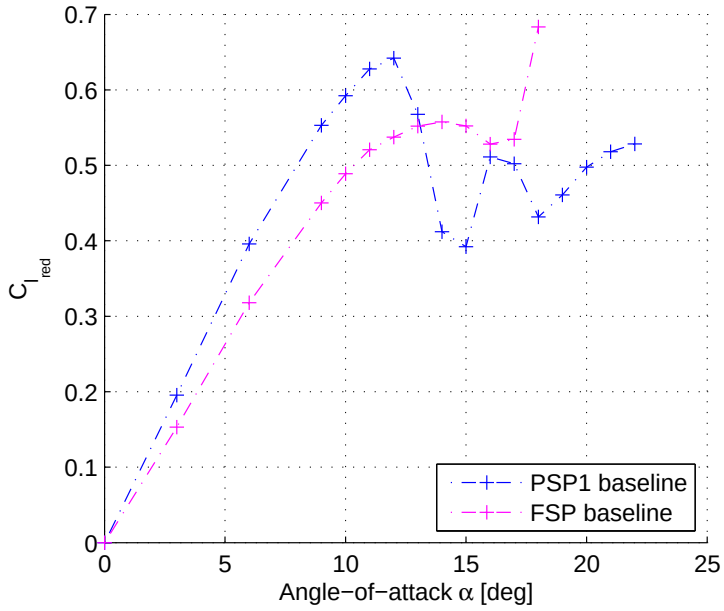

Figure A.12. Part and full span $C_{l_{red}}$ vs. α

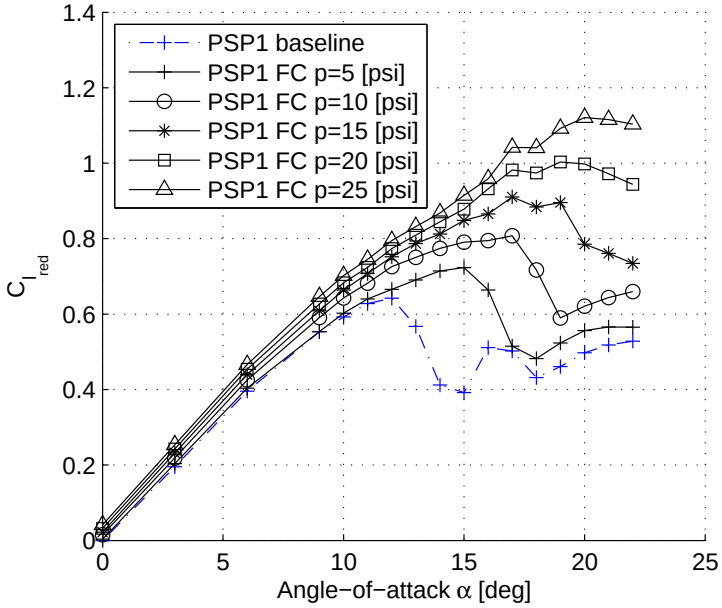

Figure A.13. $C_{l_{red}}$vs. α

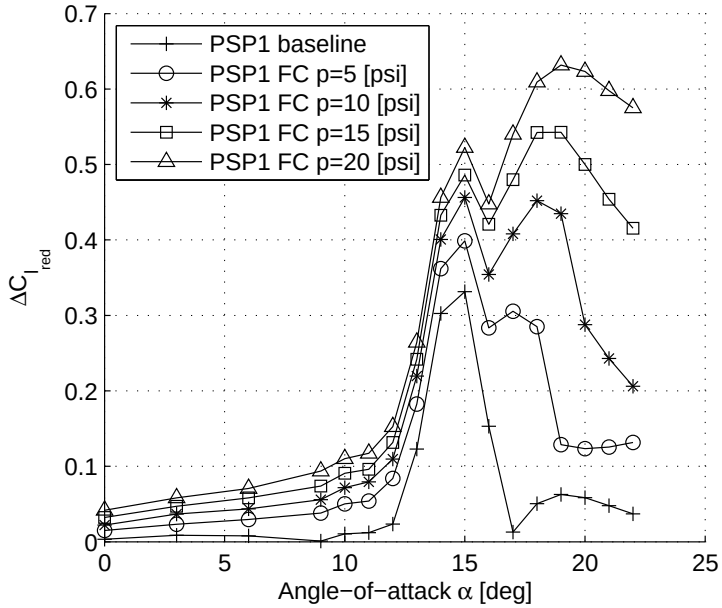

Figure A.14. $\Delta C_{l_{red}}$ vs. α

A.3 Cp plot of baseline

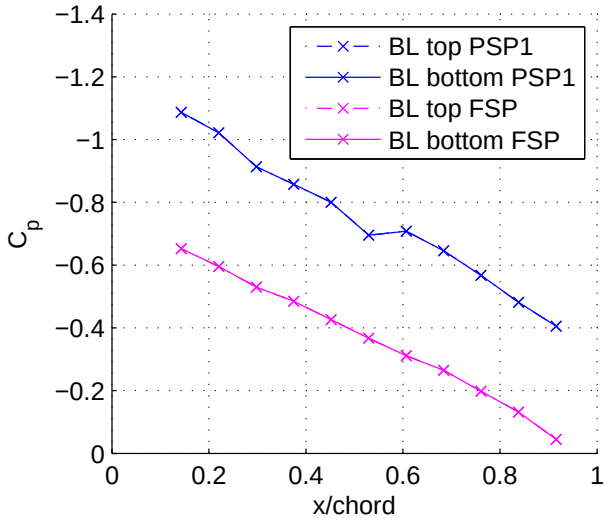

Figure A.15. Cp vs. x/c @ α=0 [deg]

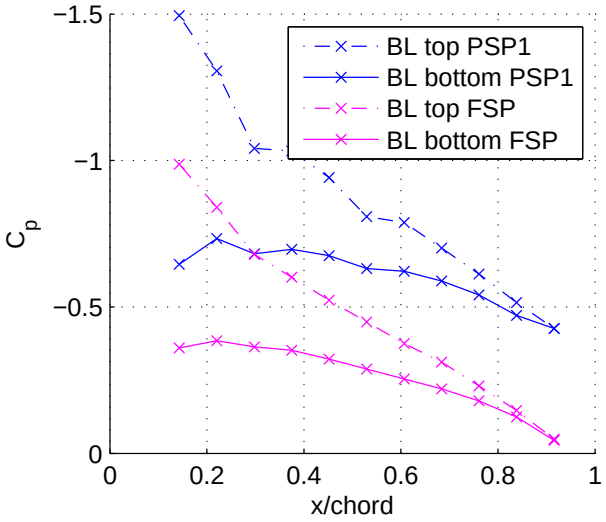

Figure A.16. Cp vs. x/c @ α=3 [deg]

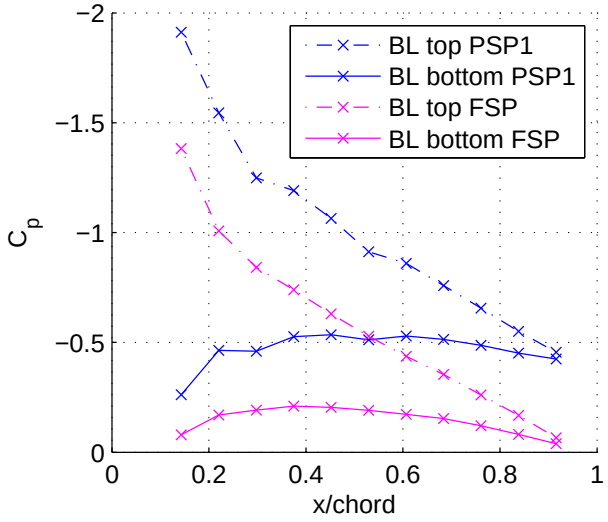

Figure A.17. Cp vs. x/c @ α=6 [deg]

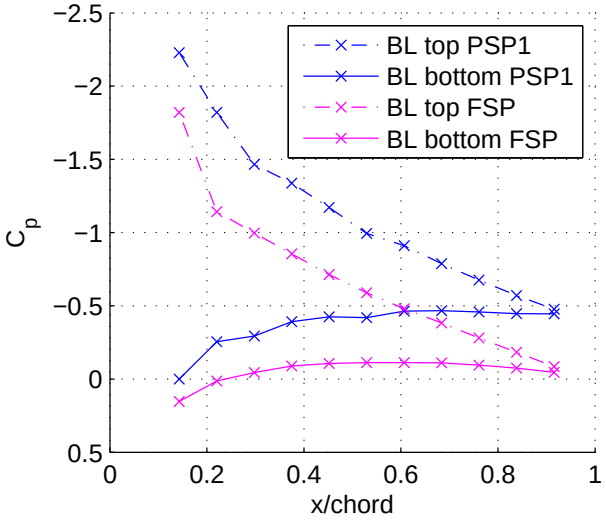

Figure A.18. Cp vs. x/c @ α=9 [deg]

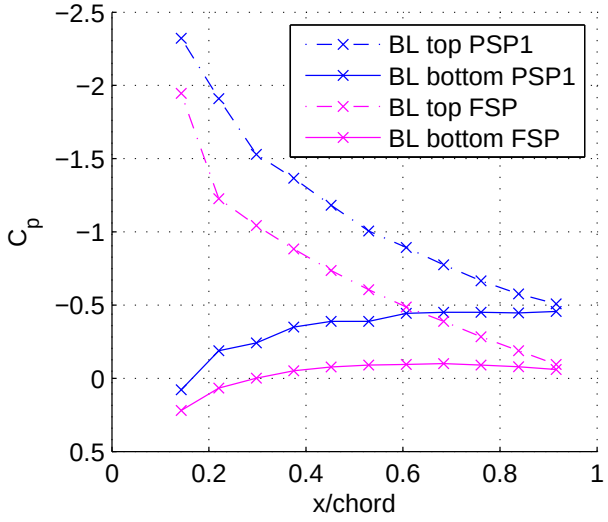

Figure A.19. Cp vs. x/c @ α=10 [deg]

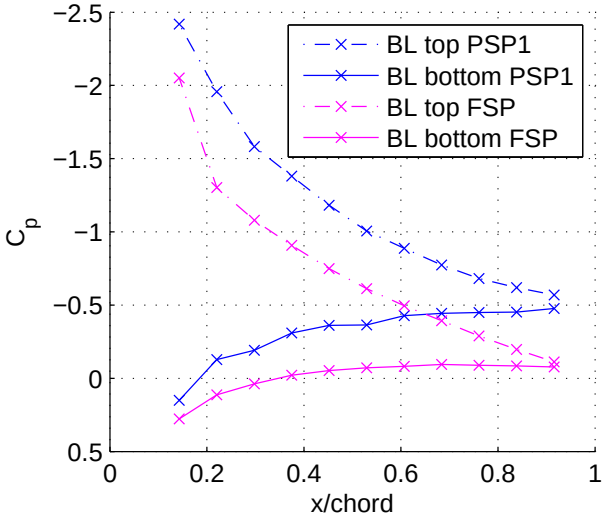

Figure A.20. Cp vs. x/c @ α=11 [deg]

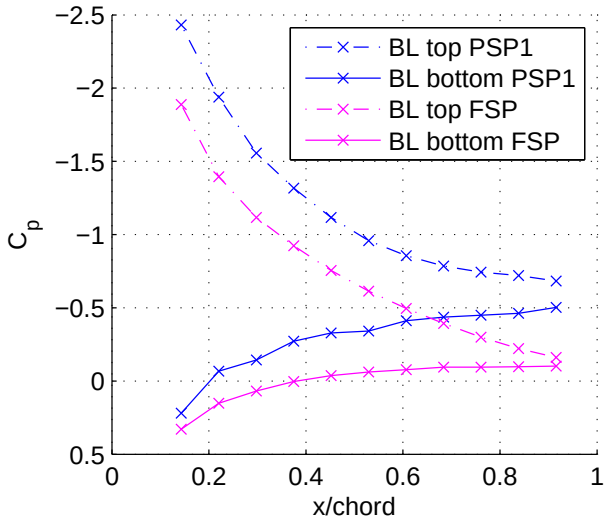

Figure A.21. Cp vs. x/c @ α=12 [deg]

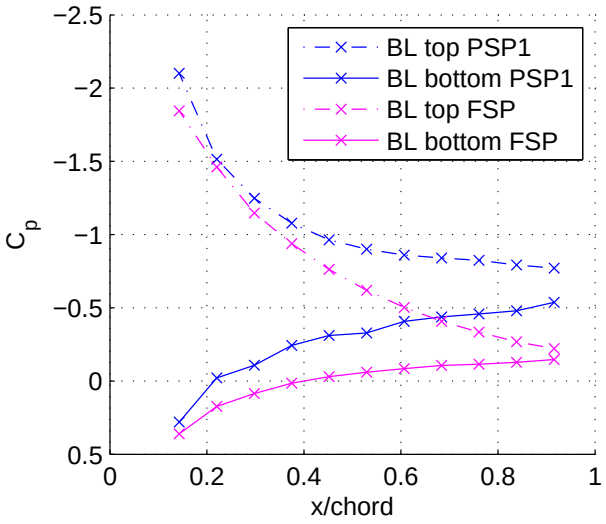

Figure A.22. Cp vs. x/c @ α=13 [deg]

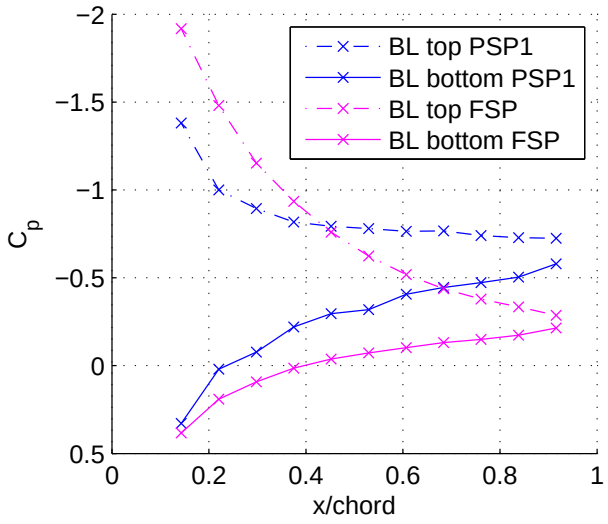

Figure A.23. Cp vs. x/c @ α=14 [deg]

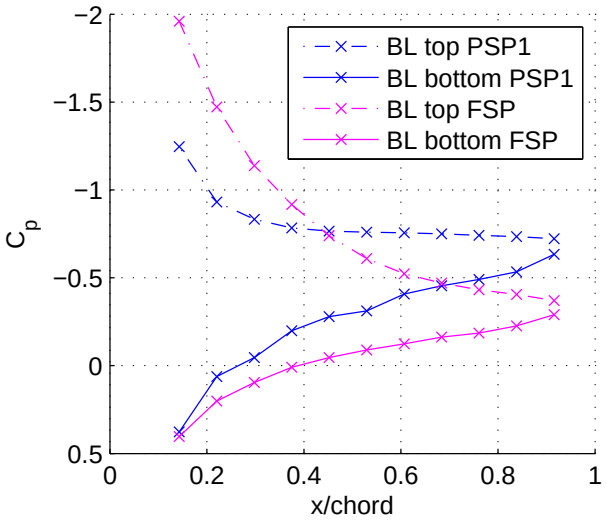

Figure A.24. Cp vs. x/c @ α=15 [deg]

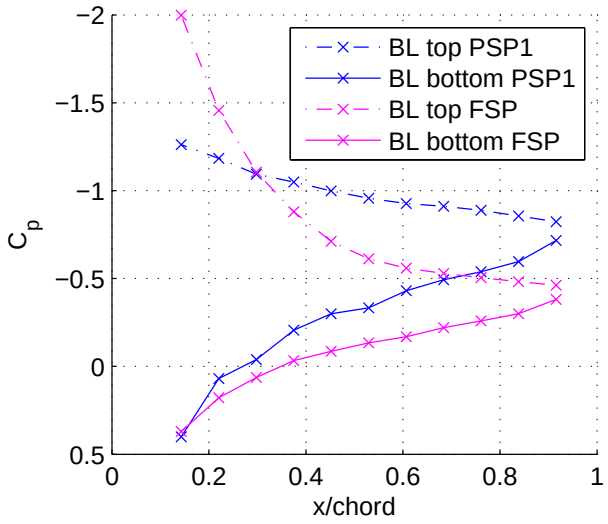

Figure A.25. Cp vs. x/c @ α=16 [deg]

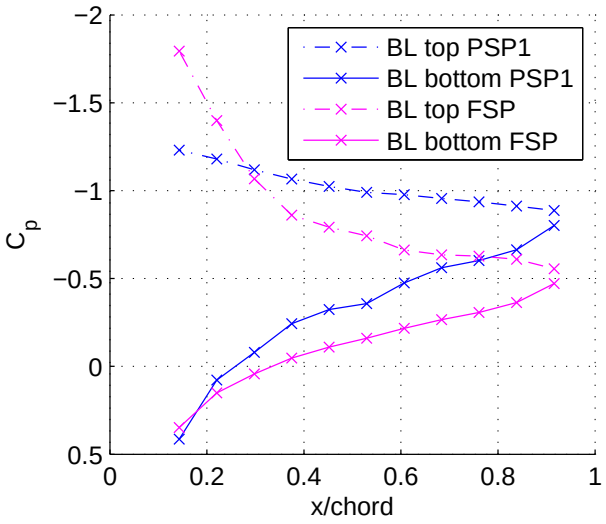

Figure A.26. Cp vs. x/c @ α=17 [deg]

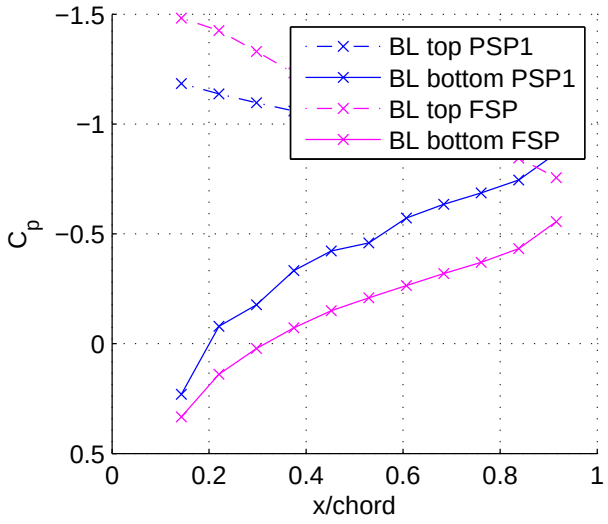

Figure A.27. Cp vs. x/c @ α=18 [deg]

A.4 Cp plot with flow control

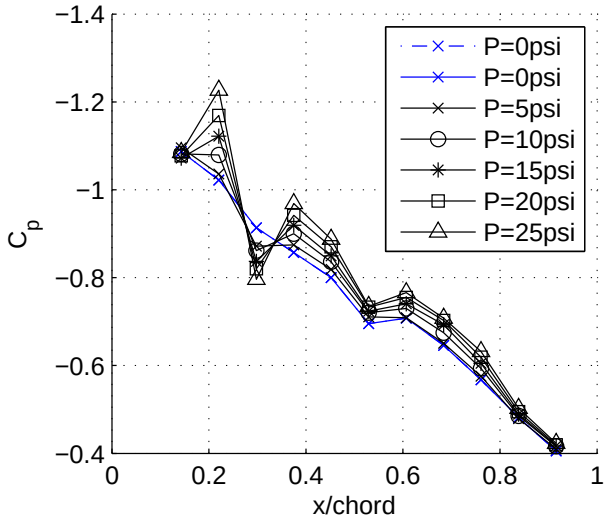

Figure A.28. Cp vs. x/c @ α=0 [deg]

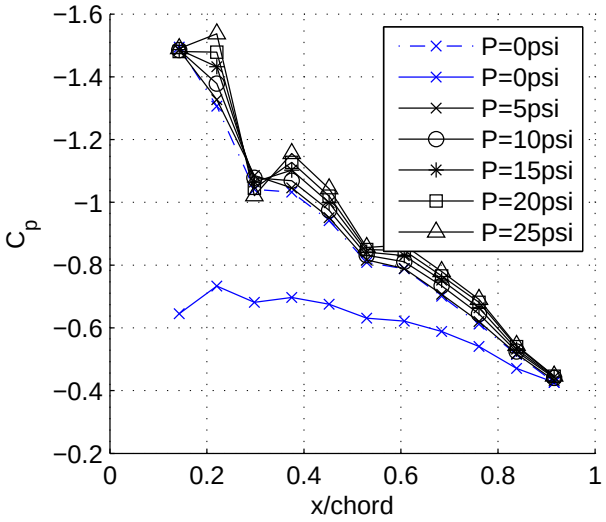

Figure A.29. Cp vs. x/c @ α=3 [deg]

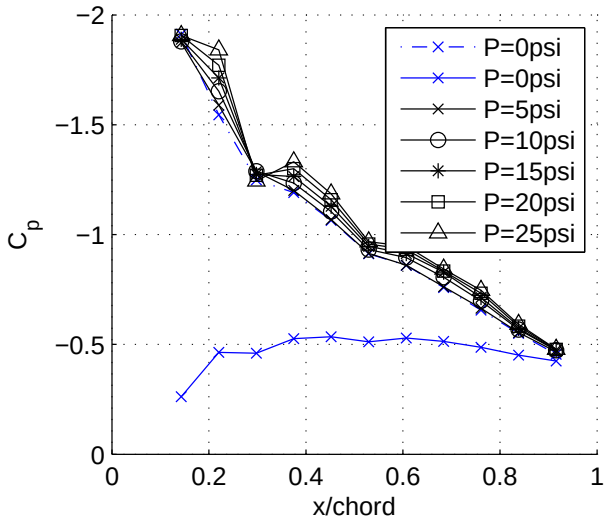

Figure A.30. Cp vs. x/c @ α=6 [deg]

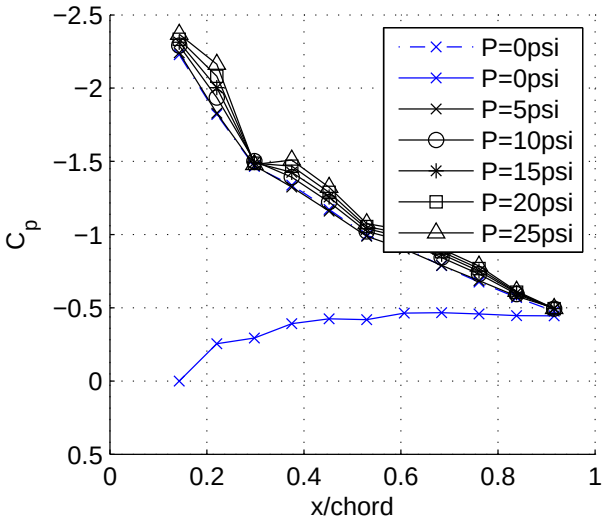

Figure A.31. Cp vs. x/c @ α=9 [deg]

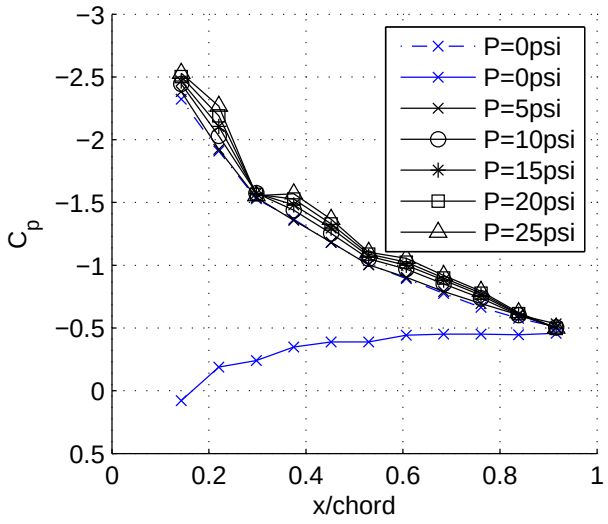

Figure A.32. Cp vs. x/c @ α=10 [deg]

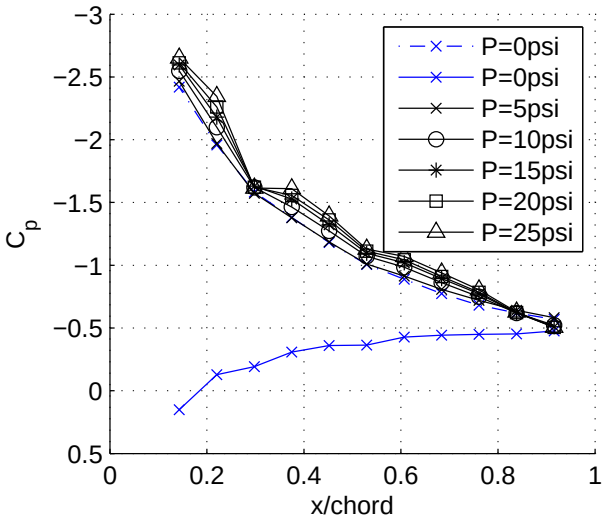

Figure A.33. Cp vs. x/c @ α=11 [deg]

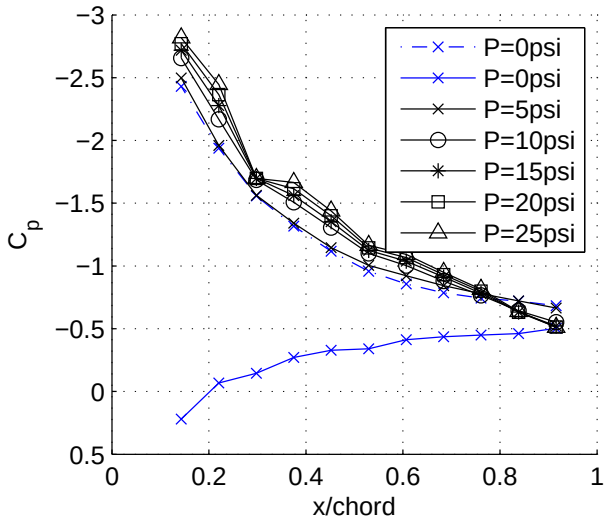

Figure A.34. Cp vs. x/c @ α=12 [deg]

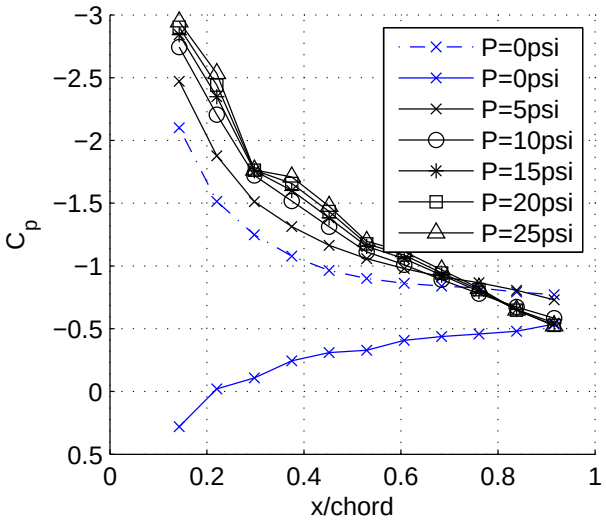

Figure A.35. Cp vs. x/c @ α=13 [deg]

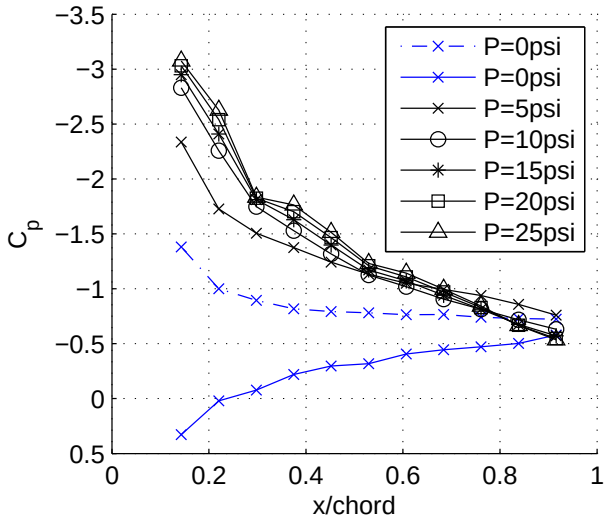

Figure A.36. Cp vs. x/c @ α=14 [deg]

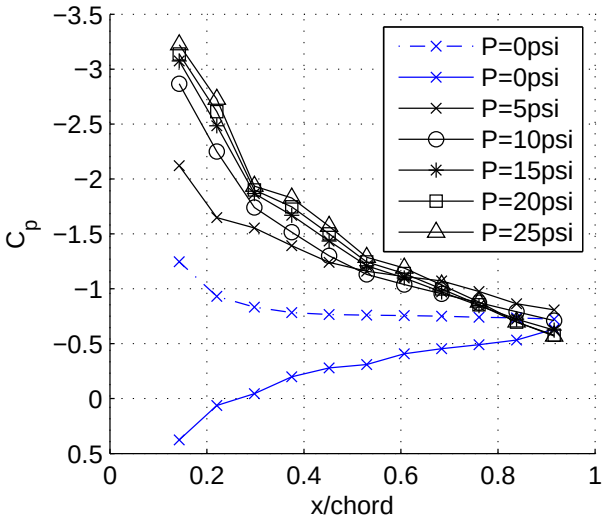

Figure A.37. Cp vs. x/c @ α=15 [deg]

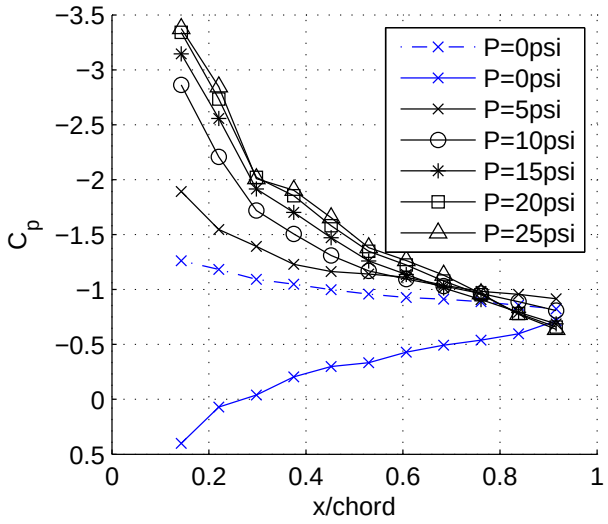

Figure A.38. Cp vs. x/c @ α=16 [deg]

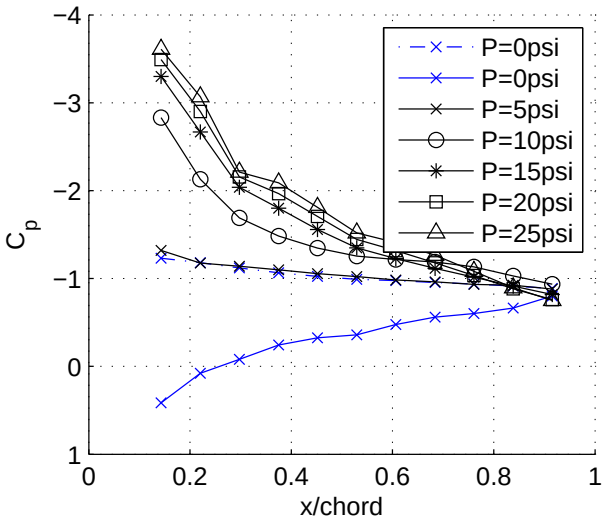

Figure A.39. Cp vs. x/c @ α=17 [deg]

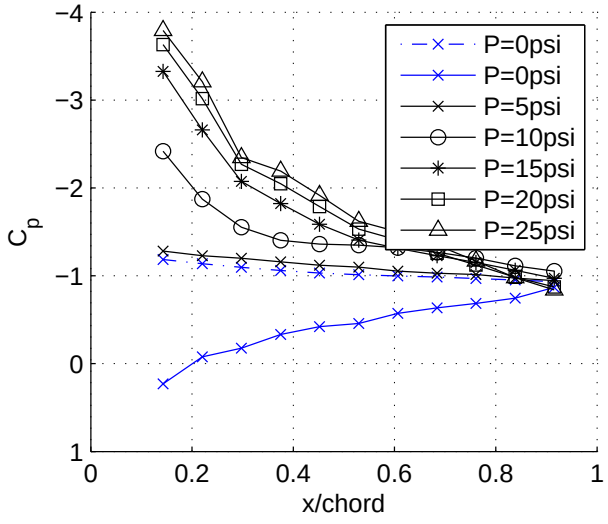

Figure A.40. Cp vs. x/c @ α=18 [deg]

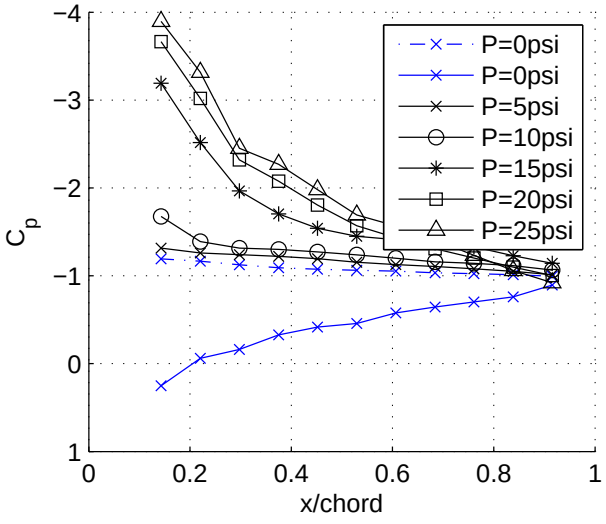

Figure A.41. Cp vs. x/c @ α=19 [deg]

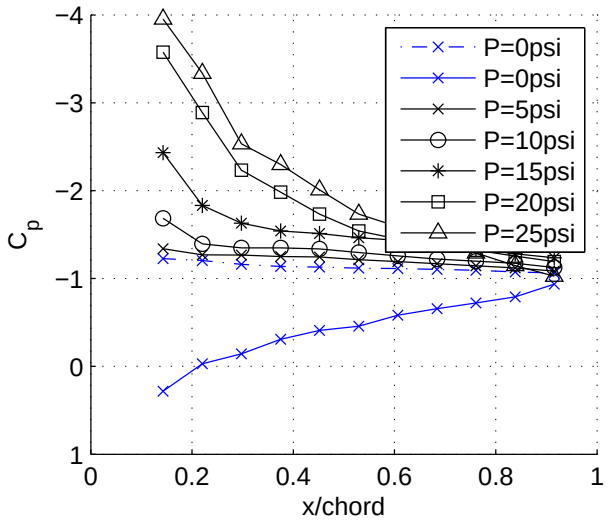

Figure A.42. Cp vs. x/c @ α=20 [deg]

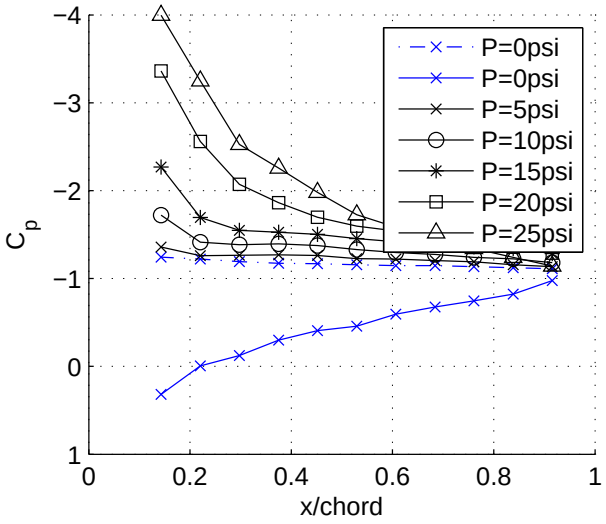

Figure A.43. Cp vs. x/c @ α=21 [deg]

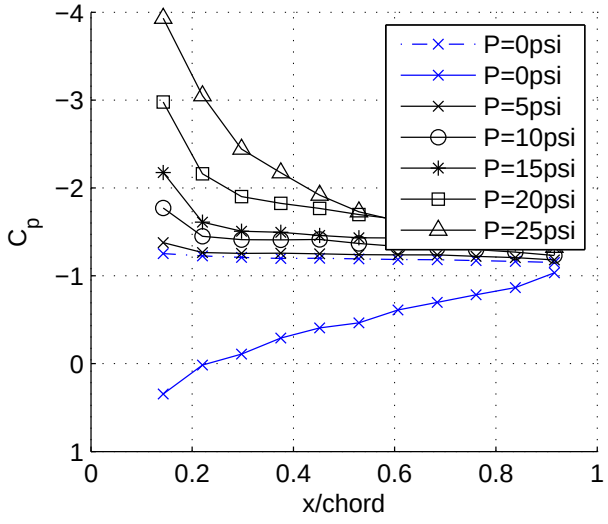

Figure A.44. Cp vs. x/c @ α=22 [deg]

VITA

Shalom Johnson was born in Galveston, Texas. He obtained his Bachelor of Science degree in Aerospace Engineering from the Dwight Look College of Engineering, Texas A&M University, College Station, Texas, in Dec 2007. He began graduate studies in Aerospace Engineering at Texas A&M University in Jan 2007.

Contact address: Texas A&M University, Department of Aerospace Engineering
Shalom Johnson
H.R. Bright Building, TAMU 3141
College Station, TX 77843-3141

Email address: shalom.johnson7@gmail.com

Education: B.S. Aerospace Engineering, Texas A&M University, 2007
M.S. Aerospace Engineering, Texas A&M University, 2010